Photometric, Thermal, and Spatial Evolution of the Impact Flash

by

Carolyn Martha Ernst

Sc.M., Brown University, 2003
Sc.B., Brown University, 2001

Dissertation

Submitted in partial fulfillment of the requirements
for the degree of Doctor of Philosophy
in the Department of Geological Sciences at Brown University

Providence, Rhode Island
May 2008

This dissertation by Carolyn Ernst is accepted in its present form by the Department of Geological Sciences as satisfying the dissertation requirements of the degree of Doctor of Philosophy.

Date ________________ ______________________________
Professor Peter H. Schultz, Advisor

Recommended to the Graduate Council

Date ________________ ______________________________
Professor Carlé M. Pieters

Date ________________ ______________________________
Professor E. Marc Parmentier

Date ________________ ______________________________
Professor Michael B. Wyatt

Date ________________ ______________________________
Dr. David A. Crawford
Sandia National Labs, NM

Approved by the Graduate Council

Date ________________ ______________________________
Dr. Sheila Bonde
Dean of the Graduate School

Carolyn Martha Ernst

Department of Geological Sciences
Brown University, Box 1846
Providence, RI 02912

Email: Carolyn_Ernst@alumni.brown.edu
Phone: 401.863.3594
Fax: 401.863.3978

Vita

Born September 18, 1979
Boston, Massachusetts

Education

BROWN UNIVERSITY**,** Providence, Rhode Island

- **Ph.D.**, **Geological Sciences**, May 2008.
  Advisor: Dr. Peter H. Schultz
- **Sc.M.**, **Geological Sciences**, May 2003.
- **Sc.B.,** **Physics**, May 2001.
  magna cum laude, with honors

Research Experience

Research Assistant, Brown University, 2001 – Present.

- Designing and performing impact experiments at the NASA Ames Vertical Gun Range.
- Analyzing the light intensity, temperature, and emitting source area evolution of the impact flash using experimental photometric data, utilizing software packages including: C, IDL, Matlab, Excel, Photoshop, Illustrator.
- Assessing the effect of initial conditions on the resulting impact flash.

Deep Impact Science Team, Member, 2005-2006.

- Performed real-time image processing on comet approach spacecraft images.
- Analyzed encounter data, focusing on the impact flash and vapor plume, using IDL, Photoshop, and Excel.

Workshop Participant, Sandia National Laboratories, March 2003.

- Attended an introductory class on the CTH shock-physics hydrocode, learning problem generation and execution.

Undergraduate Research Assistant, Brown University, Providence, RI, Summer 2000.

- Summer research project with Dr. Peter Schultz.
- Wrote computer programs in C and Excel to examine the origin of deep Imbrium Structure grooves, using spherical trigonometry to determine their convergence with respect to the basin.

- Analyzed ejecta patterns from experimental impacts to compare to Imbrium results.

Undergraduate Research Assistant, Smithsonian Astrophysical Observatory, Cambridge, MA, Summer 1999.

- NSF Research Experiences for Undergraduates project with Dr. Matthew Holman.
- Performed photometric and astrometric analyses on Kuiper Belt Objects and other minor planetary bodies.
- Observed Kuiper Belt Objects and asteroids using the 1.2-meter telescope at Whipple Observatory, AZ.

Honors and Awards

- NASA Graduate Student Researchers Program Fellowship, 2004-2007.
- Brown University First-year Fellowship for Graduate Study, 2001-2002.
- Elected to Sigma Xi, Brown University chapter, 2001.

Teaching Experience

Teaching Assistant, Brown University, Providence, RI
"Mars, Moon, and the Earth", Fall 2002

- Led laboratory sections for 120 students, held weekly office hours, and graded exams, laboratory reports, and weekly exercises.

Guest Lecturer
"Planetary Geology", Brown University, Providence, RI, 2006, 2007, 2008.
"The Solar System", Wheaton College, Norton, MA, 2005.

Undergraduate Teaching Assistant, Brown University, Providence, RI
"Beginning Astronomy I, II" (for non-majors), Fall 1999-Spring 2001.

- Led observational laboratory sections. Operated 16-inch reflector in conjunction with a CCD camera and a spectrometer, along with various smaller telescopes.

"Introduction to Astronomy" (for majors), Spring 2000, 2001.

- Held weekly discussion section for student questions and review. Led observational laboratory sections. Operated 16-inch reflector in conjunction with a CCD camera and a spectrometer, as well as various smaller telescopes.

Teaching-Related Activities

Mad Scientist Network (www.madsci.org)
Mad Scientist, 2002-Present.

- Responded to general questions submitted by the public about astronomy, geology, and planetary science.

The Sheridan Center for Teaching and Learning in Higher Education, Brown University
Sheridan Teaching Certificate I, 2006.

- Completed a series of seminars and workshops to develop a reflective teaching practice, and received an individual teaching consultation from trained Sheridan Center staff.

Community Outreach Talks
"Snowballs from Space", May 21, 2006, Bryant College, Providence, RI.

- Introduced four classes of 15 6th-8th grade students to comets at a statewide Girl Scout math and science day.

"The Deep Impact Mission: Results from the First Planetary-Scale Experiment", April 7, 2005, Seagrave Observatory, Sciuate, RI.

- Lectured for ~70 members of the Skyscrapers Amateur Astronomers Society of Rhode Island

"A Future in Astronomy", December 3, 2002, Watertown High School, Watertown, MA

- Lectured for five senior physics and astronomy classes of 15-20 students each.

Publications

Peer-Reviewed Papers:

Ernst, C.M. and Schultz, P.H. (2007) Evolution of the Deep Impact flash: Implications for the nucleus surface based on laboratory experiments, *Icarus*, *190*, 334-344.

Schultz, P.H., Eberhardy, C.A., **Ernst, C.M.**, A'Hearn, M.F., Sunshine, J.M., and Lisse, C.M. (2007), The Deep Impact oblique impact cratering experiment, *Icarus*, *190*, 295-333.

Schultz, P.H., Sugita, S., Eberhardy, C.A., **Ernst, C.M.** (2006) The role of ricochet in impact vaporization, *International Journal of Impact Engineering*, Vol. 33, 771-780.

A'Hearn, M.F., ***et al.*** (2005) Deep Impact: Excavating Comet Tempel 1, *Science*, Vol. 310, Iss. 5746, 258-264.

Schultz, P.H., **Ernst, C.M.**, and Anderson, J.L.B. (2005) Expectations for crater size and photometric evolution from the Deep Impact collision, *Space Science Reviews*, Vol. 117, Iss. 1-2, 207-239.

Conference Abstracts:

Ernst, C.M. and Schultz, P.H. (2008) Effects of view orientation on impact flash observations: Implications for lunar impacts, *Lunar and Planetary. Sci. Conf.*, *39*, #2291.

Ernst, C.M. and Schultz, P.H. (2007) Temporal and spatial resolution of the early-time impact flash: Implications for light source distribution, *Lunar and Planetary. Sci. Conf.*, *38*, #2353.

Schultz, P.H., Eberhardy, C.A., and **Ernst, C.M.** (2007) Initial stages of the Deep Impact collision, *Lunar and Planetary. Sci. Conf.*, *38*, #1890.

Ernst, C.M., Schultz, P.H., A'Hearn, M.F., and the Deep Impact Science Team (2006) Photometric evolution of the Deep Impact flash, *Lunar and Planetary. Sci. Conf.*, *37*, #2192.

Schultz, P.H., **Ernst, C.M.**, A'Hearn, M.F., Eberhardy, C.A., Sunshine, J.M., and the Deep Impact Team (2006) The Deep Impact collision: A large-scale oblique impact experiment, *Lunar and Planetary. Sci. Conf.*, 37, #2294.

Ernst, C.M., Schultz, P.H., the Deep Impact Team (2005) Photometric evolution of the Deep Impact flash *Bulletin of the American Astronomical Society*, *37*, 709.

Schultz, P.H., **Ernst, C.M.**, Eberhardy, C.A., Sunshine, J.M., A'Hearn, M.F., and the Deep Impact Team (2005) The Deep Impact Cratering Experiment on the Comet 9P/Tempel 1, *Bulletin of the American Astronomical Society, 37,* 1484.

Ernst, C.M. and Schultz P.H. (2005) Investigations of the luminous energy and luminous efficiency of experimental impacts into particulate targets, *Lunar and Planetary. Sci. Conf.*, *36*, #1475.

Ernst, C.M. and Schultz P.H. (2004) Early-time temperature evolution of the impact flash and beyond. *Lunar and Planetary. Sci. Conf.*, *35,* #1721.

Schultz, P.H., Sugita, S., Eberhardy, C.A., and **Ernst, C.M.** (2004) Isolating the ricochet-induced vaporization process, *Lunar and Planetary. Sci. Conf.*, *35*, #1946.

Ernst, C.M. and Schultz P.H. (2003) Effect of initial conditions on impact flash decay. *Lunar and Planetary. Sci. Conf.*, *34*, #2020.

Ernst, C.M. and Schultz P.H. (2002) Effect of velocity and angle on light intensity generated by hypervelocity impacts. *Lunar and Planetary. Sci. Conf.*, *33*, #1782.

Ernst, C. M. and Holman, M.J. (1999) Astrometric observations of Kuiper Belt Objects, *Bulletin of the American Astronomical Society, 31,* 1532.

Acknowledgements

In 4th grade I wrote a report on the planets. Tremendously excited about the topic, I must have taken all applicable books out of the library to research every excruciating detail about each planet (there were nine planets back then!). Having completed the paper, I proceeded to work on my poster. In the process, I saved my figure captions under the same name as my paper, destroying my only copy. In the end, after some moments of panic, well-taken research notes dictated to a quickly typing parent saved the day. I guess it didn't traumatize me too much, since I ended up a planetary scientist.

In some roundabout way, this dissertation is like that paper, just expanded by several orders of magnitude. I didn't mistakenly delete the whole thing, but it has involved plenty of research, moments of frustration, the excitement of discovery, panic, and most importantly, outside support. I may be the author of this dissertation, but it was made possible by the friendship and support of so many others that it's impossible to name them all. There are several people who deserve particular mention.

My road to Brown began in Watertown, Massachusetts. **Laura Viklund** and **Maggie Coe** have been my friends for close to 20 years, and helped me to navigate the way through middle and high school. Two Watertown teachers deserve particular mention. **Steve Wilson**, my 9th grade science teacher, was my first true teacher of all things geology. **Peter Clough**, my 8th grade global studies teacher, was the most inspiring teacher I have ever had. Memories of his unwavering enthusiasm, love for teaching, and encouragement continually inspire me to strive to be a better person and to always keep learning. I hope I would have made him proud.

In the spring of 1997 I set foot in Lincoln Field Building as a prospective Brunonian. Little did I know that my visit to the classroom of **Pete Schultz** would end up shaping my entire career. Pete's enthusiasm, energy, and love of discovery are contagious. Through the eleven years I've known him, Pete has been constantly excited about science. If I felt burned out and down about my research, a talk with Pete would always get me pepped back up. Thank you for being supportive, always available for a meeting, and teaching me the ways of experimental cratering…even if you did like to throw things at me.

My education as a planetary scientist has come about thanks to the top-notch professors at Brown. Their expert knowledge, cutting edge research, and inside information about missions have helped to fuel my fascination with space. **Jim Head** taught my very first planetary geology class and later let a curious undergraduate into a planetary seminar. **Carlé Pieters** and **Marc Parmentier** have taught me more than I ever thought I'd know about spectra, small bodies, and geophysics. Though I was never directly instructed by **Jack Mustard** and **Mike Wyatt**, their knowledge and experience have made me a more well-rounded scientist. Though he is not at Brown, many thanks go to Dave Crawford for being my defense savior and outside reader.

The staff of the Brown geology department always made things run easily and smoothly. Without their help and friendship, grad school would have been a much scarier place: **Bill Collins, Nancy Christy, Anne Côté, Ruth Crane, Nancy Fjeldheim, Bill Fripp, Phil Howell, Dorcas Metcalf, Peter Neivert, "Captain" Nancy Picard,** and **Rebekkah Sylvia.**

It may seem strange to acknowledge an organization, but there are several out there that deserve my thanks for keeping me happy and mostly sane through graduate school. **RIPUL**, the **Rolling Stones**, and **Billy's Blue Room** kept me active and made sure that I saw the sun. Thank you to the **Boston Red Sox** and the **New England Patriots** for being wicked awesome and worthy of fan obsession. Before I entered graduate school, neither team had won a championship since 1918. Five championships later, this Boston sports fan is eternally grateful.

I am Ever True to **Elrod T. Snidley**, the **Brown Band**, and everyone who has been a part of it (especially the trombone section). Not many people can say that a band played at their defense party; that's one of the coolest things that's ever been done for me. Along the musical vein, a special thanks to **Matt McGarrell** who allowed a busy graduate student into the wind symphony for a much needed escape from research.

I moved within Providence more times than I would have wished, but I was extremely lucky to have lived with a multitude of fantastic roommates. **Becca Zhukov** brought me in and took care of me during the darkest months of the writing process (and pneumonia). I have never technically lived with **Heidi Tebbe**, but the number of chats we've had make it seem like I did. **Chris Meegan** has been the provider of way too much (tremendously delicious) chocolate. **Lauren Kupersmith** was always up for a catch in the park (or an occasional drive to the ER). **Peter Cheifetz,** a commiseration and lunch partner, will always be my "good roomie" extraordinaire. Life would have been rather dull without the antics and stories of **James Coburn**. Finally, **Amy Przeworski,** deserves special notice for putting up with me for the longest time. Thanks for the millions of talking and venting sessions and for keeping me relatively sane.

I'm very thankful to have found such a wonderful group of fellow graduate students at Brown: **Chris Cooper**, **Jason Dahl**, **Carolyn van der Bogart**, **Brad Thompson**, **Patrick Russell**, **Kate Fishbaugh**, **Sarah Noble**, **Zach Morgan**, **Alyssa Beck**, **Sarah Milkovich**, **Rob Jacob**, **Will Pomerantz**, **Bex Parsons**, **Gil Ghatan**, **Caleb Fassett, Jay Dickson**, **Scott Harris**, **Joe Levy**, **Leah Roach**, **Gareth Morgan**, **Sam Schon**, **Laura Kerber**, **Kate Burgess**, **Bethany Ehlmann**, **Lillian Ostrach**, **Deborah Horowitz**, and many more. Thank you for the LFB lunches, the GCB nights, and everything in between.

Angela Stickle and **Brendan Hermalyn** brought life back to the third floor. Thanks for humoring me by listening to my "advice" and for paving my road to caffeine addiction. **Jenn Anderson** is my scientific role model. Thanks for answering the endless questions of a new graduate student. **Wes Patterson** actually made the trek up to the third floor on many occasions for much needed distractions/visits; he gets thanks even though he tried his best to get us killed in the Grand Canyon.

Three people were my major lifeline during the final phase of grad school and through the dissertation writing process. **Peter Isaacson** is my partner in crime when it comes to New England sports. Thanks for the Sox talk, disc tossing, and late night LFB mental-health-check visits. My appreciation for **Rachel and Allan Klima** is difficult to put into words. We've shared so many talks, games, movies, craft nights, absurd stories, and laughs. Thank you for being amazing friends.

Clara Eberhardy, **Noah Petro**, and **Kelly Wrobel** were on this grad school journey with me from the very beginning. I couldn't have asked for better officemates, colleagues, or friends. From our beginnings together as naïve first years through the many good times and the few bad times, they have inspired me, comforted me, encouraged me, entertained me, and supported me. Thank you for always being there for me.

Last and certainly not least, I thank all of my family for their support throughout my life. **Julie Bruno** has always been the most amazing sister. Thank you for always being there for me and for only occasionally making fun of me for still being in school. Thanks also to **Joe Bruno**, the most recent family addition and the brother I never had.

Most importantly, the biggest thank you belongs to my parents, **David and Jean Ernst**. You've provided me with encouragement, support, humor, friendship, love, the means to start this Brunonian journey, and so much more. I owe you everything. I love you bigger than the sky, and I dedicate this thesis to you.

Preface

Hypervelocity collisions generate extreme conditions at the point of impact. Projectile and target materials are shocked, sheared, and comminuted, undergoing rapid pressure and temperature variations. Heated materials that reach high enough temperatures will emit light in the visible wavelength range. This phenomenon is known as the "impact flash".

Impact flashes have been observed in nature, modeled in computational studies, and created in laboratories. Studying the flash using any one of these approaches has its own strengths and limitations. Naturally occurring impacts are difficult to observe unless they are part of a forecasted event (e.g., lunar impacts related to predictable meteor showers, artificial impacts, Shoemaker-Levy 9 impact into Jupiter). These impacts are relatively rare events that can be observed only from large distances and from limited viewing orientations and resolutions. Additionally, the variables associated with such events are largely unknown and uncontrollable. Such factors make the observation and analysis of natural impacts logistically difficult.

Computational hydrocodes provide unprecedented insights into impact cratering and create impressive simulations of the cratering process. These models can simulate impacts at all scales; however, complications include the difficulty of tracking multiple thermal sources, opacities, available equations of state for the materials involved, and assumptions made to simplify the calculations. Hydrocodes may miss complex processes and must be validated with empirical data.

Due to projectile size and velocity limitations in the laboratory, experiments cannot completely simulate large-scale impacts. Experiments, however, capture complex interactions at all scales and provide one of the few calibrations for computational simulations. Fine-scale physical processes can be examined that otherwise might be overlooked in a theoretical simulation. The laboratory setting also allows for the systematic variation and isolation of variables and processes and the easy reproducibility of initial conditions.

Early experimental impact flash studies used primarily metal targets, which produced flashes of very short duration (<10 μs) [e.g., *MacCormack*, 1963; *Jean and Rollins*, 1970; *Eichhorn*, 1976]. The primary light sources from such impacts are atomic and molecular emissions from vaporized material. Later theoretical investigations also predicted short-duration impact flashes relative to the time of crater formation [*Melosh et al.*, 1993; *Artem'eva et al.*, 2001]. Observations and predictions of such short signals led to the expectation that impact flashes would be extremely short-lived.

Impact flashes caused by thermal emissions will be longer in duration as they continue to radiate while cooling. Typical thermal sources are melt droplets and heated particulates that line the growing transient crater cavity or are ejected above the target surface. For thermal emissions from a blackbody source, the impact flash intensity (I) is given by:

$$I = \sigma T^4 A_s, \tag{1}$$

where T is the temperature, A_s is the effective source area, and σ is the Stephan-Boltzmann constant.

Because the impact flash is a quickly evolving, short-duration phenomenon, it is difficult to examine carefully. If detailed observations can be made, however, the impact flash provides a way to observe the early-time cratering process at very short timescales.

The primary goals of this dissertation are to characterize the evolution of the impact flash caused by impacts into particulate surfaces and to use the flash as a way to examine early-time impact processes. These tasks are undertaken from an experimental approach, by performing impacts at the NASA Ames Vertical Gun Range. The design of this facility allows the variation of impact angle from vertical (90º) to 15º. The study of oblique impacts is essential because the most common impact angle on any planetary surface is 45º and only 0.75% of impacts occur at angles greater than 85º (or less than 5º) [*Gilbert*, 1893; *Shoemaker*, 1962]. Because of the ability to vary impact angle, targets can be correctly oriented with respect to gravity, allowing the use of particulate and layered targets and permitting proper crater growth. Particulate targets better simulate the effect of gravity on the cratering flow field and make better analogs to planetary-scale impacts than solid targets [*Gault and Wedekind*, 1977; *Schmidt and Holsapple*, 1980].

The first three chapters of this dissertation address different aspects of the impact flash evolution: (1) intensity, (2) temperature, and (3) source distribution. In each case, the effects of initial conditions on the flash evolution are evaluated and the results are used to interpret processes controlling the generation and subsequent exposure of the radiating source. The final chapter, Chapter 4, applies the experimental results to interpret the flash created by NASA's Deep Impact mission, which is effectively a planetary-scale impact experiment. The chapters are summarized below.

Chapter 1 investigates the photometric evolution of the impact flash using a photodiode for high temporal resolution. The observed intensity signal demonstrates that impacts into particulate targets can produce relatively long-duration flashes (on the order of milliseconds at laboratory scales). The observed intensity evolution exhibits several components with characteristics (e.g., timing, duration, magnitude, decay rate) that can be directly related to the initial impact conditions. Because of these relationships, the impact flash contains valuable information for remotely investigating an impact event and the physical mechanisms occurring during the early-time cratering process. Impact flash photometry has potential as a remote-sensing tool for assessing the nature of planetary surfaces, whether by natural or man-made impacts.

Chapter 2 directly builds on the results found in Chapter 1 by examining the thermal evolution of the impact flash. Spatially integrated intensity measurements cannot resolve the source of the intensity evolution, i.e., changes in source temperature, area, or a combination of the two. To solve this ambiguity, one of the two variables must also be measured. A multi-filtered photodiode system is used to record the flash intensity through time, thereby allowing the calculation of temperature. The intensity and temperature observations are combined to determine the evolution of the radiating source area. The evolving source controls the early portion of the impact flash intensity signal, while a steadily decaying temperature controls the later-stage intensity signal.

The spatial resolution of the flash is observed in Chapter 3. While photodiodes can record the impact flash at very high time resolution, the resulting intensity observations are spatially integrated over the entire emitting source region. Therefore, direct measurement of the physical distribution and source of the radiating material cannot be determined. An intensified CCD camera system is used to capture very-short exposure images of the impact flash. These images can be used to measure directly the projected area and distribution of the radiating source. The distribution of the radiating source is found to be dependent on the impact angle and the target material.

Finally, the observed and derived relationships found in the experimental studies are used to interpret the impact flash evolution observed during the Deep Impact collision into Comet P/Tempel 1 on July 4, 2005. The Deep Impact flash was of relatively long duration; so, it was both temporally and spatially resolved. Details of the cometary surface, including porosity and broad compositional information, were constrained by examining the impact flash. The results were independently confirmed by other means (spectrometry, ejecta behavior). The laboratory experiments were critical to understanding the underlying processes that caused the observed flash. This represents one successful application of the impact flash as a remote sensing tool. The results from this dissertation can be applied to future remote impact observations (e.g., lunar impacts, LCROSS) and to understanding the underlying early-time impact processes.

References

Artem'eva, N. A., I. B. Kosarev, I. V. Nemtchinov, I. A. Trubetskaya, and V. V. Shuvalov (2001), Light flashes caused by Leonid meteoroid impacts on the lunar surface, *Solar System Research*, *35*(3), 177-180.

Eichhorn, G. (1976), Analysis of the hypervelocity impact process from impact flash measurements, *Planetary and Space Sciences*, *24*, 771-781.

Gault, D. E., and J. A. Wedekind (1977), Experimental hypervelocity impact into quartz sand - II, Effects of gravitational acceleration, in *Impact and Explosion Cratering: Overviews*, edited by Roddy, D. J., R. O. Pepin and R. B. Merrill, pp. 1231-1244, Pergamon Press, New York.

Gilbert, G. K. (1893), The Moon's face, *Bull. Philos. Soc. Wash.*, *12*, 241-292.

Jean, B., and T. L. Rollins (1970), Radiation from hypervelocity impact generated plasma, *American Institute of Aeronautics and Astronautics Journal*, *8*, 1742-1748.

MacCormack, R. W. (1963), Investigation of impact flash at low ambient pressures, *6th Symposium on Hypervelocity Impact*, 613-625.

Melosh, H. J., N. A. Artemieva, A. P. Golub, I. V. Nemchinov, V. V. Shuvalov, and I. A. Trubetskaya (1993), Remote visual detection of impacts on the lunar surface, *LPSC*, *24*, 975-976.

Schmidt, R. M., and K. A. Holsapple (1980), Theory and Experiments on Centrifuge Cratering, *Journal of Geophysical Research*, *85*(B1), 235-252.

Shoemaker, E. M. (1962), Interpretation of lunar craters, in *Physics and Astronomy of the Moon*, edited by Kopal, Z., pp. 283-359, Academic Press, San Diego.

Table of Contents

Chapter 1

Photometry of the Impact Flash

Carolyn M. Ernst

Peter H. Schultz

Department of Geological Sciences

Box 1846

Brown University

Providence, RI 02912

Abstract

When a hypervelocity impact occurs, a visible light flash is produced at the moment of first contact. Analysis of the impact flash can be used to probe the early-time impact process responsible for its generation and evolution. For experimental impacts into metal targets, this flash is of very short duration (on the order of microseconds) because the light sources are mainly atomic and molecular emission lines and bands. In contrast, impacts into non-volatile, particulate targets produce hot thermal sources (heated particulates and melt droplets), resulting in significantly longer-duration flash signals (on the order of milliseconds). The melt produced during impacts at these scales is a dominant contributor to the impact flash, yet is often ignored in theoretical and computational studies. Time-resolved light intensity observations of such impacts reveal three main components to the flash evolution: (1) an early-time spike, (2) a delayed, broad peak, and (3) a long-lasting decay. The early-time spike evolves from the first contact between the projectile and the target, revealed by the transparency of the projectile. The later broad intensity peak and its subsequent decay depend on the distribution and cooling of the radiating source. The properties of these components are highly dependent on initial conditions (e.g., velocity, impact angle, projectile size, target composition, view orientation). When most of the initial impact conditions are known, the remaining variables can be constrained by analyzing the flash photometry. By this method, properties of an impacting body (e.g., size) or planetary surface (e.g., strength or porosity) may be assessed using the impact flash as a remote sensing tool.

1. Introduction

During a hypervelocity impact, a fraction of the projectile's initial kinetic energy is partitioned into the thermal heating and vaporization of both the projectile and the target. If the impact is sufficiently energetic, the heated materials will emit an observable light "flash", which occurs over a very short timescale relative to crater formation. The two major potential radiation sources are emission lines from vapor (atomic and molecular), and thermal emissions from heated particulates, melt, and vapor condensates; this study focuses on these thermal emissions. At sufficient time resolution, the recorded impact flash reveals characteristics that can be related to initial impact conditions (i.e., velocity, impact angle, projectile size and composition, target composition). Because of its short duration, the impact flash provides a means to examine early-time impact processes.

Hypervelocity impact studies rely on three approaches, each with its own strengths and limitations: natural impacts, modeled impacts, and experimental impacts. Naturally occurring impacts are difficult to observe unless they are part of a forecasted event (e.g., lunar meteor shower, Shoemaker-Levy 9 impact into Jupiter). These impacts are relatively rare events that can be observed only from large distances and from limited viewing orientations and resolutions. Additionally, the variables associated with such events are largely unknown and uncontrollable. Such factors make the observation and analysis of natural impacts logistically difficult.

Computational hydrocodes provide unprecedented insights into impact cratering and create impressive simulations of the cratering process. These models can produce impacts at all scales; however, complications include the difficulty of tracking multiple thermal sources, available equations of state and opacities for the materials involved, and assumptions made to simplify the calculations. Hydrocodes may miss complex processes and must be validated with empirical data.

Due to projectile size and velocity limitations in the laboratory, experiments cannot completely simulate large-scale impacts. Experiments, however, capture complex interactions at all scales and provide one of the few calibrations for computational simulations. Fine-scale physical processes can be examined that otherwise might be overlooked in a theoretical simulation. These processes can be observed from many orientations and resolutions and with various instruments. The laboratory setting also allows for the systematic variation and isolation of variables and processes, the easy reproducibility of initial conditions, and the ability to perform many impacts over short timescales. Experimental impacts are thus essential for understanding the processes that generate and control the impact flash.

2. Background

Several early experimental studies devoted to the impact flash used photodiodes to examine the maximum flash intensity at high time resolution [e.g., *Gehring and Warnica*, 1963; *MacCormack*, 1963; *Jean and Rollins*, 1970]. Such studies find a power-law relationship between maximum intensity (I_{max}) and projectile velocity (v):

$$I_{\max} \sim v^{\beta}, \tag{1}$$

where the exponent (β) ranges from 2 to 8 (for velocities between 2 and 7 km/s), and is dependent on the projectile and target materials.

Additional studies employed Van de Graaff generators to accelerate small iron projectiles in order to examine the impact flash over a large velocity range. Microparticles impacting at an angle normal to metal targets (gold and tungsten, from 0.5 to 35 km/s) yield a consistent maximum intensity that increases as a power of impact velocity, where the exponent ranges from 3 to 5 [*Eichhorn*, 1976]. Experiments impacting ice targets at 2 to 65 km/s found a consistent power-law relationship with exponent values of approximately 4 [*Burchell et al.*, 1996].

Baird et al. [1997] used the Rankine-Hugoniot equations to derive a power law relationship between impact intensity and velocity where $\beta = 8$. Although the power law is generally observed, $\beta = 8$ does not always fit experimental observations. This is attributed to the limited wavelength response of the observing photodetectors [*Baird and King*, 1999].

Previous studies of the impact flash extended to only 20 μs after impact [*Kadono and Fujiwara*, 1996]. For hypervelocity laboratory impacts into metal targets, vapor emissions are the primary sources of the impact flash, resulting in very short-duration signals of less than 10 μs [e.g., *MacCormack*, 1963; *Eichhorn*, 1976]. In contrast, laboratory impacts into non-volatile, particulate, silicate targets produce mainly thermal emissions from heated particulates and melt droplets. Flashes produced by thermal sources are noticeably different than those produced by vapor emissions, and are capable of lasting orders of magnitude beyond the penetration time of the projectile [*Ernst and Schultz*, 2003]. Particulate targets are more representative of planetary environments than solid (especially metallic) targets.

Shockwaves compress both the projectile and the target on impact. The resulting shock compression and subsequent release generate very high pressures and temperatures. Both laboratory experiments and theoretical simulations show that peak shock pressures (in both the target and the projectile) decrease with decreasing angle (as measured with respect to the target surface) [e.g., *Schultz*, 1996; *Dahl and Schultz*, 2001; *Pierazzo and Melosh*, 2000b; 2000a]. Despite this decrease, oblique impacts have been shown to enhance target heating and vaporization [*Schultz and Gault*, 1990; *Schultz*, 1996], peak impact flash intensity [*Ernst and Schultz*, 2002], and the area of the radiating source [*Ernst and Schultz*, 2004; *Schultz*, 1996]. Frictional shear heating has been proposed as a cause of this enhancement [*Schultz and Gault*, 1990; *Schultz*, 1996; *Schultz et al.*, 2006], but the importance and role of shear heating has yet to be fully addressed.

The main goals of this study are to characterize the generation and evolution of the impact flash intensity for experimental impacts into non-volatile particulate targets and to determine how specific initial conditions affect the observed impact flash. First, the general characteristics and phenomena associated with the light intensity are examined using time-resolved photometry measurements. The effects of projectile and target variables as well as view orientation are then assessed. Next follow interpretations of the intensity observations with a focus on assessing the radiating source. Finally, applications and implications of the results are considered. This study is restricted to addressing the impact flash intensity; Chapter 2 will address the full evolution of the flash, including temperature and source area evolution as well as its luminous efficiency (luminous energy relative to impact kinetic energy).

3. Experimental Design

Hypervelocity impact experiments were performed using the two-stage light gas gun at the NASA Ames Vertical Gun Range (AVGR). The AVGR is a unique facility that allows significant flexibility in experimental design. Impact angles range from 90º to 15° (measured from the horizontal) and possible impact velocities range up to ~ 6.5 km/s into a horizontal target. Tilting of the target itself permits lower impact angles. Several window ports are positioned above and around the target chamber, thereby allowing a choice of viewing orientation. The atmospheric pressure inside of the target chamber can be varied from 1 bar (~760 Torr) down to a near-vacuum (<0.30 Torr).

The vertically-mounted gun allows for the use of loose particulate targets. Post-shock fragmentation increases at large scales. Hence, particulate targets better simulate the effect of gravity on the cratering flow field and make better analogs to planetary-scale impacts [*Gault and Wedekind*, 1977; *Schmidt and Holsapple*, 1980]. The target chamber is approximately 2.5 meters in diameter and height. The large chamber permits the free expansion of the ejecta and thermal plume without interference from the chamber walls that would otherwise affect later-time observations of the photometric signal [e.g., *Eichhorn*, 1976; *Kadono and Fujiwara*, 1996].

The AVGR and the experimental design are illustrated in Figure 1. A high-speed photodiode system with a spectral range of 350 - 1100 nm recorded the light generated during the impacts. The instrument was positioned primarily at a window port above and slightly uprange of the impact point (A in Figure 1). The view orientation of the photodiode system affects the observed signal, since portions of the radiating material may be obscured by expanding solid and vapor ejecta, by the growing crater cavity, and even by the projectile itself at very early times. In order to assess the effect of view orientation on the observed flash, impacts were also performed with the photodiode positioned perpendicular to the projected oblique impact trajectory at a side window (B in Figure 1).

The light intensity was recorded every 100 ns for up to 2 ms of data per impact. The photodiode field of view is large enough to ensure that all radiating sources remained observable over the recorded time interval. A high-speed video camera (500 frames/sec) also recorded the impacts in order to confirm that the experiments occurred nominally (i.e., the projectiles did not disrupt before impact). The data presented here were acquired over several experimental runs. The measurements were consistent across all runs, thereby confirming the same basic evolution of the flash in all cases.

The experiments for this study covered a range of impact velocities (from 4.05 to 6.14 km/s) and impact angles (90º to 15º). This angular variation is extremely important; in nature only 0.75% of impacts are expected to occur at angles greater than 85º (or less than 5º), whereas 50% should occur between 30º and 60º [*Gilbert*, 1893; *Shoemaker*, 1962]. Pyrex spheres (3.18-6.35 mm diameter, 2.23 g/cm^3) were chosen as projectiles. At these velocities, Pyrex undergoes brittle failure and disrupts completely on impact [*Gault and Wedekind*, 1978; *Schultz and Gault*, 1990], thereby better simulating conditions of larger-scale impacts.

Particulate, uncompacted pumice powder (1.25 g/cm^3 bulk density, with a bimodal grain size distribution at 25 μm and 81 μm) was used as the target material for the majority of the experiments. The predominantly silicate compositions of Pyrex and pumice powder minimize the production of atomic and molecular lines and bands in the visible wavelength range. In addition to pumice powder, pumice blocks (0.62 g/cm^3) and particulate perlite (0.22 g/cm^3, sieved to allow only particles smaller than 800 μm) were used to assess the effect of target porosity and strength on the impact flash evolution. Perlite is a magnesium/aluminum silicate with a composition similar to pumice, but the vesicular structure of individual perlite grains results in a high-porosity target at both particle-to-particle and bulk scales.

To avoid complications due to atmospheric interactions, the experiments were performed under near-vacuum conditions (mostly between 0.30 and 0.70 Torr of air). The examined pressure extremes ranged from a maximum of 3.62 Torr to a minimum of 0.39 Torr with a residual helium atmosphere in order to assess the effect of pressure at these low levels. The low density of helium makes the 0.39 Torr of He atmosphere comparable in density to a 0.03 Torr air atmosphere.

4. Observations

Open-shutter images of the flash for vertical (90º) and 30º impact angles (taken from above and under dark conditions) reveal two apparent source regions of radiation: a bright central area around the impact point and streaks that trace the paths of molten ejecta fragments (Figure 2). Also observable are differences in the source distribution between the two impacts. The radiating sources appear symmetrical for a vertical impact of Pyrex into pumice powder (Figure 2a). In contrast, for a 30º impact under otherwise identical initial conditions the central region is elongated along the direction of impact with the brightest region on the downrange side (Figure 2b). The visible ejecta paths are also concentrated downrange for the oblique case. This comparison illustrates how changes in impact angle affect the distribution of the radiating sources [e.g., *Gault and Wedekind*, 1978]. In order to examine the flash evolution, a photodiode was used to achieve temporal resolution.

4.1 Impact Flash Evolution

Impacts of Pyrex projectiles into pumice powder targets (hereafter, Pyrex/pumice powder impacts) exhibit three common components (Figure 3): (1) an early-time spike, (2) a broad intensity peak, and (3) a long decay signal. Each component represents the effect of multiple processes and depends on initial impact conditions. Here, the general characteristics of these components are described. Interpretations of the observations are deferred to Section 5.

4.1.1 Early-time Spike

The early-time spike is the first observable light, beginning immediately at impact. The spike is short-lived with its decay quickly overtaken by a secondary rise to the broad intensity peak. Under the current experimental conditions, the average spike rise time was ~0.2 μs and its duration ranged from 0.4 - 1.5 μs, which is on the order of the time required for the projectile to travel its own diameter below the pre-impact target surface; therefore, the early-time spike component of the impact flash is related to the first contact between the projectile and the target.

4.1.2 Intensity Peak

The delayed broad intensity peak dominates the appearance of the light curves under the explored conditions. The maximum intensity is delayed from first contact by 10 - 50 μs and its FWHM duration ranges from 100 - 400 μs (the timing and the duration are highly dependent on impact angle). The magnitudes of the maximum intensity and the spike appear unrelated in this study, although the fast evolution of the spike may lead to its peak not being completely resolved. Such long-lasting, delayed peaks were not previously observed for impacts into solid targets [*Gehring and Warnica*, 1963; *MacCormack*, 1963; *Eichhorn*, 1976; *Jean and Rollins*, 1970; *Kadono and Fujiwara*, 1996]. The materials used in those studies generated only a brief early-time spike; either no secondary intensity rise occurred (except one due to interference by chamber walls) or the observations were concluded before one could be detected. The predominant sources of radiation were likely short-lived atomic and molecular emission lines.

4.1.3 Intensity Decay

Once the maximum intensity is reached, the signal decays slowly over time, lasting beyond the 2 ms window of observation. For comparison, craters of this size under these conditions usually form in approximately 90 ms. The current experiments demonstrate that impacts into particulate targets can produce relatively long-duration flashes, which has significant implications for lunar impact flash observations (discussed in Section 6).

4.2 Initial Condition Effects

The characteristics of the three impact-flash components depend on initial conditions. Assessing the effect of initial conditions is a strategy for identifying the underlying early-time processes generating and controlling the appearance of the impact flash. The following initial conditions were varied: velocity, angle, target material, the view orientation of the photodiode, and the ambient pressure. The resulting observations are detailed in this section while interpretations are again deferred until Section 5.

4.2.1 Velocity Effects

The maximum intensity (I_{max}) of the flash occurs during the delayed intensity peak for high-speed impacts (4 – 7 km/s). The maximum intensity increases with impact velocity, following a power-law dependence as described in Equation 1 (Figure 4). The observed values of the exponent, β, range from 5 to 6. All of the examined angles and diameters resulted in consistent β values. For 90º and 75º angles, I_{max} values fall along the same trendline (Figure 4a). The impact angle does not start to produce a noticeable intensity offset until it reaches 60º (b). The most data were obtained at 30º (c), and these impacts exhibit the highest I_{max} values for a given velocity. By 15º (d), the trend of increasing intensity with decreasing angle no longer holds. Impacts at 90º and 30º using smaller projectiles (e and f) exhibit the same β values at lower intensities. This parallel offset of impacts using different projectile diameters was also seen by *Jean and Rollins* [1970].

Baird et al. [1997] derived a value of β = 8; nevertheless, the experimentally observed exponent lies within the range (2 to 8) found in previous studies using different materials and larger velocity ranges [e.g., *Gehring and Warnica*, 1963; *MacCormack*, 1963; *Jean and Rollins*, 1970; *Eichhorn*, 1976]. It is important to note that the relationships measured in previous studies correspond to a maximum intensity that occurs very close to the initial contact, not to a delayed maximum intensity as measured here.

For lower velocity impacts (~1 to 2 km/s), frictional heating along the surface contact between the projectile and the target dominates the observed signal. In the laboratory, the velocity difference between 5 km/s and 2 km/s results in a drastic reduction in the flash intensity and duration (Figure 5). At such low velocities, the spike becomes the point of highest intensity. A delayed peak is still observed, but its peak intensity remains lower than that of the spike.

4.2.2 Impact Angle Effects

Figure 6 provides direct comparisons for the flash evolution from 90º to 15º. The maximum flash intensity increases with decreasing impact angle, except below 30º. Impact angles at 90º and 75º produce similar evolutions, with 75º displaying a slightly higher I_{max} occurring at an earlier time. Moderate differences in the evolution appearance emerge from 60º to 45º with I_{max} continuing to rise and occurring at earlier times for lower angles. By 30º, not only does the I_{max} vary considerably from 90º to 30º, but also the duration of the broad peak is much shorter (the FWHM at 90º lasting 3 - 4 times longer than at 30º). At 15º, the maximum intensity occurs at an earlier time, but the observed angular trend of the maximum intensity no longer holds. There is thus a critical angle for these materials between 15º and 30º, below which the cratering process changes significantly. The decay signals are better displayed on a logarithmic scale (Figure 6b).

The decay rates are comparable from 90º to 45º angles. At 30º and 15º, the intensity decays at a slower rate.

4.2.3 Target Effects

Variations of target properties can be used to assess the evolution of the radiating source region. Different targets were chosen for their specific properties, including perlite granules (high porosity) and a solid pumice block (strength). The differences between the intensity profiles for different target materials are illustrated in Figure 7.

The impact flash is highly dependent on target properties. Both new targets produce significantly less luminous energy (at all times) and shorter-duration signals than a pumice powder target, with distinct decay rates all faster than that for pumice powder. Consequently, it is possible to distinguish among different target types if all other initial conditions are known.

4.2.4 View Orientation Effects

Observations from above ensure maximum exposure of the impact flash. A lower-angle view orientation should decrease the observed flash intensity since the walls of the transient crater and expanding ejecta will partly mask the radiating source. Here, the effect of the view orientation on the observed impact flash for both vertical and oblique impacts is addressed. Comparing the flash intensity and evolution from different view orientation provides a strategy to assess the spatial distribution of the radiating source material.

A series of experiments used Pyrex projectiles impacting pumice powder targets at angles of 90º (vertical), 45º, and 30º with velocities between 5.10 and 5.40 km/s. The photodiode was positioned in two locations, "top view" (A) and "side view" (B), as indicated in Figure 1. The side view position is elevated ~15º form horizontal.

The flash appears significantly fainter when observed from the side (Figure 8). Over the entire 1 ms observed, the side-view intensity never matches the level of the top view signal. Because the most of the observed signals decay steadily after ~50 μs, the light curves are only displayed out to 150 μs in order to better resolve the early-time features.

There is a clear difference between the total intensity (and thus the luminous efficiency) for the two view orientations, with the greatest disparity for the 90º impact (Figure 8a). The total intensity out to 150 μs appears 9 times lower from the side view. When integrating over 1 ms, the difference is lower though still significant (the difference drops from 9 to ~6 times lower).

Maximum and overall intensity levels increase for the oblique impacts for both top and side views (45º and 30º, Figures 8b,c). The delayed intensity peak can be observed from the side at these angles. The timing of the delayed intensity peak is the same for both 45º impact views. For the 30º impact, however, the side view signal reaches a peak while the top view intensity continues to rise. The differences in intensity from the side to the top views are 6 times and 3 times less for the 45º and 30º cases respectively (out to 150 μs). Consequently, the top view always yields a greater flash intensity with the greatest difference occurring at lower impact angles.

4.2.5 Ambient Pressure Effects

Impact flash intensity may be enhanced by the residual ambient atmosphere [*Schultz*, 1996]. This enhancement results from vapor and fine ejecta coupling their kinetic energy of expansion to internal heating of the surrounding atmosphere. Figure 9 reveals, however, that atmospheric pressure does not affect the maximum intensity over the examined pressure range (0.3 to 3.6 Torr) for the silicate targets used here.

As a further test, the impact chamber was refilled with 100 Torr of helium and then purged to 0.39 Torr, effectively reducing the atmospheric density equivalent to 0.03 Torr of air. Under these conditions, there was no significant effect on the maximum intensity (Figure 9), although more data are needed. This observation is consistent with the results of *Gehring and Warnica* [1963], but inconsistent with other findings [*Eichhorn*, 1976; *MacCormack*, 1963]. It should be noted that the latter studies (those finding a pressure dependence) use metal projectiles and targets, whereas the present study and *Gehring and Warnica* [1963] use primarily non-metallic materials.

5. Discussion

5.1 Early-time spike

The early-time spike is enigmatic. The duration of the spike is so short that sub-microsecond time resolution is necessary to capture its true shape and magnitude. Increasing impact velocity and projectile diameter (both of which increase the impact kinetic energy) generally result in higher intensity spikes, but no trends are evident. A larger projectile also leads to longer spike duration. While changes in impact angle have no apparent relation to the spike intensity, impact angle does affect its duration. This effect relates to the rise to the delayed intensity peak. For 30º impacts, the beginning of the secondary intensity rise overtakes the spike decay signal up to 1 μs earlier than for a vertical impact.

Many of the 30º light curves exhibit double spikes: the first is equivalent to those described above, and the second occurs ~1.2 - 1.4 μs after impact, appearing superimposed onto the secondary rise. The double spike feature may indicate small irregularities in the target surface, or more likely is related to the failure of the Pyrex projectile at a low angles.

Because this spike is observable from both the top and side views, it must develop from the moment of first contact before the projectile has penetrated into the target. Similar spikes are observed during metal impacts, for which the proposed origin is a small, high-speed jet of highly shocked material ejected on impact [*Jean and Rollins*, 1970]. This phenomenon is known as "jetting" and is caused by convergent shocks [*Gault and Heitowit*, 1963; *Vickery*, 1993; *Sugita and Schultz*, 1999].

The mass of material involved in the jetting process is extremely small. The light it emits is primarily in the form of emission lines [*Sugita and Schultz*, 1999], which would not contribute significant light to the flash signal. Here, jetting is unlikely to be the source of the spike for the current experiments. The observed effects of initial conditions on the spike are also inconsistent with a jetting origin. Due to confinement by the target surface, observed jetting should be lower for vertical impact angles than for oblique angles, yet the magnitudes of the observed spikes are comparable for 90º and 30º impacts. Also, velocities of 2 km/s should be too low to produce jetting; however, significant spikes have been observed at these velocities (e.g., Figure 5).

Experiments using copper projectiles produced impact flashes without early-time spikes (but by later times the signals are comparable). Copper and Pyrex projectiles differ in density, composition, and opacity. Higher-density projectiles create higher peak pressures that should generate more jetting. No spike is observed for copper projectiles, indicating that jetting is not the most probable source of the spike for the Pyrex impacts.

The projectile opacity is perhaps the more important factor. Because Pyrex projectiles are transparent, a photodiode positioned above the impact point has a direct view of the actual point of contact between the projectile and the target. This point experiences the highest pressure and temperature of the impact event, and the spike represents a unique way to directly observe these conditions. The origin of the spike is investigated further in Chapter 3.

5.2 Radiating Source

Thermal emissions dominate the observed flash throughout its duration for these impacts. The emissions sources are melt droplets and heated particulates that line the growing transient crater cavity or are ejected above the target surface. Similar thermal sources have been observed spectroscopically in laboratory scale impacts [*Sugita et al.*, 1998; *Schultz et al.*, 1996] and analytically modeled for lunar impact flash observations [*Yanagisawa and Kisaichi*, 2002].

For thermal emissions from a blackbody source, the impact flash intensity (I) is directly related to the temperature (T) and the radiating source area (A_s):

$$I = \sigma T^4 A_s, \tag{2}$$

where σ is the Stephan-Boltzmann constant. The maximum intensity dependence on velocity primarily reflects the increase in the total energy partitioned into heating the target. Higher energy generates higher temperatures and more heated mass (larger source area); both factors lead to a higher intensity signal. Impacts at ~2 km/s generate temperatures too low to produce significant radiation in the visible wavelength range, especially as the source cools. Consequently, the maximum intensity for such an impact coincides with the spike and the delayed intensity peak is subdued.

Whether the delayed intensity signal is caused by an increase in temperature, an increase in source area, or a combination of the two cannot be directly determined using only the spatially integrated data gathered in this study; however, an increasing source area is physically more realistic (either by the increase in the source or the redistribution and exposure of material) than a delayed temperature increase.

The decay portion of the flash evolution represents the cooling of the radiating source. After the intensity peak, the impact flash signal decays as a power law with time, given by:

$$I \sim t^{-\alpha}, \quad (3)$$

where α is the intensity-decay exponent (a larger value of α corresponds to a faster decay). This exponent is constant for a given set of initial conditions, but varies with parameters including impact angle and target properties. The effect of initial conditions on the appearance of the intensity evolution can be used to assess the sources of and processes controlling the delayed maximum intensity and the decay with the available data.

5.2.1 Impact Angle Effects

The maximum intensity and the rise time to this maximum both depend on the impact angle: at a lower angle there is a faster rise to a higher maximum intensity. The rise time decreases systematically with impact angle (see Figure 6). Figure 10 reveals that the rise time is related to a $\sin\theta$ term. An expression for a dimensionless time (τ) can incorporate this angle-dependent length scale (d):

$$\tau = t\frac{v}{a\sin\theta} = t\frac{v}{d}, \tag{4}$$

where a and θ are the projectile diameter and impact angle, respectively. The use of τ causes the maximum intensities for all angles to coincide (Figure 11).

For the case of the rise time, the $\sin\theta$ term must be related to a length scale and not to the vertical component of velocity since the term must be in the denominator. It may be related to the distribution of the melt volume (V_m):

$$V_m \sim A_m d, \tag{5}$$

where A_m is the area of the melted mass. The d value will relate to the depth at which the projectile couples its energy to the target, which is shallower for lower impact angles. A shallower depth leads to faster exposure of heated material to the detector, and thus a shorter rise time to its maximum intensity.

The maximum intensity increases with a decreasing impact angle (90º to 30º), which indicates a relation to the horizontal component of the velocity (Figure 11). This trend does not hold for 15º. At such low angles, the projectile retains much of its initial kinetic energy after impact, i.e., its energy remains largely decoupled from the target [*Schultz and Gault*, 1990]. Consequently, less energy is partitioned to heating the target.

The increase in maximum intensity appears to relate to cosθ for angles from 75º to 30º. Such a dependence could correspond to an increase in the exposed area of the heated material. The effect of impact angle may reflect the distribution and location of the radiating source. The penetration depth of a projectile is greater for higher impact angles; therefore, the transient crater will be narrowest and deepest for a vertical impact [*Schultz et al.*, 2005]. If the main radiating source is located inside of the transient crater, the source will be confined to a smaller exposed area. At lower impact angles, the transient crater opening is shallower and elongated parallel to the direction of impact (for pumice powder targets). The radiating material will be spread over a greater area, will be located at a shallower depth, and more will be ejected from the crater (mostly downrange). All of these factors result in the greater exposure of radiating material to the detector. Frictional shear heating and the effects of impactor ricochet (both of which increase with decreasing impact angle) contribute to enhanced vaporization of carbonates [*Schultz*, 1996; *Schultz et al.*, 2006] and could also contribute to the observed maximum intensity dependence.

5.2.2 Target Effects

The lower intensity output for impacts into perlite granules is likely due to the greater initial penetration depth of the more porous perlite targets [*Schultz*, 2003; *Schultz et al.*, 2005; *Ernst and Schultz*, 2007]. The final crater for an impact into a perlite target is significantly shallower and wider than the transient crater due to rim collapse and high-angle ejecta fallback. Nevertheless, the transient crater is deep and narrow with most of the heated material driven downward, blocked from view [*Schultz et al.*, 2005]. As a result, the maximum intensity observed from above is lower and the total flash duration is significantly shorter. In contrast, for pumice powder the heated material lines the transient cavity and remains visible to the detector.

For the pumice block, heated particulates are compressed and driven into the target, again hidden from view. Less ejecta are also produced for the strength controlled targets. The difference between the pumice powder and pumice block impacts demonstrates that solid pumice cannot be used to directly simulate the impact light evolution of a loose particulate target. In both cases, the radiating source is largely driven below the surface. Consequently, a low-intensity signal does not necessarily indicate that there is very little heated material. It also could indicate that the source is almost completely obscured from view.

5.2.3 View Orientation Effects

A flash observed from above always has a higher intensity than a flash observed from the side. Thus, more radiating material (larger area) is exposed to the top view photodiode. The intensity differences between views demonstrate that the bulk of the signal source is blocked by the transient crater walls and/or by an optically thick ejecta curtain for the side view.

The intensity difference between top and side views of an oblique impact is less than that for a vertical impact. This intensity difference can be attributed to evolution of the transient crater and downrange ejecta. Because the transient crater is deepest (and narrowest) during a 90º impact, most of the radiating material remains trapped inside the transient crater, blocked from the side view photodiode. As impact angle decreases, the projectile does not penetrate as deeply and its momentum launches heated ejecta out of the cavity and downrange [*Schultz et al.*, 2005].

5.3 Summary

The current findings only apply to the dominant thermal signal, not to light emitted from vapor or condensates produced during an impact. Silicate targets are used to minimize vaporization, but the amount of melt and vapor produced can be scaled by the velocity of the impactor [*Pierazzo et al.*, 1997]. The total mass of melt will remain greater than the total mass of vaporization products for similar non-volatile materials [*O'Keefe and Ahrens*, 1977]. Even though higher velocities generate more vapor (and condensates as thermal sources), the luminous energy will be dominated by the greater mass of heated melt. An exception, however, would be easily volatilized targets where solid condensates may not form [e.g., *Schultz et al.*, 2007].

The source of the impact flash for the present experiments is thermal emissions from melt droplets and heated particulates in a rapidly expanding thermal plume (hot dust) above the impact point and lining the transient crater walls. The early-time spike evolves from the first contact between the projectile and the target, revealed by the transparency of the projectile. The later broad intensity peak and its subsequent decay depend on the distribution and cooling of the radiating source. The depth at which the projectile couples to the target controls the thermal sources, along with the growth and shape of the developing transient crater. The flash evolution at different impact angles is sufficiently distinct such that the relative angle of impact can be easily identified for impacts of otherwise identical conditions observed by the same setup.

6. Applications and Implications

The results of these experiments demonstrate that the photometric evolution of the impact flash strongly depends on initial impact conditions. Conversely, when most of the initial conditions are known, the impact variables may be constrained by analyzing the flash photometry. By this method, the nature of a planetary surface (e.g., strength or porosity) may be assessed using the impact flash as a remote sensing tool. In addition, the derived target conditions can be considered along with simultaneous spectroscopic measurements to examine the composition of materials at or just below the surface of the target [e.g., *Schultz et al.*, 1996].

6.1 Impact Flash as a Remote Sensing Tool

Impact flash photometry was applied successfully as a remote sensing tool to analyze data from NASA's Deep Impact (DI) mission. On July 4, 2005, the DI mission performed a planetary-scale impact experiment by placing a 370 kg projectile of known density, size, and composition into the path of comet P/Tempel 1, which had a velocity of 10.3 km/s relative to the projectile [*A'Hearn et al.*, 2005]. Instruments on board the flyby spacecraft observed the comet prior to, during, and after the impact. These instruments recorded the spatial and temporal evolution of a prolonged, complex impact flash.

Self-luminous material was observed to radiate for more than 500 ms [*A'Hearn et al.*, 2005; *Ernst and Schultz*, 2007]. Analyses determined the impact flash to be consistent with laboratory experiments into highly porous targets. This result suggests that the Tempel 1 surface is highly porous [*Ernst and Schultz*, 2007], a constraint that agrees with conclusions drawn by other means (spectroscopy, ejecta curtain behavior)

[*Schultz et al.*, 2007; *Richardson et al.*, 2007] and predicted prior to the encounter [*Schultz et al.*, 2005]. The DI flash is discussed in depth in Chapter 4.

The upcoming Lunar Crater Observing and Sensing Satellite (LCROSS) mission may provide another opportunity to observe a manmade planetary-scale impact flash [*Colaprete et al.*, 2008]. The LCROSS mission will have known projectile variables and a generally known silicate surface with unknown water/ice content. The impact flash should be energetic enough to be detected by the observing spacecraft. The resulting photometry will contribute to understanding meter-scale topography, strength, and porosity as well as presence of water/ice at the impact site. LCROSS will also provide a second data point for controlled, planetary-scale experiments.

6.2 Lunar Impacts

Lunar impacts can be studied using impact flash photometry. This has implications for determining the sizes of meteor streams, which can be used to assess impact hazards for manned lunar missions [*Cooke et al.*, 2007]. Because the Moon has no atmosphere, many small meteoroids, both sporadic and associated with meteor showers, impact its surface. There have been many telescopic observations of meteoroids impacting the Moon [e.g., *Bellot Rubio et al.*, 2000; *Ortiz et al.*, 2002; *Yanagisawa and Kisaichi*, 2002]. Though these collisions typically occur at velocities much higher than those possible in laboratories (~16.9 km/s for sporadic meteoroids [*Steel*, 1996], as high as ~ 72 km/s for shower meteoroids), experiments still can be used to interpret the observations. In such cases, the properties of the projectiles (mass, size, composition) are the unknown quantities, whereas the lunar surface is relatively well known. Several observed lunar impacts produced "afterglows" lasting for several exposure frames [*Yanagisawa and Kisaichi*, 2002], with one signal lasting for over 600 ms [*Ortiz et al.*, 2002]. These low-resolution light curves exhibit the same overall characteristics as those observed in the laboratory experiments: a fast rise to an intensity peak and a prolonged decay signal.

Earth-based telescopes have a fixed view orientation with respect to the Moon, but the location of the impact effectively changes the view orientation due to the curvature of the lunar surface. An impact near the lunar limb will appear to have far less luminous energy than an identical impact near the sub-Earth point. A single value for the luminous efficiency is often assumed in order to calculate an impactor mass [e.g., *Bellot Rubio et al.*, 2000]. An observed luminous energy from an impact near the limb will underestimate the impactor mass for a given luminous efficiency. Because flash duration is also affected by view orientation, an impact viewed from above will also appear to last longer than an identical impact observed from the side. If the sensitivity is too low, one might only record the early-time spike.

Just as in the present study, observed impact flashes cannot be fully interpreted without measurements of the temperature or radiating source area. The laboratory experiments, however, demonstrate that the existence of such long afterglows in the recorded lunar flashes should be an expected component of the evolving impact-generated thermal sources (large quantities of melted and partially melted incandescent ejecta droplets), in addition to an evolving vapor plume and condensation within the cooling vapor. Even though the initial coupling in laboratory experiments does not fully replicate natural impacts, the long duration of the thermal plume in both experimental and lunar impacts must represent the cooling of molten ejecta. Longer lasting lunar impact flashes (600 ms) as compared to the laboratory experiments (2 ms) can be attributed to a much greater amount of melt and heated particulates, due to the much higher impact energy (both increased mass and velocity).

7. Conclusions

The results from high-speed photometry of impact experiments demonstrate that the impact-generated light intensity lasts much longer than the brightest “flash” at impact. The term “impact flash” can be misleading, at least for impacts into non-volatile particulate targets. The initial flash is created by high-temperature thermal emissions that transition to a much longer-lasting signal affected by the evolving thermal sources (retained melt, heated particulate ejecta, and the evolution of exposed material).

There are three main components observed in the impact flash light curves through time: an early-time spike, a delayed, broad intensity peak, and a long decay signal. The appearances of these components depend on initial conditions. The early-time luminous spike is caused by the moment of first contact between the projectile and the target. Its detection here is due mainly to the use of translucent projectiles; opaque projectiles obstruct the signal from reaching the detector. The spike therefore provides a way to observe the interface between the projectile and the target.

The shape of the intensity peak depends on projectile and target variables. The subsequent growth of the thermal source controls its evolution. The maximum intensity has a power-law dependence on velocity and is dependent on the horizontal component of the impact angle. This dependence suggests the possible contribution of frictional shear heating and the influence of the transient crater geometry on the exposed source area. The rise time to the maximum intensity increases with angle and may be related to the original coupling depth of the projectile.

The decay rate follows a power-law function and is controlled by the cooling of the radiating source. The initial decay signal exponent, α, is comparable for impact angles of 90º to 45º, but angles of 30º and 15º impacts exhibit slower decays. The decay exponent also depends on the physical properties of the target (solid versus particulate, and composition).

Detectors viewing from above an impact observe not only radiating ejecta but also material contained within the transient crater (which lies below the pre-impact surface plane). In side views, most of the radiating material (especially in the 90º case) remains hidden by the crater walls and the emerging optically thick ejecta curtain. Consequently, view orientation plays a large part in the observed flash magnitude and duration.

The impact flash provides valuable information for investigating an impact event and the physical mechanisms occurring during the early-time cratering process. Impact flash photometry is a valuable (but non-unique) remote sensing tool for assessing the nature of the impacted surface, whether by natural or man-made impacts. If the initial impactor variables are well understood, measurements of the impact flash can constrain unknown target properties.

Acknowledgements

The authors would like to thank the dedicated technicians at the NASA Ames Vertical Gun Range (D. Holt, R. Smythe, D. Bowling, C. Cornelison, and J-P. Wiens) and William Patterson of the Brown University Division of Engineering. This material is based on work supported by the NASA Planetary Geology and Geophysics Program (NAGS-11538) and the NASA Graduate Student Researchers Program (04-6011H).

References

A'Hearn, M. F., and 32 coauthors (2005), Deep Impact: Excavating comet Tempel 1, *Science*, *310*(5746), 258-264.

Baird, J. K., G. R. Hough, and T. R. King (1997), Velocity dependence of impact fluorescence, *International Journal of Impact Engineering*, *19*(3), 273-276.

Baird, J. K., and T. R. King (1999), A Wien displacement law for impact radiation, *International Journal of Impact Engineering*, *23*, 39-49.

Bellot Rubio, L. R., J. L. Ortiz, and P. V. Sada (2000), Observation and Interpretation of Meteoroid Impact Flashes on the Moon, *Earth, Moon, and Planets*, *82-83*, 575-598.

Burchell, M. J., M. J. Cole, and P. R. Ratcliff (1996), Light Flash and Ionization from Hypervelocity Impacts on Ice, *Icarus*, *122*, 358-365.

Colaprete, A., G. Briggs, K. Ennico, D. Wooden, J. Heldmann, L. Sollitt, E. Asphaug, D. Korycansky, P. Schultz, A. Christensen, K. Galal, and the LCROSS Team (2008), An Overview of The Lunar Crater Observation and Sensing Satellite (LCROSS) Mission – A Mission to Investigate Lunar Polar Hydrogen, *LPSC*, *XXXIX*, 1838.

Cooke, W. J., R. M. Suggs, R. J. Suggs, W. R. Swift, and N. P. Hollon (2007), Rate and Distribution of Kilogram Lunar Impactors, *LPSC*, *XXXVIII*, #1986.

Dahl, J. M., and P. H. Schultz (2001), Measurement of stress wave asymmetries in hypervelocity projectile impact experiments, *International Journal of Impact Engineering*, *26*, 145-155.

Eichhorn, G. (1976), Analysis of the hypervelocity impact process from impact flash measurements, *Planetary and Space Sciences*, *24*, 771-781.

Ernst, C. M., and P. H. Schultz (2002), Effect of velocity and angle on light intensity generated by hypervelocity impacts, *LPSC*, *XXXIII*, #1782.

Ernst, C. M., and P. H. Schultz (2003), Effect of initial conditions on impact flash decay, *LPSC*, *XXXIV*, #2020.

Ernst, C. M., and P. H. Schultz (2004), Early-time temperature evolution of the impact flash and beyond, *LPSC*, *XXXV*, #1721.

Ernst, C. M., and P. H. Schultz (2007), Evolution of the Deep Impact flash: Implications for the nucleus surface based on laboratory experiments, *Icarus*, *190*, 334-344.

Gault, D. E., and J. A. Wedekind (1977), Experimental hypervelocity impact into quartz sand - II, Effects of gravitational acceleration, in *Impact and Explosion Cratering: Overviews*, edited by Roddy, D. J., R. O. Pepin and R. B. Merrill, pp. 1231-1244, Pergamon Press, New York.

Gault, D. E., and J. A. Wedekind (1978), Experimental studies of oblique impact, *Proceedings of the Lunar Planetary Science Conference*, *9*, 3843-3875.

Gehring, J. W., and R. L. Warnica (1963), An investigation of the phenomena of impact flash and its potential use as a hit detection and target discrimination technique, *6th Symposium on Hypervelocity Impact*, 627-681.

Gilbert, G. K. (1893), The Moon's face, *Bull. Philos. Soc. Wash.*, *12*, 241-292.

Jean, B., and T. L. Rollins (1970), Radiation from hypervelocity impact generated plasma, *American Institute of Aeronautics and Astronautics Journal*, *8*, 1742-1748.

Kadono, T., and A. Fujiwara (1996), Observation of expanding vapor cloud generated by hypervelocity impact, *Journal of Geophysical Research*, *101*(E11), 26,097-26,109.

MacCormack, R. W. (1963), Investigation of impact flash at low ambient pressures, *6th Symposium on Hypervelocity Impact*, 613-625.

O'Keefe, J. D., and T. J. Ahrens (1977), Impact-induced energy partitioning, melting, and vaporization on terrestrial planets, 8th *Lunar Science Conference Proceedings*, 3357-3374.

Ortiz, J. L., J. A. Quesada, J. Aceituno, F. J. Aceituno, and L. R. Bellot Rubio (2002), Observation and interpretation of Leonid impact flashes on the Moon in 2001, *The Astrophysical Journal*, *576*, 567-573.

Pierazzo, E., A. M. Vickery, and H. J. Melosh (1997), A reevaluation of impact melt production, *Icarus*, *127*, 408-423.

Pierazzo, E., and H. J. Melosh (2000a), Understanding oblique impacts from experiments, observations, and modeling, *Annual Review of Earth and Planetary Sciences*, *28*, 141-167.

Pierazzo, E., and H. J. Melosh (2000b), Melt production in oblique impacts, *Icarus*, *145*, 252-261.

Richardson, J. E., H. J. Melosh, C. M. Lisse, and B. Carcich (2007), A ballistics analysis of the Deep Impact ejecta plume: Determining Comet Tempel 1's gravity, mass, and density, *Icarus*, *190*(2), 357-390.

Schmidt, R. M., and K. A. Holsapple (1980), Theory and Experiments on Centrifuge Cratering, *Journal of Geophysical Research*, *85*(B1), 235-252.

Schultz, P. H., and D. E. Gault (1990), Prolonged global catastrophes from oblique impacts, in *Global Catastrophes in Earth History: An Interdisciplinary Conference on Impacts, Volcanism, and Mass Mortality*, edited by Sharpton, V. L. and P. D. Ward, pp. 239-261, Special Paper of the Geological Society of America.

Schultz, P. H. (1996), Effect of impact angle on vaporization, *Journal of Geophysical Research*, *101*(E9), 21,117-21,136.

Schultz, P. H., M. A. Adams, J. W. Perry, J. D. Goguen, and S. Sugita (1996), Impact flash spectroscopy, *LPSC*, *XXXVII*, 1149-1150.

Schultz, P. H. (2003), Transient crater growth in low density targets, *LPSC, XXXIV*, #2067.

Schultz, P. H., C. M. Ernst, and J. L. B. Anderson (2005), Expectations for crater size and photometric evolution from the Deep Impact collision, *Space Science Reviews*, *117*, 207-239.

Schultz, P. H., S. Sugita, C. A. Eberhardy, and C. M. Ernst (2006), The role of ricochet in impact vaporization, *International Journal of Impact Engineering*, *33*, 771-780.

Schultz, P. H., C. A. Eberhardy, C. M. Ernst, M. F. A'Hearn, J. M. Sunshine, and C. M. Lisse (2007), The Deep Impact oblique impact cratering experiment, *Icarus*, *190*, 295-333.

Shoemaker, E. M. (1962), Interpretation of lunar craters, in *Physics and Astronomy of the Moon*, edited by Kopal, Z., pp. 283-359, Academic Press, San Diego.

Steel, D. (1996), Meteoroid Orbits, *Space Science Reviews*, *78*, 507-553.

Sugita, S., P. H. Schultz, and M. A. Adams (1998), Spectroscopic Measurements of Vapor Clouds Due to Oblique Impacts, *Journal of Geophysical Research*, *103*(E8), 19,427-19,441.

Sugita, S., and P. H. Schultz (1999), Spectroscopic characterization of hypervelocity jetting: Comparison with a standard theory, *Journal of Geophysical Research*, *104*(E12), 30,825-30,845.

Yanagisawa, M., and N. Kisaichi (2002), Lightcurves of 1999 Leonid impact flashes on the Moon, *Icarus*, *159*, 31-38.

Figure Captions

Figure 1. Sketch of the Ames Vertical Gun Range (AVGR) target chamber showing the gun and viewing ports. Projectiles can be fired at 90º (vertical) to 15º (in 15º increments) and at velocities up to 6.5 km/s. The target is located on a platform inside of the vacuum chamber. A photodiode viewed the impacts through a window on the top of the chamber ("top view", A) and the high-speed video camera observes through a window in the side wall ("side view", B).

Figure 2. Open shutter images of Pyrex/pumice powder impacts. The images were taken without lights from a position above the impact point. Two radiating sources are seen: a central bright area around the impact point and streaks that trace the paths of molten ejecta fragments. (a) For a 90º impact angle, the radiating sources appear symmetrical. (b) For a 30º impact angle, the radiating sources are elongated along the direction of impact (indicated by the arrow) and concentrated downrange.

Figure 3. Plot of the light intensity evolution of (a) the first 2 ms and (b) the first 100 μs of a 30º, 6.35-mm Pyrex/pumice powder impact at 5.96 km/s. Three main components can be seen: (1) an early-time spike (duration = 5 μs); (2) a broad intensity peak that dominates the signal (maximum intensity time = 18 μs, FWHM = 100 μs); and (3) a long-lasting decay signal that lasts well beyond the 2 ms of observations presented here.

Figure 4. Plot of the maximum flash intensity as a function of impact velocity for Pyrex/pumice powder impacts. The data follow power law relationships (i.e., Equation 1) and the slopes of the trendlines represent β values between 5 and 6. The β value is consistent over angles from 90º to 15º and for different projectile diameters: (a) 6.35 mm, 90º and 75º, (b) 6.35 mm, 60º, (c) 6.35 mm, 45º and 30º, (d) 6.35 mm, 15º, (e) 4.76 mm, 90º and 30º, and (f) 3.18 mm, 90º and 30º.

Figure 5. Comparison of impact flash light curves for 60º, 6.35 mm-Pyrex/pumice powder impacts at "high" (4.94 km/s) and "low" (1.72 km/s) velocities from 0 – 800 μs (a) and 0 – 250 μs (b). The initial kinetic energy of the projectile is 8.2 times higher for the high-velocity impact, producing higher radiating source temperatures. The heated sources produced by the low-velocity impact do not emit much light in the visible wavelength range and the source cools very quickly to temperatures too low to be self-luminous. The result is a dimmer, shorter duration impact flash signal for the low-velocity impact. An early-time spike, delayed intensity peak, and decay signal are all observed for the low-velocity impact; however, the maximum intensity corresponds to the spike.

Figure 6. (a) Effect of impact angle on the observed light curves for 6.35 mm Pyrex/pumice powder impacts between 5.5 and 5.7 km/s. Higher angle impacts exhibit lower and broader intensity peaks and longer rise times to the maximum intensity. The brightest maximum intensity occurs at 30º. At 15º the projectile is poorly coupled to the target on impact, producing a very different light curve. Here, the ricochet impacts the

downrange chamber wall ~200 μs after impact (later times are truncated). (b) A logarithmic scale highlights the decay portion of the curve. After the broad intensity peak, the decay follows a power law. For 90º to 45º angles, the decay rate is the same. For 30º and 15º angles, the post-peak decay rate is slower.

Figure 7. Light curve comparison for 30º impacts into various target types: pumice powder (5.83 km/s), perlite granules (5.51 km/s), and a pumice block (5.80 km/s). The addition of porosity (perlite versus pumice powder) or strength (pumice block versus powder) to compositionally similar targets leads to a drastic suppression in the observed luminous output of the impact flash, both in terms of overall signal brightness and duration.

Figure 8. Comparison of top and side view intensity curves for impact angles of (a) 90º, (b) 45, and (c) 30º for Pyrex/pumice powder impacts at 5.15, 5.33, and 5.37 km/s, respectively. In all cases, the highest (black) curve represents the top view data, the lowest (red) curve represents the side view data, and the intermediate (blue) curve represents the difference between the two. The large difference observed between the top and side views demonstrates that most of the radiating source material is contained inside of the transient crater, especially for vertical impacts.

Figure 9. Plot of the 6.35 mm, 30º peak intensity as a function of velocity (from Figure 4) for a range of ambient pressures. Open circles: typical pressures used in the current study (0.30 – 0.92 Torr). Closed circles: high pressures (3.0 – 3.6 Torr). Closed triangle: low pressure (0.39 Torr of helium, which results in an atmospheric density equivalent to air at 0.03 Torr). No pressure dependence is observed.

Figure 10. Plot of the rise time to the maximum intensity versus sinθ. A correlation holds for all angles (90º to 15º). The relationship between the rise time and sinθ may relate to the distribution of the melt volume and the depth at which the projectile couples its energy to the target. A shallower depth occurs at lower impact angles and leads to faster exposure of heated material to the detector, i.e., a shorter rise time.

Figure 11. The intensity evolution versus τ for the same impacts plotted in Figure 6. The use of τ causes the maximum intensities for all angles to coincide at $\tau \sim 35$ (shown by the dashed line). The increase in maximum intensity with decreasing impact angle (90º to 30º) can also be observed here. The increase appears to relate to cosθ for angles from 75º to 30º. Such a dependence could correspond to an increase in the exposed area of the heated material or the contribution of frictional shear heating and ricochet.

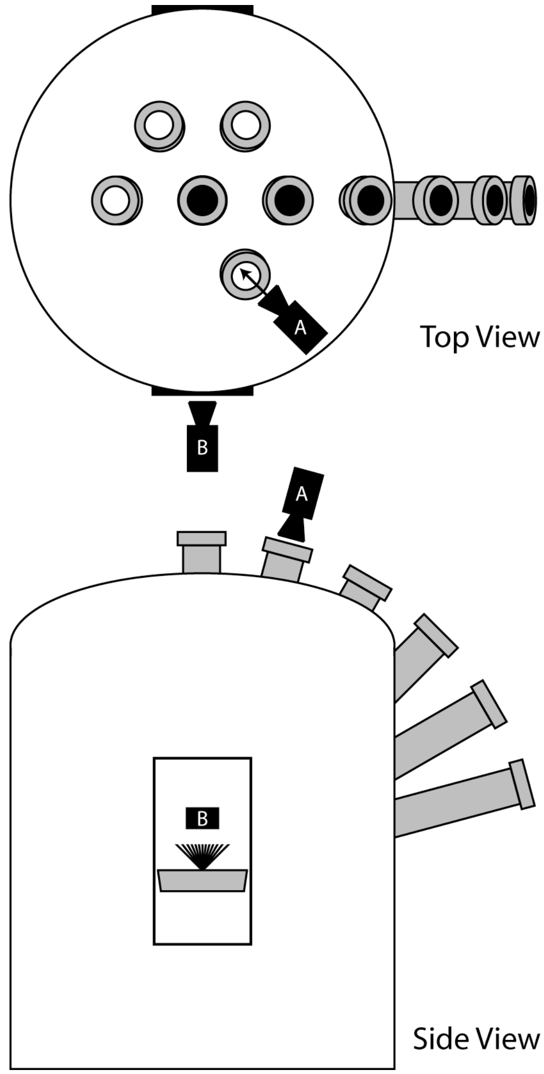

Chapter 1, Figure 1

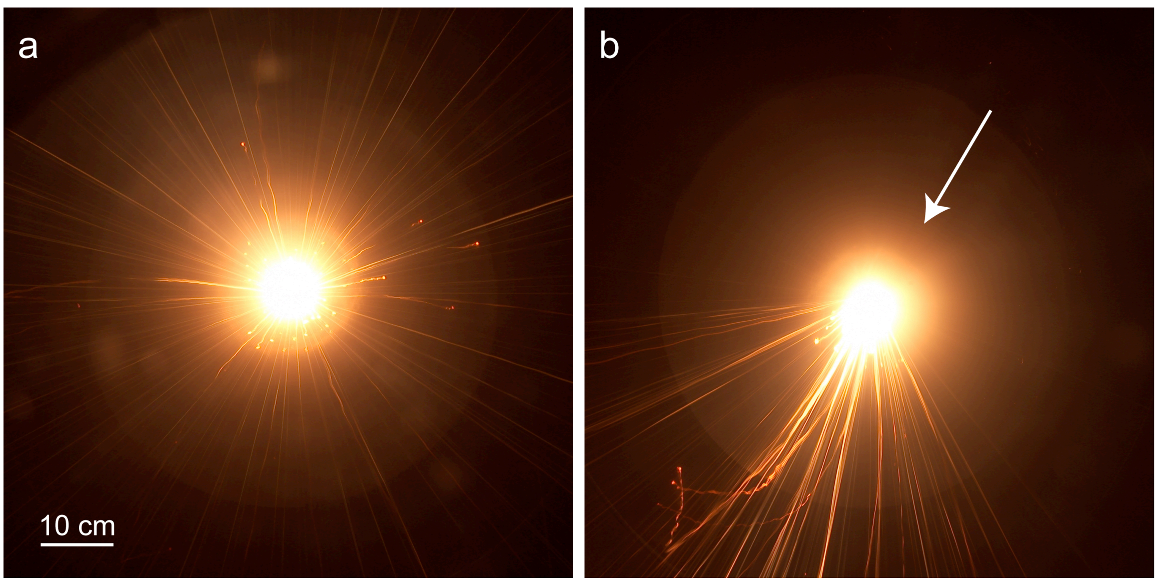

Chapter 1, Figure 2

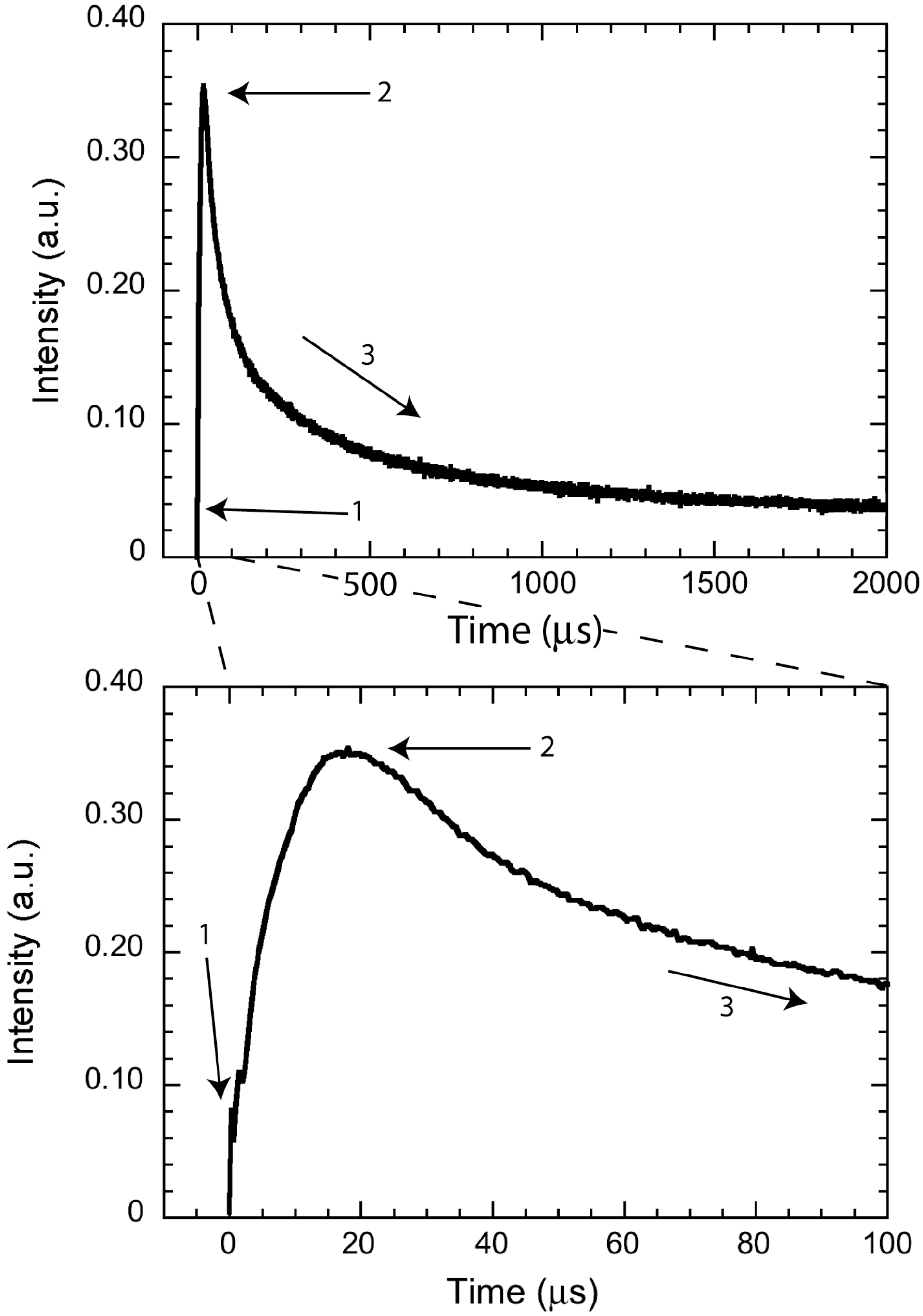

Chapter 1, Figure 3

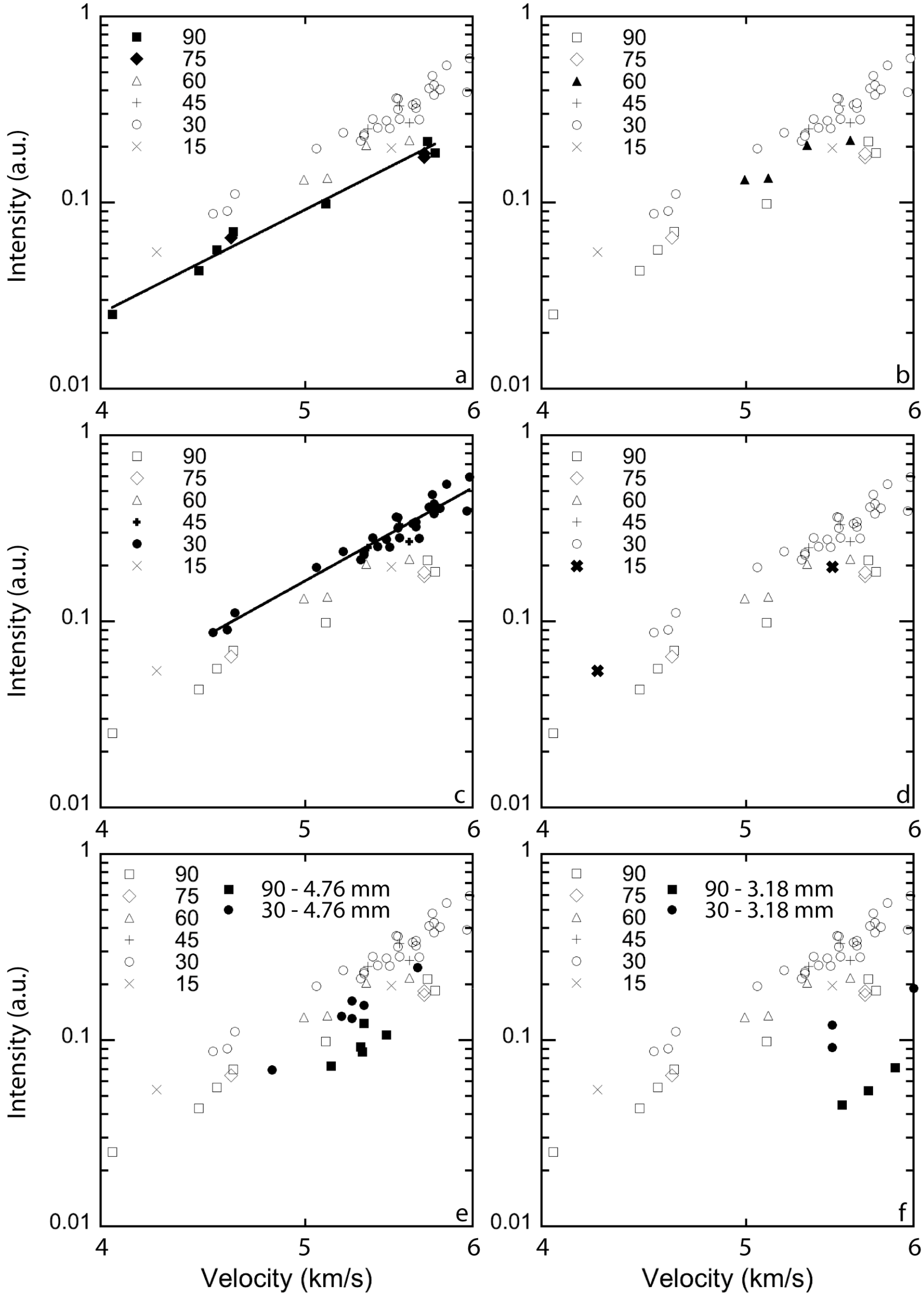

Chapter 1, Figure 4

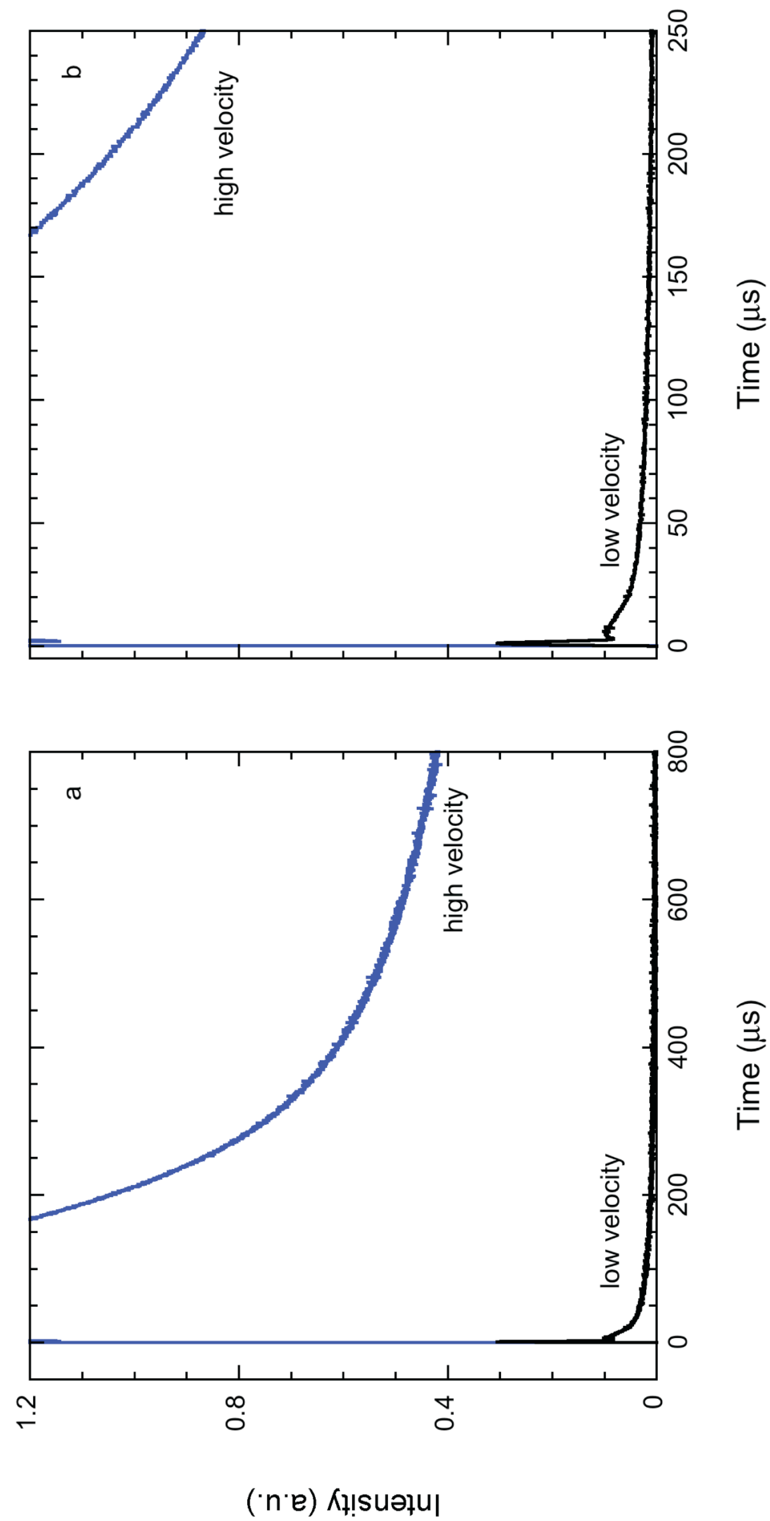

Chapter 1, Figure 5

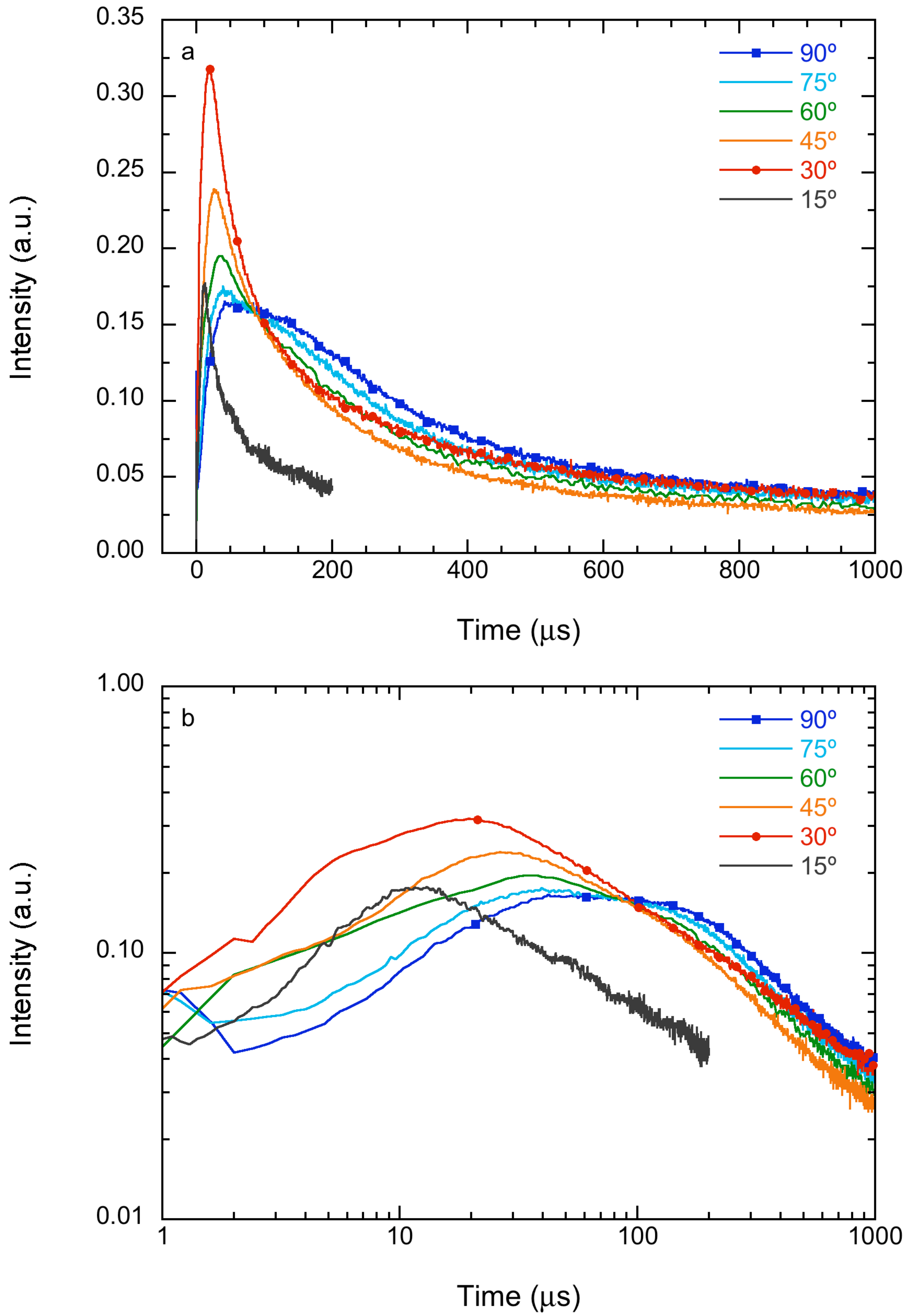

Chapter 1, Figure 6

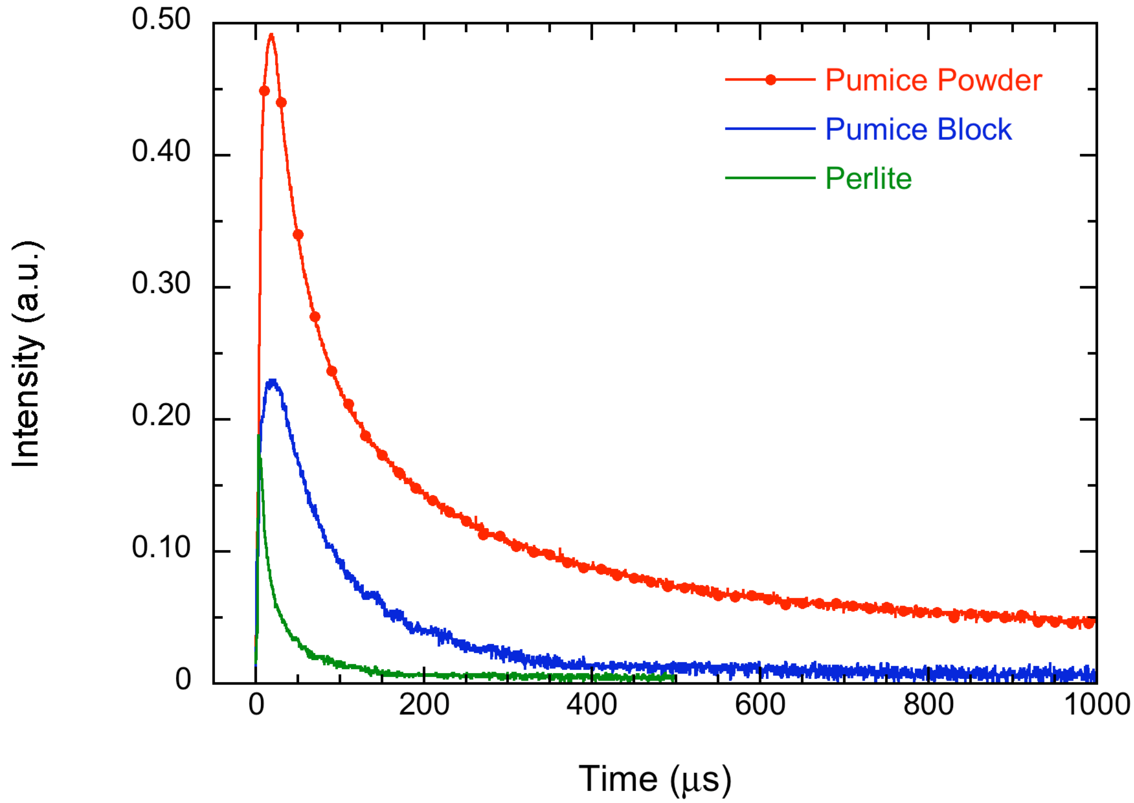

Chapter 1, Figure 7

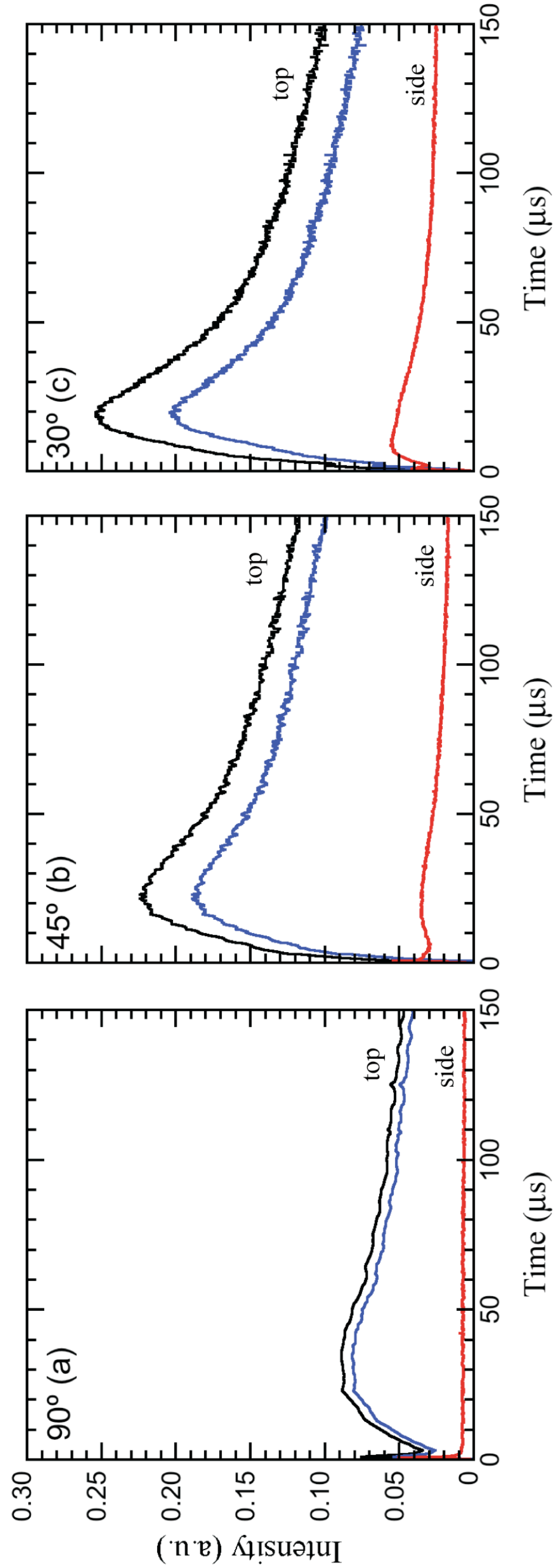

Chapter 1, Figure 8

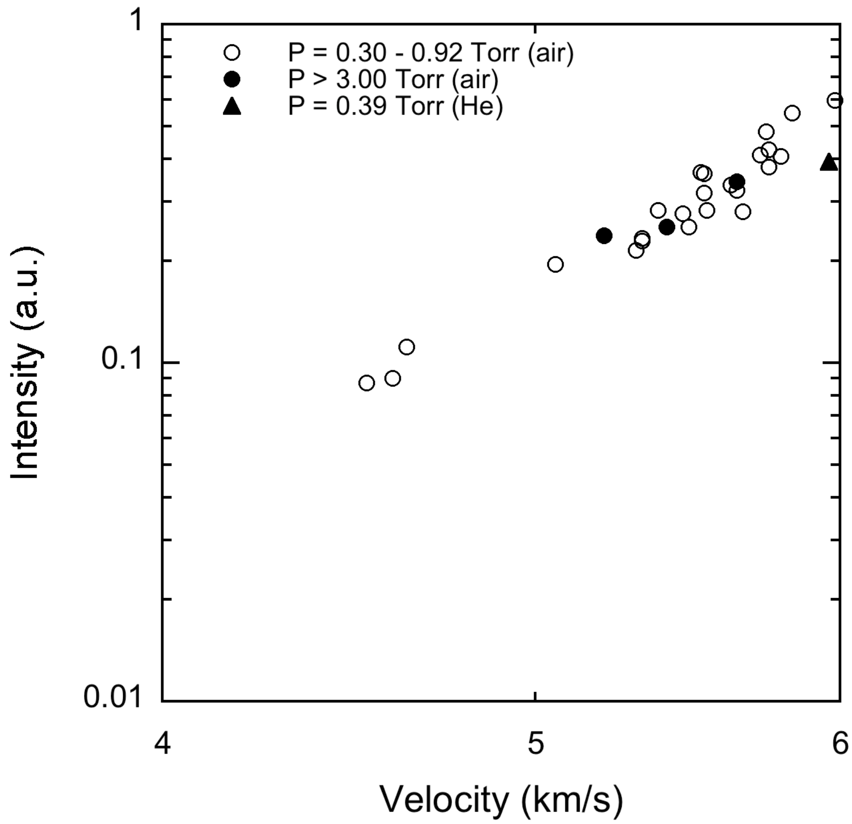

Chapter 1, Figure 9

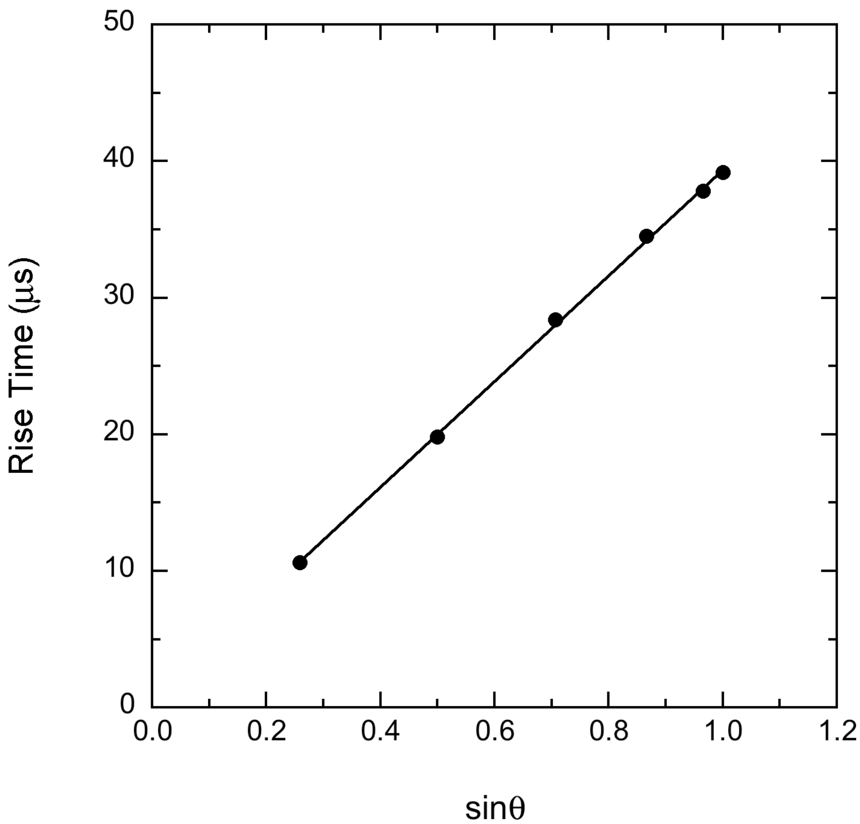

Chapter 1, Figure 10

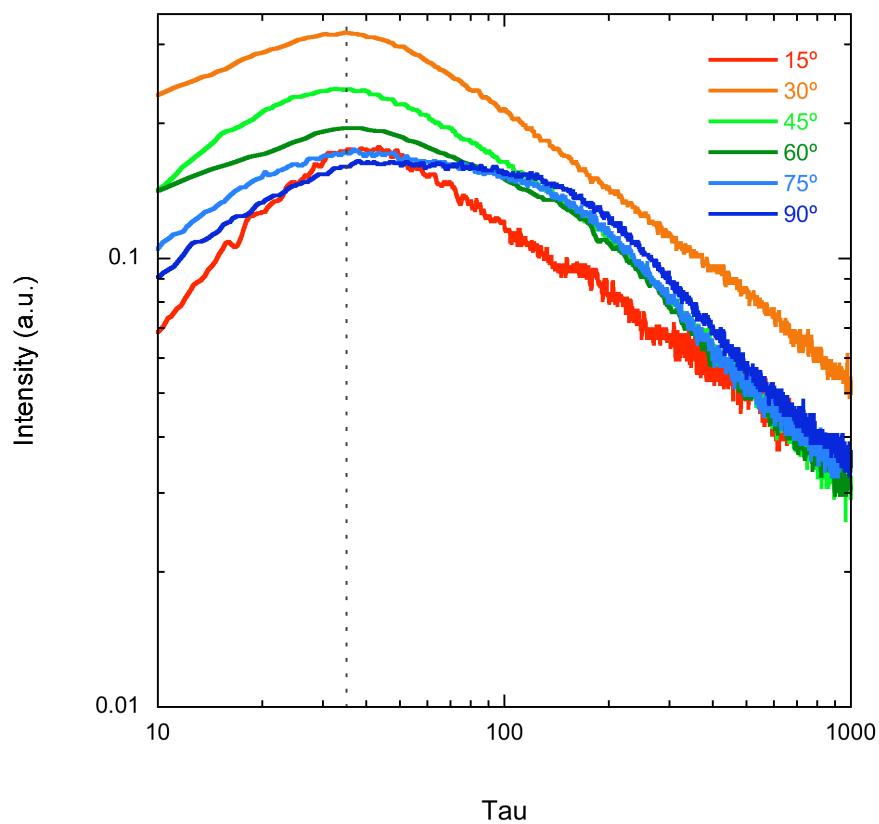

Chapter 1, Figure 11

Chapter 2

Thermal Evolution of the Impact Flash

Carolyn M. Ernst

Peter H. Schultz

Department of Geological Sciences

Box 1846

Brown University

Providence, RI 02912

Abstract

The impact flash provides a method of observing small-scale cratering processes at very early times. Evolution of the flash can be used to evaluate the effect of initial impact conditions. The thermal evolution of the impact flash also contains information about early-time cratering processes. Experimental impacts of Pyrex spheres into non-volatile, particulate pumice targets were performed at the NASA Ames Vertical Gun Range. A multi-filtered photodiode system recorded the flash intensity through time, thereby allowing observations of the thermal evolution. The maximum temperature occurs at the moment of first contact. The temperature subsequently decreases, with a decay rate affected by initial conditions. Intensity and temperature constrain the source area evolution of the flash as well as its luminous efficiency, which is found to be in the range of 10^{-4} – 10^{-5} under the examined conditions. The long-duration "tail" of the intensity signal contains a significant portion of the total radiated energy, with as much as 60% of the visible-wavelength luminous energy being emitted after the intensity peak.

1. Introduction

An impact flash is the observable light produced by an impact event. Possible sources include atomic and molecular emissions from vaporized materials and thermal emissions from heated melt, particulates, and vapor condensates. The flash begins at first contact between the projectile and the target, and its characteristics (evolution, duration, and magnitude) vary widely depending on initial impact conditions.

Most early studies of the impact flash involved impacts into metal targets, which produced flashes of very short duration (< 10 μs) [*MacCormack*, 1963; *Jean and Rollins*, 1970; *Eichhorn*, 1976]. The principal light sources from such impacts are heated microparticles as well as atomic and molecular emissions from the produced vapor. Impacts into sand targets also produced brief flashes due to the low impact velocities ~2.5 km/s [*Gehring and Warnica*, 1963]. In all cases, the maximum intensity of the flash occurs during the initial projectile penetration, with the signal quickly decaying thereafter. Later theoretical investigations also predicted short-duration impact flashes [*Melosh et al.*, 1993; *Artem'eva et al.*, 2001]. These theoretical estimates predicted durations on the order of milliseconds, even though the studies assumed much higher velocities (50 - 70 km/s). Observations and predictions of such short signals led to the expectation that impact flashes would be of extremely short-duration.

Recent studies explored the flash intensity evolution during impacts into non-volatile, particulate targets (mainly pumice powder) [*Ernst and Schultz*, 2002; 2003]. Although the sizes and speeds are comparable to previous studies, the flash characteristics are noticeably different. Impacts into particulates produce thermal signals lasting orders of magnitude longer than metallic-target flashes observed in previous studies. The target grains and projectile materials heated and melted by the impact continue to radiate while cooling. The resulting intensity light curve lasts well beyond the projectile penetration time, with the signal remaining detectable out to 2 ms (measurement duration). Shockwaves heat porous materials to higher temperatures than non-porous materials. Energy in the porous impact is irreversibly partitioned into heat due to an increase in entropy as pore space is compacted [*Love et al.*, 1993]. Friction at grain boundaries could also be an additional heat source [*Schultz*, 1996; *Schultz et al.*, 2006].

In Chapter 1, intensity measurements were made using a spatially integrating photodiode. Typical impact flash light curves exhibit three main features: (1) an early-time spike, (2) a broad intensity peak, and (3) a long decay signal (Figure 1). The spike is due to the first contact between the projectile and the target with a duration on the order of the time it takes the projectile to travel its own diameter into the target. The broad intensity peak is delayed from first contact. The magnitude and duration of this peak are highly dependent on initial impact conditions. The decay signal is very long lasting for pumice powder targets, depending on the cooling rate of heated particulates, both ejected from and retained in the transient crater.

Flash evolution depends on several initial conditions: velocity, impact angle, projectile diameter, target type, and view orientation. As a result, observations of the impact flash can be used to constrain initial conditions, even if observed from great distances. More information can be gathered from the impact flash by examining its thermal evolution.

For a purely kinetic event (with thermal emissions from a blackbody source), the impact flash intensity (I) is given by:

$$I = \sigma T^4 A_s, \tag{1}$$

where T is the temperature, A_s is the effective source area, and σ is the Stephan-Boltzmann constant. Spatially integrated intensity measurements cannot resolve the source of the intensity evolution, i.e., changes in source temperature, area, or a combination of the two. Following Equation 1, an intensity rise could be caused by a radiating source of constant size and increasing temperature, but a growing source area at a constant temperature could create the same signal. The ambiguity of the intensity data alone limits the information that can be obtained about the early-time processes controlling the impact flash generation.

The main purpose of the present study is to further understand the underlying processes responsible for the impact flash based on the work done in Chapter 1. First, a multi-filtered photodiode system simultaneously records the impact flash intensity, which allows the calculation of the flash temperature. The thermal evolution characteristics are analyzed and related to changing initial projectile conditions (velocity and angle). Next, the intensity and temperature measurements are used together to derive the source area and its evolution through time. Last, we calculate the luminous efficiency of the impact flash under the same variable conditions. The findings are used to interpret the physical processes generating the observed impact flash and controlling its exposure, in addition to deriving correlations between the initial impact conditions and the flash temperature.

2. Experimental Design

In order to observe the thermal evolution of the impact flash, a series of hypervelocity impact experiments were performed at the NASA Ames Vertical Gun Range (AVGR). The two-stage light gas gun is capable of impact velocities up to ~6.5 km/s for projectiles ≤ 6.35 mm in diameter. The impact angle can be varied from 90º to 15º (measured from the horizontal) in 15º increments, allowing for oblique impacts. The variable launch angles of the AVGR allow the use of loose particulate targets. The target chamber is approximately 2.5 meters in diameter and height, which is large enough to permit the free expansion of the ejecta without interference from the chamber walls that could otherwise affect later-time observations of the photometric signal.

In this study, Pyrex projectiles (3.18 to 6.35 mm in diameter) impacted mainly pumice powder targets (1.25 g/cm^3 bulk density, with a bimodal grain size distribution at 25 μm and 81 μm). Impact velocities ranged from 4.25 to 6.04 km/s, and angles ranged from 90º to 15º. The chamber pressure was reduced to near-vacuum conditions (< 0.6 Torr).

Two photodiode systems, located above the target chamber, to either side and slightly uprange of the oblique impact trajectory, recorded the light output every 100 ns for a total of 2 ms. The first system, previously described in Chapter 1, is a single photodiode with a spectral range of 350 – 1100 nm. The second system consists of six identical photodiodes used in conjunction with narrow bandpass filters (50 – 80 nm FWHM). The filters used in this study have wavelength centers at 500, 550, 600, 650, 700, and 880 nm. The multiple-channel photodiode/filter system was calibrated using a

Thermogauge carbon arc blackbody source at NASA Ames Research Center's Sensor Calibration Laboratory.

The field of view of each photodiode was large enough to ensure that all radiating sources would remain observable over the recorded time interval. A high-speed video camera (500 frames/sec) also recorded the impacts in order to confirm that the experiments occurred nominally (i.e., the projectiles did not disrupt before impact). The predominantly silicate compositions of Pyrex and pumice minimize the production of atomic and molecular emissions in the visible wavelength range and enhance the generation of thermal emissions, which are of primary interest for this study.

3. Thermal Evolution

The six filtered channels exhibit the same features (early-time spike, delayed intensity peak, long-duration decay signal) as the unfiltered light curve, as shown in Figure 2. Note that these are raw, uncalibrated data. Consequently, the filtered-channel intensities do not exhibit the relative values expected from a thermal source; however the important comparisons here are the timings of similar intensity features. The consistent characteristics of the filtered curves confirm the expectation that impacts of Pyrex projectiles into pumice powder targets (hereafter, Pyrex/pumice powder impacts) do not produce strong emission bands; therefore, we can assume a completely thermal source and calculate the source temperature from the wavelength-filtered data.

The output of each photodiode is proportional to the light energy received. The non-uniform wavelength response of the detector and the spectral transmission of the filters and the target chamber windows affect the observed signals. The instrument was calibrated with filters and windows in place in order to eliminate their possible effects on the calculated temperatures (see Appendix). Because the photodiodes record the spatially integrated light output, the calculated temperature values are spatially integrated over the entire flash at a given time. The actual temperature of the source, however, is presumably non-uniform.

3.1 Temperature Calculation

The radiated power per unit area per unit wavelength from a blackbody depends only on its temperature (*T*), as given by Planck's Law:

$$\frac{dR}{d\lambda} = \frac{2hc^2}{\lambda^5}\frac{1}{e^{hc/\lambda kT} - 1}, \tag{2}$$

where λ is wavelength, h Planck's constant, c the speed of light, and k Boltzmann's constant. The color temperature of a thermal radiation source can be determined using intensity ratios at different wavelengths. The color temperature of a source is the temperature at which a blackbody, emissivity (ε) = 1, would emit radiation corresponding to the observed intensity ratios. If $\varepsilon < 1$ but wavelength-independent (definition of a "greybody"), the color temperature of the source as determined by ratios is equivalent to its true temperature. For this study, all materials are assumed to be blackbodies, but the ratio method of temperature calculation used here is not affected by a blackbody versus a greybody assumption (see Appendix).

The multi-channel photodiode system functions as a pyrometer with a spectral range favorable for high temperature measurements and a temporal response appropriate for observing the quickly evolving flash. The signals recorded by the filtered channels are ratioed and combined with the instrument calibrations to determine the color temperature of the impact flash at a given time. Applying this method to an entire intensity light curve generates the temperature as a function of time. It is difficult to obtain temperature measurements for the exact moment of impact since the oscilloscope sampling rate does not always capture the very earliest portion of the signal; however, the recorded data begin no later than 100 ns after first light.

3.2 Temperature Characteristics

Temperatures were calculated out to ~200 μs after impact. Figure 3 illustrates the impact-flash temperature evolution along with the corresponding unfiltered intensity curve for a 30º impact at 5.33 km/s. The temperature data were smoothed using a Stineman function (geometric weight applied to the current point and ± 10% of the data range) in order to reduce scatter. The error in these temperature measurements is ± 200 K. The arrow indicates the point on the temperature curve corresponding to the maximum intensity. The maximum intensity does not coincide with any major features on the temperature curve and clearly does not coincide with the maximum temperature (T_{max}).

All of the Pyrex/pumice powder impacts exhibit the same basic thermal evolution (out to 200 μs) as that shown in Figure 3: the maximum temperature occurs at the beginning of the signal followed by a gradual decay over the time observed. As will be shown below, details of the temperature evolution, including the T_{max} and decay rate, are affected by changes in initial conditions.

The first 2 μs of the temperature signal are difficult to interpret. This portion of the signal coincides with the early-time intensity spike. For some impacts, this early signal is continuous with the trend of subsequent temperature measurements, but in other cases it exhibits sharp jumps from higher temperatures (> 5000 K, in one case as high as 6500 K) occurring at $t = 0$. Due to this break from the rest of the signal, it is initially unclear whether these early temperature values are real (i.e., related to extreme temperature and pressure conditions at the projectile/target interface) or related to insufficient time resolution.

At contact, the target and projectile materials are heated to high initial temperatures (T_i) due to compression by shockwaves. The shock release time is proportional to the travel time of the shockwave to the nearest free surface, which in this case is the rear of the projectile [*Baird and King*, 1999]. The shock release time is on the order of 1 μs for the velocities and diameters used in this study. The reversible part of the shock compression process causes the temperature of the shocked material to suddenly decrease once the shocks are released (~1 μs), after which the observed temperature can be considered a "release" temperature (T_o). The release temperature continues to decrease as the heated source expands [*Ang*, 1990].

The irregular temperature evolution during the first couple of microseconds corresponds to the time before the shock release; consequently, the break in trend likely represents a real process. It is possible that at these early times the shocked projectile material is being observed due to the transparency of the projectile. The data are collected on two separate oscilloscopes and although triggered off of the same source, they occasionally have staggered recording times. It is possible this may affect the very early-time measurements when the intensity changes on a timescale at or shorter than the data resolution. Added complications arise because the high temperatures (5000 – 6000

K) are well above the calibration performed on the system (3100 K); however, such high temperatures have been derived from emission lines for quartz/dolomite impacts at similar velocities [*Sugita et al.*, 1998]. Because temperature measurements at such early times are less certain, the displayed temperatures begin 2 μs after impact. The maximum temperatures reported here therefore correspond with the initial release temperatures ($T_{max} = T_o$) measured at 2 μs, not to the true temperature maximum that occurs on impact (T_i).

The velocities used in this study are limited mostly to a range of 5.20 to 6.04 km/s. Lower velocities (< 4 km/s) do not generate sufficient visible light to be detectable by the filtered photodiode channels. Higher speeds (~7 km/s), although attainable, induce too much wear on the launch barrel of the AVGR. Coupled with a small variation in projectile diameter, the initial condition limitations result in a small range of possible specific kinetic energies, spanning less than an order of magnitude (790 – 4550 J). As a result, the T_{max} values lie in a narrow range, from 3400 - 4500 K (Table 1). Note that the melting and vaporization temperatures of pumice are ~1700 K and ~3800 K respectively [*Cintala*, 1992]. Some T_{max} values are high enough to exceed the vaporization temperature. These temperatures are confined to a very small area, likely along the projectile/target interface. Any vapor produced will be small in quantity. All the T_{max} values are well above the melting temperature, consistent with a thermal source primarily composed of melt droplets.

4. Discussion

4.1 Temperature

There is an observable dependence of T_{max} on impact angle (Figure 4): under otherwise identical impact conditions, lower angles result in higher T_{max} values. This contrasts with previous studies of vapor plumes concluding that the temperature decreases with decreasing angle [*Schultz*, 1996; *Sugita et al.*, 1998]. Theoretical analyses have also come to similar conclusions [*Pierazzo and Melosh*, 2000a; *Nemtchinov et al.*, 1999], and peak shock pressures are known to decrease for decreasing angle (both experimentally and theoretically) [*Schultz*, 1996; *Dahl and Schultz*, 2001; *Pierazzo and Melosh*, 2000a].

The disagreement with previous experimental results may be due to a difference in the emitting sources (vapor phases versus thermal emissions). The inconsistency with theoretical studies may reflect simplified inputs for the codes used to simulate oblique impacts. For example, these hydrocode simulations did not include a strength model, making it impossible to address frictional effects [*Pierazzo and Melosh*, 2000b].

Frictional shear heating occurs along the projectile/target interface, localized near the surface. Its effect increases in magnitude with obliquity [*Schultz*, 1996; *Schultz et al.*, 2006]. This effect was found to enhance vapor production in oblique impacts. If shear heating contributes significantly to target melting along the surface, it would create a hot, well-exposed thermal source. Visibility of the heated material also may contribute to the observed inconsistency. Vertical impacts may result in the hottest portion of the source buried in the transient crater and concentrated in a small area. Oblique impacts result in a melt mass that is spread out and partly ejected downrange, thereby exposing these sources to the detectors. Finally, it is possible that this "reverse" trend only applies to the initial temperature, whereas the previous studies apply more to later.

A higher impact velocity generally results in a higher T_{max} (see Figure 4), as would be expected due to an increased specific kinetic energy. *Baird et al.* [1997] showed that the T_i behind the shockwave varies quadratically with velocity (assuming a constant specific heat):

$$T_i = \frac{v^2}{24Nk}, \qquad (3)$$

where N is the number of atoms per unit mass and k is Boltzmann's constant. This equation includes the assumption that the target and projectile have the same composition. The predicted values of T_i are also displayed in Figure 4, assuming a vertical (90º) impact and taking $N = 1.00 \times 10^{25}$ kg^{-1} (the value for SiO_2). As expected, these T_i values are all higher than the T_{max} observed by the photodiodes at 2 μs for the 90º impacts. Because lower angles produce higher temperatures, not all of the non-vertical T_{max} values fall below the predicted 90º T_i values. Though a relation between T_{max} and velocity is unclear, the data at a given impact angle do not follow a similar quadratic trend to T_i. The theoretical quadratic relation (Equation 3), however, may not apply to the release temperature. Alternatively, the temperature may be affected by the contrasting projectile/target compositions. Additionally, because some temperatures are above the limit for vaporization, some heat is lost during phase transitions.

Although ambiguous at the beginning of the signal, a stronger correlation between temperature and velocity begins to emerge at later times, after the intensity peak. Similar relationships are observed for temperatures observed at both 100 and 200 μs (T_{100} and T_{200}, respectively) (Figure 5a, Table 1): an increase in impact velocity leads to an increase in T_{100} and T_{200}. Significant scatter is still observed over the available range of speeds for a given projectile size and composition; therefore, it is difficult to quantify the correlation. Nevertheless, the data still do not follow theoretical expectations (Equation 3). Interestingly, at these later times, the temperature of a vertical impact is higher than that of an equivalent oblique impact. This reversal may be due to the more efficient cooling at oblique angles due to the distribution of the radiating source.

The measured temperatures at a given time occur at different portions of the intensity curve for different impact angles. For a 90º impact, t = 200 μs lies on the peak of the intensity curve, whereas for a 30º impact, t = 200 μs lies well into the decay portion of the curve. Therefore, the temperatures for oblique impacts are being sampled during different stages of the impact process where different processes are governing the observed intensity and temperature.

Impact-flash timescale can be normalized to a penetration depth timescale (the time it takes the projectile to a depth equal to its diameter into the target):

$$\tau = t \cdot \left(\frac{v \sin\theta}{a} \right), \quad (4)$$

where t is time, v is the impact velocity, θ is the impact angle, and a is the projectile diameter. Note that the τ defined here is based on a different normalization factor than that used in Chapter 1. The use of τ values allows the comparison of impacts at different angles for a specific set of observations or processes. By using τ instead of time, the chosen temperatures better represent similar stages in the impact event. A value of τ = 250 lies near the intensity peak but on the decay portion of the temperature curve while also remaining within the maximum time observed for all of the impacts. The τ values range from 135 - 225 for the 90º impacts and place the selected temperatures off the intensity peak. For the 30º impacts, the τ values ranged from 65 – 144 and place the selected temperatures closer to the intensity peak than T_{200}. The use of τ also effectively relates the temperature at a given time to the vertical component of velocity ($v\sin\theta$).

The T_τ values exhibit a clear correlation with impact velocity, regardless of impact angle or projectile diameter (Figure 5b). The theoretical quadratic relation, however, does not fit the observed T_τ. Instead, a power law can fit the trend with an exponent from 0.5 to 1.0. Additional experiments at higher (6 – 7 km/s) and lower (4 – 5 km/s) velocities may help to refine the value of this exponent. Because the temperatures calculated at any post-intensity peak time do not appear to relate to a v^2 term, the cooling and dispersal of the thermal source is not simply related to the initial kinetic energy of the projectile. A similar power-law relationship (with an exponent of 0.3) was observed between the vapor temperature and the vertical component of impact velocity [*Sugita et al.*, 1998]; however, these temperatures were observed at early times (0 – 20 μs).

The total luminous energy (*LE*) of an impact can be calculated by integrating the intensity (Equation 1) over time [*Schultz et al.*, 2005]:

$$\begin{aligned} LE &= \sigma \int_0^t T^4(t) A_s(t) dt \\ &= \sigma T^4 A_s \Delta t \end{aligned} \tag{5}$$

if averaged over the time. The luminous energy is assumed to be a constant fraction (c_1) of the initial kinetic energy (KE_o):

$$LE = c_1 \cdot KE_o = c_1 \cdot \frac{1}{2} m v^2. \tag{6}$$

Temperature can therefore be related to impact velocity with a different constant (c_2) by combining Equations 5 and 6:

$$T^4 A_s \Delta t = c_2 v^2. \tag{7}$$

At later times (after the intensity peak), the source area can be assumed to be constant with time. Equation 7 becomes:

$$T^4 \Delta t \sim v^2. \tag{8}$$

Solving for temperature leads to the following dependence:

$$T \sim \frac{v^{0.5}}{\Delta t^{0.25}}. \tag{9}$$

Substituting τ for Δt from Equation 4, for a 90º impact:

$$T_\tau \sim v^{0.75}. \tag{10}$$

Both Equation 9 and 10 are consistent with the observed relationship (Figure 5) within the error limits.

4.2 Temperature Decay

The temperature and intensity evolution for impacts at 90º, 45º, and 30º are shown out to 200 μs in Figure 6 and the first 20 μs are shown in Figure 7. As discussed in Chapter 1, the decay portion of the intensity curve follows a power law that begins after the broad intensity peak. The temperature decay for different impact angles follows a simple power law:

$$T(t) = T_o t^{-\beta}. \tag{11}$$

The observed decay can be approximated by a single power-law model with β values ranging from 0.04 to 0.15 (see Table 1). Overall, the temperature decays faster for lower impact angles (larger β). At early times (before the maximum intensity) the temperature deviates from the power law systematically with angle (see Figure 7). The deviation is best illustrated on a logarithmic scale (Figure 8): (a) for 90º, the observed temperatures deviate below the fitted power law; (b) for 45º, the observed temperatures lie along the power law; (c) for 30º, the observed temperatures deviate above the fitted power law. Although not shown here, (different projectile velocity and diameters) the temperature decay for 60º and 90º resemble each other; the decay for 15º and 30º also resemble each other. The observed departure from a single power law represents a transition in cooling rates very early in the cratering process. This transition occurs earlier during oblique impacts.

The temperature evolution is thus best approximated by a combination of two power laws with the break occurring near the time of the intensity maximum (t_{Imax}):

$$\begin{aligned} T(t) &\sim t^{-\beta_{20}} \qquad t < t_{I_{\max}} \\ T(t) &\sim t^{-\beta_{200}} \qquad t_{I_{\max}} < t \end{aligned} \tag{12}$$

There are three main processes represented in the temperature curve. First, during the initial 1-2 μs, the observed high temperature is governed by the shock heating. Second, between this time and the time of the intensity peak (2 – 20 μs), the initial decay is highly dependent on the impact angle, exhibiting a faster cooling rate for oblique impacts and a slower cooling rate for vertical impacts. This angular dependence relates to the evolving source area. The temperatures at this time for the observed impacts is close to the vaporization temperature (T_{vap} = 3800 K). It is possible that phase transitions could contribute to the evolving temperature decay. Third, from the time of the intensity peak through the end of the observations (~20 – 200 μs), the temperature decay is well fit by a new power law. This portion of the temperature evolution represents cooling that is not much affected by source expansion. The behavior of the temperature maximum and evolution (β) described above are specific to the examined impact conditions.

The decay differences due to angle can be explained in terms of the distribution of the radiating source. For 90º impacts, the source is largely contained in the transient crater. For 30º impacts, the transient crater opening is larger and shallower, and radiating material is more spread out, located closer to the surface, and partly ejected downrange. The hottest radiating sources are exposed to the detector very early, and the broader dispersal leads to faster cooling.

4.3 Comparisons to Previous Experiments

Kadono and Fujiwara [1996] made temperature measurements during impact experiments using nylon projectiles and targets. Temperature was measured to a maximum time of 20 μs after impact, thus limited by ejecta impacting the chamber walls and producing a new intensity source that overtook the original signal. Power law functions were fit to five flash temperature evolutions with β_{KF} values ranging from 0.04 – 0.20. These values match well with the β_{20} values (0.03 – 0.08).

The power-law fits improve significantly if the first 1 - 2 μs are omitted from the fit. For example, R^2 = 0.67 for the published power law fit to their data (impact #321), whereas R^2 = 0.97 if the first temperature observation (taken at 1 μs after impact) is omitted. The β_{new} values for all but one of the omitted-point cases change significantly, with most of the new values ranging from 0.24 – 0.29. The value of β that remained close to its published value (β_{new} = 0.06 versus β_{KF} = 0.04) and within the range of β_{20}

values was that of impact #322 (5.63 km/s, 55º). Note that this impact was also the only experiment viewed from above, matching the view orientation of the present study.

Exponential functions also fit the *Kadono and Fujiwara* [1996] data with R^2 values comparable to the power law fits, thereby making the fits indistinguishable based on the available data. This is an interesting observation, since the same is true for the 0-20 μs data from the present study.

As discussed in the previous section, the β_{20} function only describes the temperature evolution at early times and cannot be used to assess the temperature decay; a second power law function must be made to match this portion of the curve (Equation 6). The trend observed for the first 20 μs is thus not representative of the long-scale cooling behavior. Therefore, if Kadono and Fujiwara could have observed their impacts for longer times, the later temperature evolution likely would not follow the observed 0 - 20 μs decay pattern.

4.4 Theoretical Analysis

A complete forward model of the thermal evolution requires appropriate equations of state for both the projectile and target materials, the location and expansion of the thermal source (which will change through time), the opacity of the source (which also may change with time), and the non-uniformity of the source temperature, among other factors. In order to find an analytical solution for the thermal evolution, however, simplifying assumptions can be made. Impact conditions are assumed to be in thermal equilibrium after the initial shock heating occurs. Also, the radiating source is taken to be a solid sphere (optically thick) of constant size (no source growth). Assuming that heat conduction is rapid on the timescale of the radiative losses at the blackbody surface of a cooling sphere,

$$mC_v \frac{dT}{dt} = -\sigma A T^4, \tag{13}$$

where m is the mass, C_v is the specific heat, and A is the surface area of the assumed sphere. Integrating Equation 13 yields the temperature with time:

$$T(T_o,t) = T_o\left(1 + \frac{9\sigma T_o^3 t}{R\rho C_v}\right)^{-1/3}, \tag{14}$$

where T_o is the immediate post-shock release temperature, assumed to be initially uniform [*Baird and King*, 1999]. The time evolution of the temperature is calculated using Equation 16, assuming values of $\rho = 2.2$ g/cm^3 (particle density of pumice) and C_v= 0.84 J/gK (specific heat of sand). The free parameters in the model are T_o and R.

The dashed lines in Figure 9 represent the models that best followed the observed temperature evolution over the time observed for the previously discussed 90º, 45º, and 30º impact angles. The value of T_o is about 3500 K for all three cases. In order to make the model fit the majority of the observations (30 – 200 μs), the value of R corresponds to micron-sized particles (R = 3 - 5 μm). This size is significantly smaller than the individual grain size of the pumice powder (R = 12.5 μm), but characterizes shock-comminuted fines. The overall radial extent of the flash source, however, is observed to be much larger, on the order of mm to cm [*Ernst and Schultz*, 2004]. When R was fixed to values in this range, the temperature values decayed almost imperceptibly over the observed 200 μs.

As should be expected, the early portion of the 45º and 30º signals could only be matched when the data from 0 - 30 μs were considered separately. Under these conditions, the best-fit R values were smaller (necessary to match the much faster decay rates). Small source particles ($R < 0.5 – 2$ μm in diameter) best fit the model. Using this method, the model curves could not match both the initial temperature decrease (0 – 50 μs for the 45º and 30º impacts, 0 – 10 μs for the shallower 90º profile) and the later observations (30 – 200 μs) with the same set of parameters. Consequently, the model contains too many simplifying assumptions to recreate the entire temperature evolution, i.e., R is not a constant.

Use of Equation 14 implicitly assumes that heat conduction is rapid on the timescale of radiative losses (assumes the bulk temperature is roughly equal to the surface temperature). In reality, heat conduction also should play a role. Because the surface of a sphere cools faster than the interior, the rate of heat transfer from the center will limit the rate of radiative loss from the surface, i.e., the sphere will take longer to cool.

The conductive cooling time of a sphere (t_c), i.e., the time it takes for a given temperature to propagate to the center of a sphere, can be estimated by:

$$t_c = \frac{R^2}{\kappa}, \tag{15}$$

where κ is the thermal diffusivity. For typical rocks, $\kappa = 10^{-6}$ m^2/s. For a particle size equivalent to the smaller mode of the pumice powder ($R = 12.5$ μm), $t_c \sim 160$ μs. This time is towards the end of the temperatures observed in this study; consequently, the conductive cooling time is longer than the radiative loss time. Larger particles are also affected by skin depth, where the observed temperatures only represent the quickly cooled outer particle surface.

For the particle sizes that best fit the radiative heat loss model (R = 3 - 5 μm), t_c ~ 10 – 30 μs. This time occurs around the transition in the temperature curve. In this case, the heat conduction time is fast compared to the majority of the temperature observations. It is possible that the transition in the temperature decay relates to the heat conduction rate in the sphere; still, many additional simplifying assumptions remain. For example, the melt continually changes shape over the first 30 μs due to stretching (flow) and coalescing with other heated particulates. In all cases considered here, the best-fit source size is much smaller than the overall radial extent of the flash source. After the maximum intensity, the cooling source includes both individual, μm-sized particles and mm- to cm-sized solid mass.

In order to incorporate heat conduction fully into a model, it is necessary to numerically solve the equation for heat conduction for a sphere of density, ρ, specific heat, C_v, and thermal conductivity, k_c, at a radial position, r:

$$\frac{\partial T}{\partial t} = \frac{k_c}{\rho C_v} \cdot \frac{1}{r^2} \cdot \frac{\partial}{\partial r}\left(r^2 \frac{\partial T}{\partial r} \right). \tag{16}$$

If the sphere is assumed to have a blackbody surface, the following boundary condition applies when $r = R$ (the radius of the sphere):

$$k_c \cdot \frac{\partial T}{\partial r} = -\sigma T^4. \tag{17}$$

In addition, a complete model should include the effect of small cold clasts entrained during excavation. Such complications are best addressed using a finite difference or finite element analysis that is beyond the scope of this dissertation, but is an intriguing avenue for future work.

In addition to heat conduction, other factors need to be taken into account in order to produce a robust model with fewer simplifying assumptions. In reality, the source area rapidly expands with portions of the radiating source in a debris cloud, while other portions line the transient crater. During this time, the source temperature is non-uniform. The expansion and translational motion (for oblique impacts) change these portions of the source are exposed to the photodiodes, which in turn will affect the observed (integrated) temperature. Additionally, the model does not account for the effect of impact angle on any asymmetric heating or any shear heating that may occur.

These complications make it very difficult to fully model the impact flash analytically, especially during the earliest stage. Evolving source shapes (e.g., a sheet) need to be incorporated to try to find a better fit to the data. The physical interpretations proposed to explain the observed evolution of both temperature and intensity could be further tested by investigating the evolution of the source area (the final variable from Equation 1).

4.5 Source Area Evolution

If the radiating source area were constant, the flash intensity would depend only on the evolving temperature. In this case, the intensity and temperature curves would exhibit the same overall shapes, with coinciding maxima at $t = 0$ followed by gradual decays. Instead, the broad intensity peak is markedly delayed from the moment of first contact. Following Equation 1, this discrepancy must result from an evolving source area.

The temperature decreases while the intensity rises to its delayed broad peak; consequently, the source area must expand at least until the intensity peak is reached. The source occurs by increasing the number of radiating particles, either by the creation of new radiators or by exposing previously hidden radiators to the photodiodes (through dispersal or translational motion) or the transition of a debris cloud from optically thick to optically thin. Since the observed temperatures are integrated values, the calculated source area will not exactly match the actual source area; however, the results should be reasonably close. The calculated radiating source area will not be equivalent to the actual plume area if it is optically thin.

The source areas for 90º and 30º impacts are compared in Figure 10. The arrows indicate the time of the intensity peaks. In both cases, the source area increases through the time of the maximum intensity. By the time the 90º intensity profile reaches its maximum, the source area has already undergone most (85%) of its growth. When the 30º intensity profile reaches its maximum, the source area has undergone about 60% of its growth. The 30º source area is consistently larger than the 90º source area. This illustrates the importance of the dependence on the radiating source area. By 100 μs, the calculated source area remains constant; therefore, the intensity and temperature are related by the cooling rate of the emitting source.

Following [*Wen et al.*, 2006], an optically thin plume will have an emission flux (e_v) proportional to the radius (R) of the plume. The rate of change of the plume temperature is given by:

$$\frac{dT}{dt} \propto \frac{A_p \cdot e_v}{V_p} \sim \frac{f(R^2) \cdot f(R)}{f(R^3)} \sim f(1), \tag{18}$$

where A_p and V_p are the surface area and the volume of the plume. Thus, the rate of the temperature decay will be independent of the plume size. If the plume is optically thick, the emission flux is equal to blackbody radiation, B_v, which is independent of plume size:

$$\frac{dT}{dt} \propto \frac{A_p \cdot B_v}{V_p} \sim \frac{f\left(R^2\right) \cdot f\left(1\right)}{f\left(R^3\right)} \sim f\left(R^{-1}\right), \tag{19}$$

making the temperature decay rate inversely proportional to the plume size (larger plumes have slower cooling rates). If better constraints can be made on the size of the source area, these relations can be used to examine the changing opacity of the expanding source.

4.6 Luminous Efficiency

Knowing the temperature and the source area of the impact flash are important for studying early time impact processes and determining the thermal conditions experienced by the materials involved. For the purpose of observing impacts, however, it is often more practical to measure the intensity of the flash than its temperature or source area. The luminous efficiency is a convenient value that can be used to estimate the unknown initial conditions of an impact. The luminous efficiency (η) is a dimensionless quantity that measures the fraction of initial kinetic energy (KE_o) that is converted into luminous energy (LE) over a given wavelength range (λ_1 to λ_2):

$$\int_{\lambda_1}^{\lambda_2} LE = \eta \cdot KE_o. \tag{20}$$

This is a wavelength-specific version of Equation 6. Luminous efficiency is typically referenced with respect to the visible wavelength range.

Numerical simulations have considered the luminous efficiency of impacts in the visible wavelength range [*Nemtchinov et al.*, 1998; *Shuvalov et al.*, 1999]; however, the results span many orders of magnitude (10^{-6}-10^{-1}) and consider only the evolving vapor phases. Estimates also have been based on laboratory experiments (10^{-6}-10^{-4}) [*MacCormack*, 1963; *Eichhorn*, 1975; *Kadono and Fujiwara*, 1996] and lunar impacts (~10^{-3}-10^{-2}) [*Bellot Rubio et al.*, 2000; *Ortiz et al.*, 2006]. The experimental studies address only impacts into metal targets, which have far shorter impact flash durations than impacts into particulate targets. Estimates from observed lunar impacts rely greatly on uncertain projectile size estimates of meteor streams and involve impacts at much higher velocities where vaporization becomes important. An increase in velocity should lead to an increase in luminous efficiency because the amount of energy emitted in the visible wavelength range increases with increasing temperatures. The present study calculates the luminous energy and luminous efficiency of experimental impacts into particulate targets without significant vaporization. The results have implications for planetary impact observations that currently rely on theoretical and non-particulate target luminous efficiency estimates.

The total luminous energy (*LE*) of an impact was given in Equation 5. Integrating over the total duration of the flash yields the total *LE* of an impact; integrating only over a portion of the signal yields the cumulative energy emitted during the chosen time span. The luminous energy for visible wavelengths corresponding to the photodiode (350 - 1100 nm) was calculated for 90º and 30º impacts at similar velocities (~5.3 km/s). Figure 11 shows the cumulative luminous energy versus time for these impacts. This representation highlights the significance of the long-duration "tail" portion of the intensity signal. The maximum intensity for the 90º and 30º impacts occurs at t = 15 μs and t = 27 μs, respectively, and decays to half of its maximum value by t = 98 μs and t = 194 μs. As much as 50-60% of the visible luminous energy is emitted after this time. Such late-time contributions will significantly increase the impact luminous efficiency. Thus, it is important to consider all of the radiation emitted by an impact versus just that emitted through the main intensity peak. If the sensitivity of a detector is too low, it will not capture this portion of the curve, and an estimate of the original kinetic energy of the impact will be too low.

As an exercise, the luminous energy for infrared wavelengths (1.0 – 4.8 μm) also was calculated. Since these experiments involved color temperatures ranging from 3000-4500 K, more energy is released in the infrared wavelength range than in the visible wavelength range. Less energetic impacts are therefore easier to detect in the infrared (rather than visible) wavelength range. A comparison of the visible and infrared luminous energy outputs for the 90º and 30º impacts is also illustrated in Figure 11.

For the current experiments, η values were calculated for both the visible and infrared wavelength ranges. Luminous efficiency values for both integration times are listed for the 90º and 30º impacts in Table 2. For the long integration time, η_{vis} is on the order of 5×10^{-5} for both impact angles. This observed value falls within both the theoretical and the experimentally observed ranges. For a given set of initial conditions, a 30º impact has higher maximum intensity than a 90º impact, but vertical impacts exhibit higher temperatures after the intensity peak (as described in Section 3.2) and therefore have higher total luminous energy outputs. These factors combine to result in similar luminous efficiency values. In both cases, the luminous efficiency in the infrared range is greater than in the visible wavelength range (see Table 2).

5. Conclusions

The thermal evolution of the impact flash out to 200 μs was examined along with probable underlying controlling processes. The impact angle and velocity were varied to assess their effects on the flash temperature for a common particulate silicate target (pumice). The following main conclusions are drawn based on these experiments.

(1) The flash temperature starts at a maximum on first contact between projectile and target. The temperatures are difficult to observe during the first 1 - 2 μs. This time corresponds to the peak shock compression and projectile penetration into the target, which manifest as the early-time spike in the intensity evolution. In contrast to previous results for vapor clouds, the maximum temperature increases with decreasing impact angle. This difference likely represents the effect of phase transitions for easily volatized targets. Later temperatures, however, are higher for vertical impacts, possibly reflecting the effect of source distribution and cooling. In general, the temperature increases with velocity.

(2) Multiple power laws best approximate the temperature evolution, with the break occurring at the time of maximum intensity. The break in the power law represents a transition in the physical processes controlling the exposure and generation of the radiating source. While partial vaporization also might limit maximum temperatures (and affect evolution), analysis here reveals that the exposure of the source area plays the dominant role.

(3) The increase to the maximum intensity (0 – 20 μs) is caused by a growing source area. In general, the source area produced by a 30º impact is larger than that produced by a vertical impact.

(4) Both simplistic modeling the cooling of the source as solid spheres and analysis of the source area evolution suggest that the cooling rate after the time of maximum intensity is consistent with an optically thin source. Even though each luminous particle of solid or melt is optically thick, they are separated enough to behave optically thin as a whole.

(5) The long-duration "tail" portion of the impact flash intensity contributes a significant portion of the luminous energy of the total flash, with as much as 60% of the visible-wavelength energy being emitted after the intensity peak. Consequently, the intensity peak alone cannot be used to determine the luminous efficiency. Moreover, low instrumental sensitivity may result in underestimations of the total luminous energy output of an observed impact flash.

(6) As impact velocities increase, greater vaporization will occur. Luminous energy from vapor condensates, however, represents a small fraction of all sources (melt, heated ejecta). Consequently the calculated luminous efficiencies and trends for these experiments should reasonably apply to faster impacts into the lunar regolith as well (up to a limit in size).

Acknowledgements

We appreciatively acknowledge the assistance of the NASA Ames Vertical Gun Range crew (D. Holt, R. Smythe, D. Bowling, and C. Cornelison) and the instrument design of W. Patterson at Brown University. This research was supported by NASA grant No. NAGS-11538 and the NASA Graduate Student Researchers Program (04-6011H).

References

Ang, J. A. (1990), Impact flash jet initiation phenomena, *International Journal of Impact Engineering*, *10*, 23-28.

Artem'eva, N. A., I. B. Kosarev, I. V. Nemtchinov, I. A. Trubetskaya, and V. V. Shuvalov (2001), Light flashes caused by Leonid meteoroid impacts on the lunar surface, *Solar System Research*, *35*(3), 177-180.

Baird, J. K., G. R. Hough, and T. R. King (1997), Velocity dependence of impact fluorescence, *International Journal of Impact Engineering*, *19*(3), 273-276.

Baird, J. K., and T. R. King (1999), A Wien displacement law for impact radiation, *International Journal of Impact Engineering*, *23*, 39-49.

Bellot Rubio, L. R., J. L. Ortiz, and P. V. Sada (2000), Luminous efficiency in hypervelocity impacts from the 1999 lunar Leonids, *The Astrophysical Journal*, *542*, L65-L68.

Cintala, M. J. (1992), Impact-induced thermal effects in the lunar and mercurian regoliths, *Journal of Geophysical Research*, *97*(E1), 947-973.

Dahl, J. M., and P. H. Schultz (2001), Measurement of stress wave asymmetries in hypervelocity projectile impact experiments, *International Journal of Impact Engineering*, *26*, 145-155.

Eichhorn, G. (1975), Measurements of the light flash produced by high velocity particle impact, *Planetary and Space Science*, *23*, 1519-1525.

Eichhorn, G. (1976), Analysis of the hypervelocity impact process from impact flash measurements, *Planetary and Space Sciences*, *24*, 771-781.

Ernst, C. M., and P. H. Schultz (2002), Effect of velocity and angle on light intensity generated by hypervelocity impacts, *LPSC*, *XXXIII*, #1782.

Ernst, C. M., and P. H. Schultz (2003), Effect of initial conditions on impact flash decay, *LPSC*, *XXXIV*, #2020.

Ernst, C. M., and P. H. Schultz (2004), Early-time temperature evolution of the impact flash and beyond, *LPSC*, *XXXV*, #1721.

Gehring, J. W., and R. L. Warnica (1963), An investigation of the phenomena of impact flash and its potential use as a hit detection and target discrimination technique, *6th Symposium on Hypervelocity Impact*, 627-681.

Jean, B., and T. L. Rollins (1970), Radiation from hypervelocity impact generated plasma, *American Institute of Aeronautics and Astronautics Journal*, *8*, 1742-1748.

Kadono, T., and A. Fujiwara (1996), Observation of expanding vapor cloud generated by hypervelocity impact, *Journal of Geophysical Research*, *101*(E11), 26,097-26,109.

Love, S. G., F. Hörz, and D. E. Brownlee (1993), Target porosity effects in impact cratering and collisional disruption, *Icarus*, *105*, 216-224.

MacCormack, R. W. (1963), Investigation of impact flash at low ambient pressures, *6th Symposium on Hypervelocity Impact*, 613-625.

Melosh, H. J., N. A. Artemieva, A. P. Golub, I. V. Nemtchinov, V. V. Shuvalov, and I. A. Trubetskaya (1993), Remote visual detection of impacts on the lunar surface, *LPSC*, *24*, 975-976.

Nemtchinov, I. V., V. V. Shuvalov, N. A. Artemieva, B. A. Ivanov, I. B. Kosarev, and I. A. Trubetskaya (1998), Light Impulse Created by Meteoroids Impacting the Moon, *LPSC*, *XXIX*, # 1032.

Nemtchinov, I. V., V. V. Shuvalov, N. A. Artemieva, I. B. Kosarev, and I. A. Trubetskaya (1999), Expansion, radiation and condensation of vapor cloud, created by high-velocity impact onto a target in vacuum, *International Journal of Impact Engineering*, *23*, 651-662.

Ortiz, J. L., F. J. Aceituno, J. A. Quesada, J. Aceituno, M. Fernandez, P. Santos-Sanz, J. M. Trigo-Rodriguez, J. Llorca, F. J. Martin-Torres, P. Montanes-Rodriguez, and E. Palle (2006), Detection of sporadic impact flashes on the Moon: Implications for the luminous efficiency of hypervelocity impacts and derived terrestrial impact rates, *Icarus*, *184*(2), 319-326.

Pierazzo, E., and H. J. Melosh (2000a), Melt production in oblique impacts, *Icarus*, *145*, 252-261.

Pierazzo, E., and H. J. Melosh (2000b), Understanding oblique impacts from experiments, observations, and modeling, *Annual Review of Earth And Planetary Sciences*, *28*, 141-167.

Schultz, P. H. (1996), Effect of impact angle on vaporization, *Journal of Geophysical Research*, *101*(E9), 21,117-21,136.

Schultz, P. H., C. M. Ernst, and J. L. B. Anderson (2005), Expectations for crater size and photometric evolution from the Deep Impact collision, *Space Science Reviews*, *117*, 207-239.

Schultz, P. H., S. Sugita, C. A. Eberhardy, and C. M. Ernst (2006), The role of ricochet in impact vaporization, *International Journal of Impact Engineering*, *33*, 771-780.

Shuvalov, V. V., N. A. Artemieva, I. B. Kosarev, I. V. Nemchinov, and I. A. Trubetskaya (1999), Small comets impacting the Moon, *LPSC*, *XXX*, #1045.

Sugita, S., P. H. Schultz, and M. A. Adams (1998), Spectroscopic Measurements of Vapor Clouds Due to Oblique Impacts, *Journal of Geophysical Research*, *103*(E8), 19,427-19,441.

Wen, S.-B., X. Mao, R. Greif, and R. F. Russo (2006), Radiative cooling of laser ablated vapor plumes: Experimental and theoretical analyses, *Journal of Applied Physics*, *100*, 053104.

Table 1. Temperature and β values with impact parameters.

	θ	v (km/s)	a (cm)	T_{max} (K)	T_{100} (K)	T_{200} (K)	T_{τ} (K)	β
040634	15	4.25	6.35	4190	2880	2630	2980	0.14
040633	15	5.49	6.35	3820	2650	2430	2610	0.15
031205	30	6.04	3.18	4480	3190	2960	3330	0.11
031230	30	5.20	4.76	4310	2860	2640	2870	0.12
040603	30	5.26	4.76	4000	3010	2840	2950	0.09
050135	30	5.26	4.76	3990	3000	2800	2980	0.10
040604	30	5.33	4.76	3780	3000	2830	2980	0.08
050901	30	5.52	6.35	4010	2930	2750	2950	0.10
040607	45	5.54	4.76	4170	3110	2900	3000	0.08
040608	45	5.72	4.76	4200	3200	3050	3100	0.08
040609	45	6.03	4.76	4260	3290	3250	3230	0.07
060718	60	4.94	6.35	3790	2990	2740	------	0.09
031208	90	5.88	3.18	3740	3160	3030	3140	0.05
040612	90	5.32	4.76	3500	3140	3030	2900	0.06
040605	90	5.33	4.76	3770	3200	3100	3030	0.04
031229	90	5.46	4.76	3890	3090	2950	2920	0.06

Table 2. Luminous efficiency values for visible and infrared wavelength ranges.

Time (μs)	λ Range	η_λ (90º)	η_λ (30º)
0 – 200	VIS	2×10^{-5}	3×10^{-5}
0 – 1000	VIS	5×10^{-5}	4×10^{-5}
0 – 200	IR	5×10^{-5}	7×10^{-5}
0 – 1000	IR	2×10^{-4}	2×10^{-4}

Figure Captions

Figure 1. The impact flash intensity evolution (0 – 1000 μs) for a Pyrex/pumice powder impact. The 4.76 mm-projectile impacted at 30º and 5.33 km/s. There are three main components to the light curve: (1) an early-time spike; (2) a prominent, broad intensity peak; and (3) a long decay signal that persists well after the observed time window. The data resolution is 100 ns.

Figure 2. Seven channels of raw impact flash intensity data (0 – 200 μs) from the same impact as in Figure 1 (30º, 5.33 km/s). The unfiltered channel (black) has the highest intensity. The filtered channels are represented by different colors and the legend labels correspond to the central wavelength of each filter (nm). Note that because raw (pre-calibration) data are shown, the filtered channels do not exhibit the relative values that would be expected from a thermal radiating source, and the sum of the filtered channels add up to significantly higher intensity values than the unfiltered channel. All seven curves have similarly timed intensity peaks.

Figure 3. Evolutions of the impact flash temperature (black) and intensity (blue) (0 - 200 μs) for a 30º Pyrex/pumice powder impact (again, the same impact as in Figure 1). The arrow points to the location on the temperature corresponding to the time of the maximum intensity. There is no major corresponding feature in the temperature evolution. The temperature starts at a maximum (~3800 K in this case) and decays over the time observed (to ~2700 K at 200 μs).

Figure 4. Plot of the maximum temperature (T_{max}, measured at t = 2 μs) as a function of impact velocity for Pyrex/pumice powder impacts at various angles. Projectiles were 4.76 mm in diameter, except where indicated by brackets (6.35 mm) or parentheses (3.18 mm). The temperature error is shown on the 60º data point. The solid line represents the theoretical quadratic relationship from *Baird et al.* [1997] assuming a 90º impact and using $N = 1.00 \times 10^{25}$ (the value for SiO_2). The only impacts lying above the line occurred at low impact angles. In general, T_{max} increases with decreasing impact angle and increases with velocity. The vaporization temperature is indicated by a dashed line.

Figure 5. Later-time temperature data from the same impacts shown in Figure 4. (a) Temperature measured at t = 100 μs and t = 200 μs as a function of velocity. For 30º impacts, these times correspond to the decay portion of the intensity curve, but for vertical impacts these times correspond to the broad intensity peak. Though there is a general relationship where higher velocities produce higher temperatures, no clear relationship is observed. By these later times, higher temperatures are observed for higher impact angles. The v^2 relationship [*Baird et al.*, 1997] is indicated by the solid line. (b) The same plot with the previous data shown by outlined data symbols. Temperatures measured at τ = 250 are shown by solid symbols. A definite power-law relationship between temperature and impact velocity is observed where the exponent ranges between 0.5 – 1.0. The data do not follow a quadratic relationship.

Figure 6. Impact flash intensity (blue line) and temperature (open squares) evolutions out to 200 μs for (a) 90º, (b) 45º, and (c) 30º impacts. The temperature curves are fit with power-law decays (solid black line, exponent (β) listed in Table 1). The decay rates are dependent on impact angle. The vertical dashed lines correspond to the time of maximum intensity. The absolute temperature and intensity values are higher for the 45º impact due to a difference in impact velocity (5.54 km/s versus 5.33 km/s). Although the data resolution is 100 ns, data markers are only displayed every 5 μs for easier viewing. The intermediate (non-displayed) data points are all continuous with the displayed data.

Figure 7. The same intensity and temperature evolutions as in Figure 7, this time shown from 0 – 20 μs. The data are fit with the same power laws. The maximum intensity times are indicated dashed lines. The power law fits deviate from the observations until approximately the time of the maximum intensity for 90º (a) and for 30º (c). For 45º (b), the observations match the fit well at all times. Although the data resolution is 100 ns, data markers are only displayed every 2 μs for easier viewing. The intermediate (non-displayed) data points are all continuous with the displayed data.

Figure 8. Log-log plot of the intensity (blue line) and temperature (open squares) evolutions from 0 – 200 μs. This representation clearly shows the deviations of the observed temperature data from the power-law fit (solid black line). Dashed lines represent the maximum intensity times. Again the 90º and 30º power-law fits start to match well after the maximum intensity time. Data markers are displayed every 1 μs.

Figure 9. Comparison of the observed temperature evolution (solid lines) with best fit analytical models (dashed lines) assuming solid, spherical (3 – 5 μm diameter) radiating blackbody sources. These model parameters match the majority of the observed decay (30 – 200 μs) for 45º and 30º but cannot match the early decay.

Figure 10. The evolution of the estimated radiating source area for 90º and 30º impacts at 5.33 km/s. The arrow indicate the maximum intensity times. By the time the 90º impact intensity reaches its maximum, the source area has completed most of its growth (85%). For the 30º impact, 60% of its growth has been completed by the maximum intensity time. The overall area for the 30º impact is consistently larger than for the 90º impact.

Figure 11. Calculated cumulative luminous energy for 5.5 km/s Pyrex/pumice powder impacts at 90º and 30º. The luminous energy is calculated from the observed temperature and source area through time. The evolutions of the radiating energy in the visible (350 – 1100 nm) and infrared (1.0 – 4.8 μs) are shown. More energy is radiated in the infrared range than in the visible range under these impact conditions. The total energies emitted for both angles are comparable.

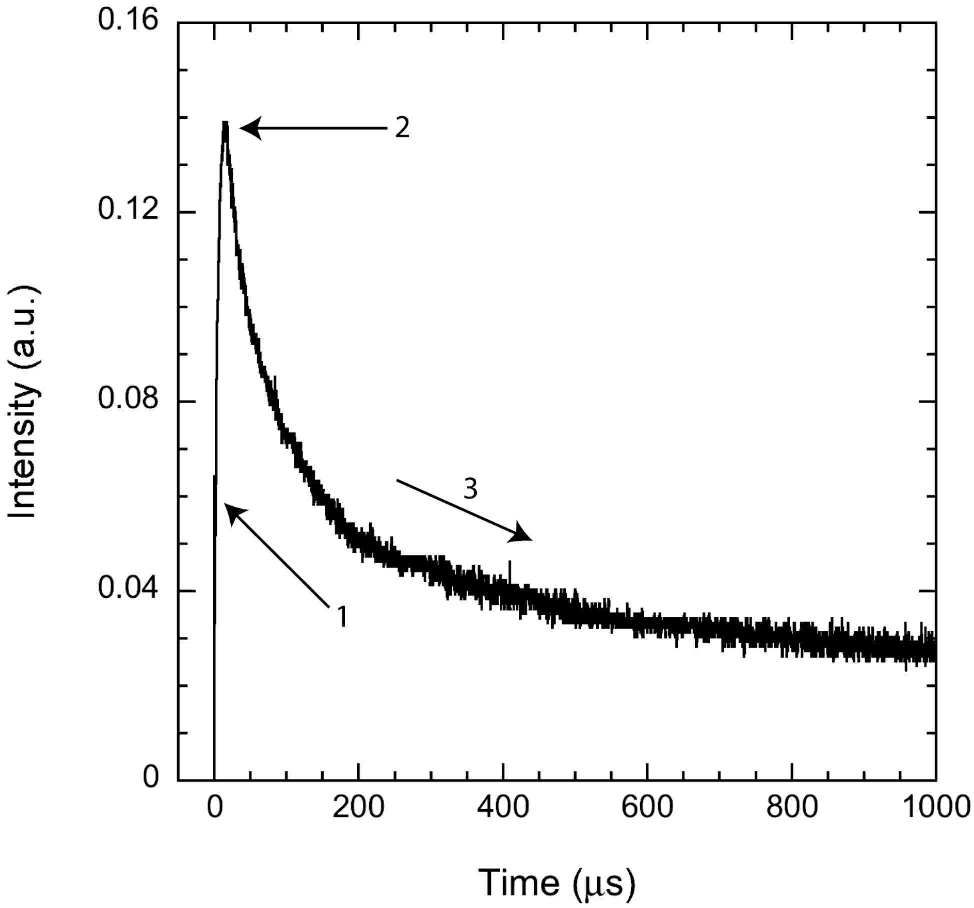

Chapter 2, Figure 1

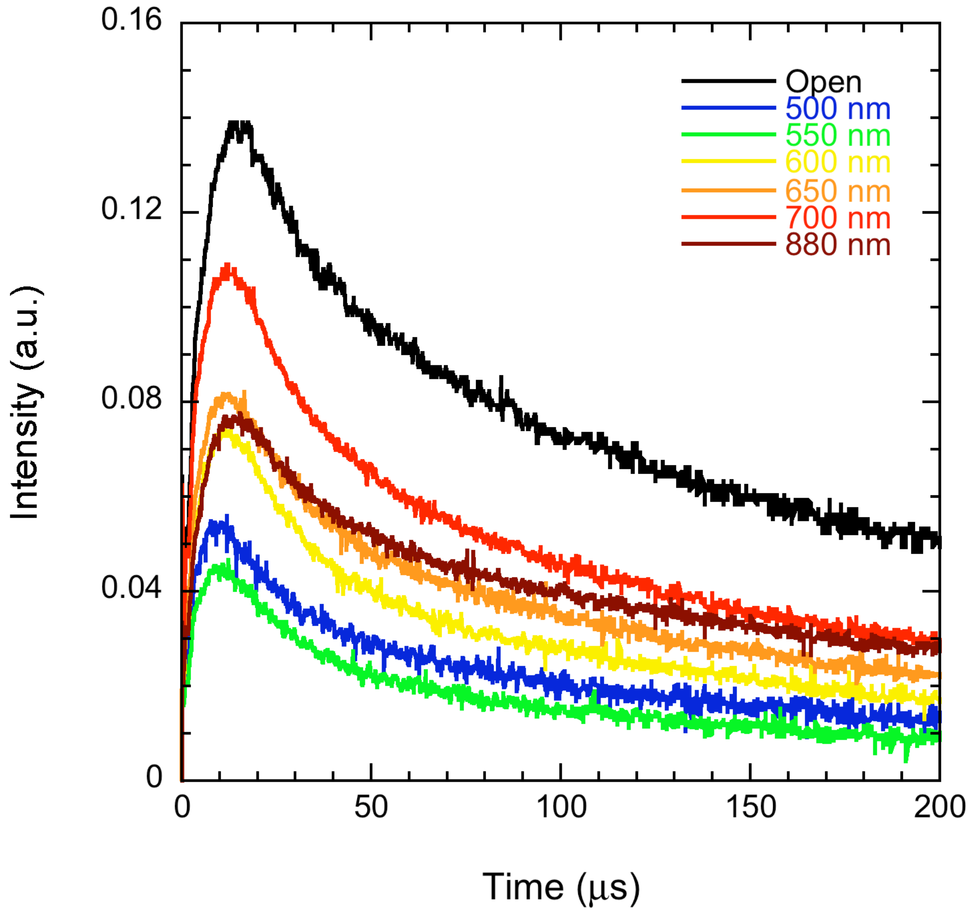

Chapter 2, Figure 2

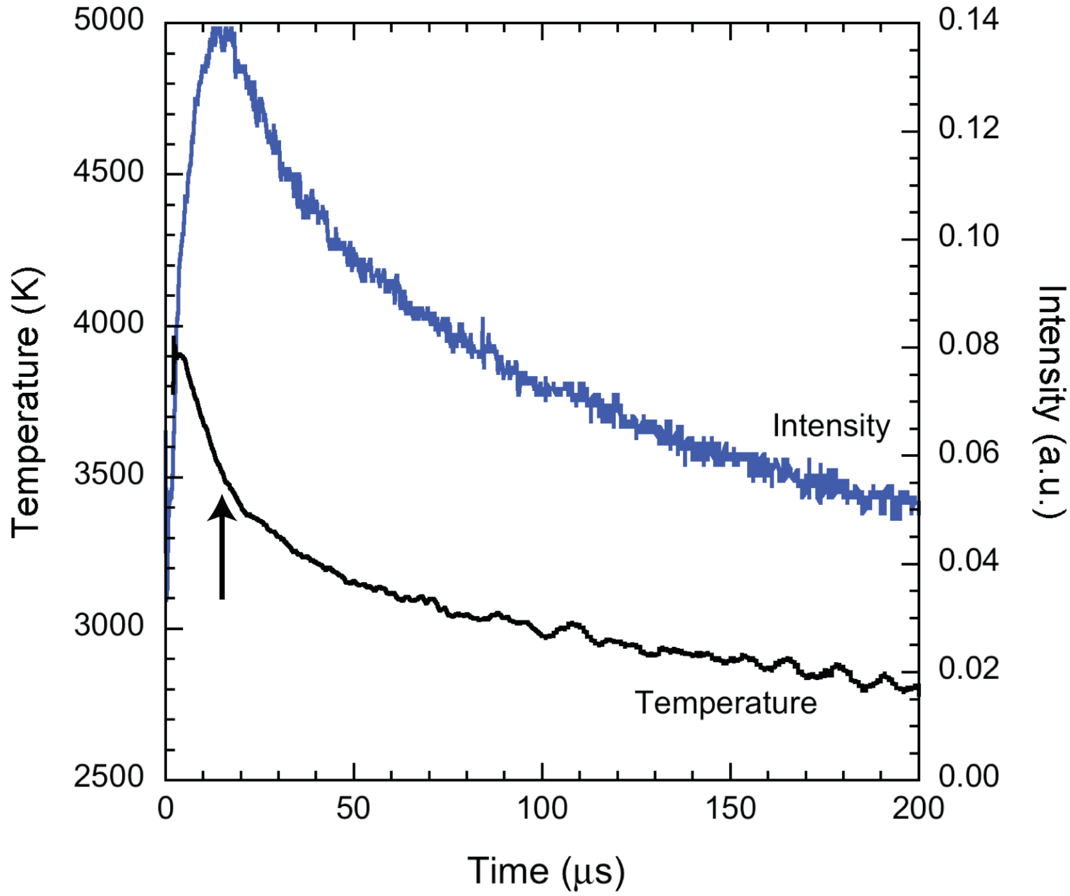

Chapter 2, Figure 3

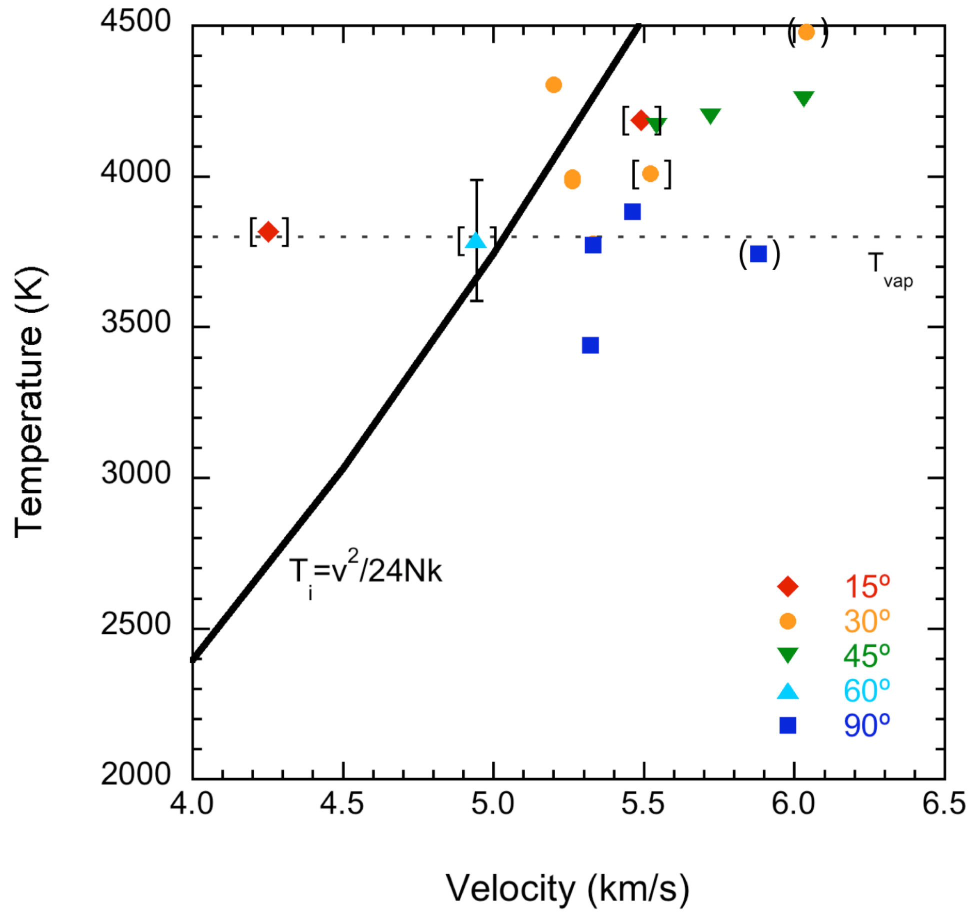

Chapter 2, Figure 4

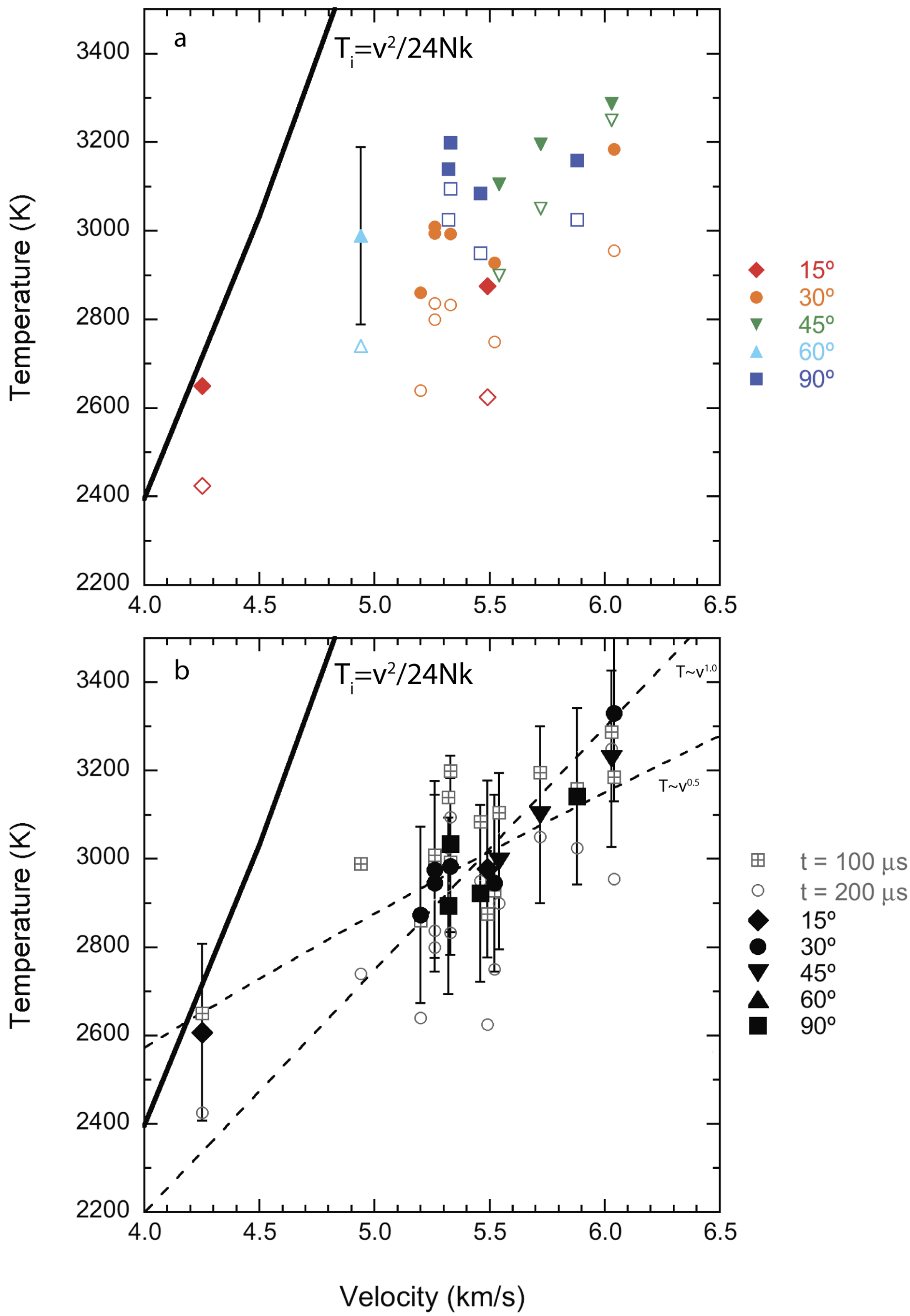

Chapter 2, Figure 5

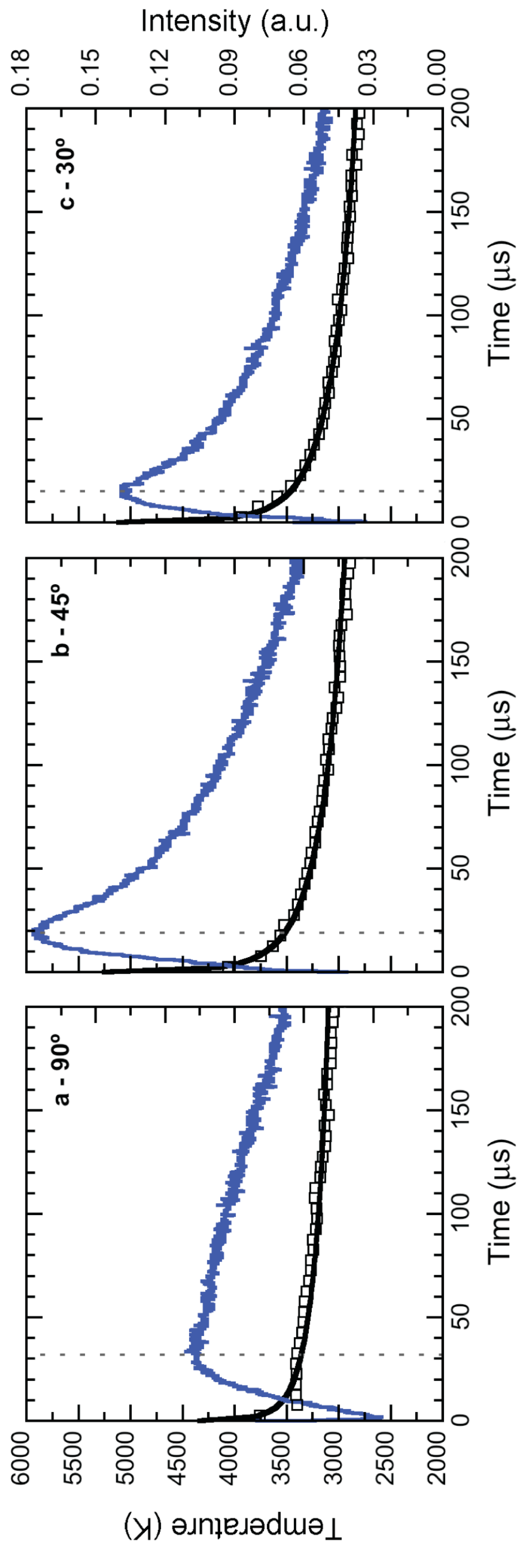

Chapter 2, Figure 6

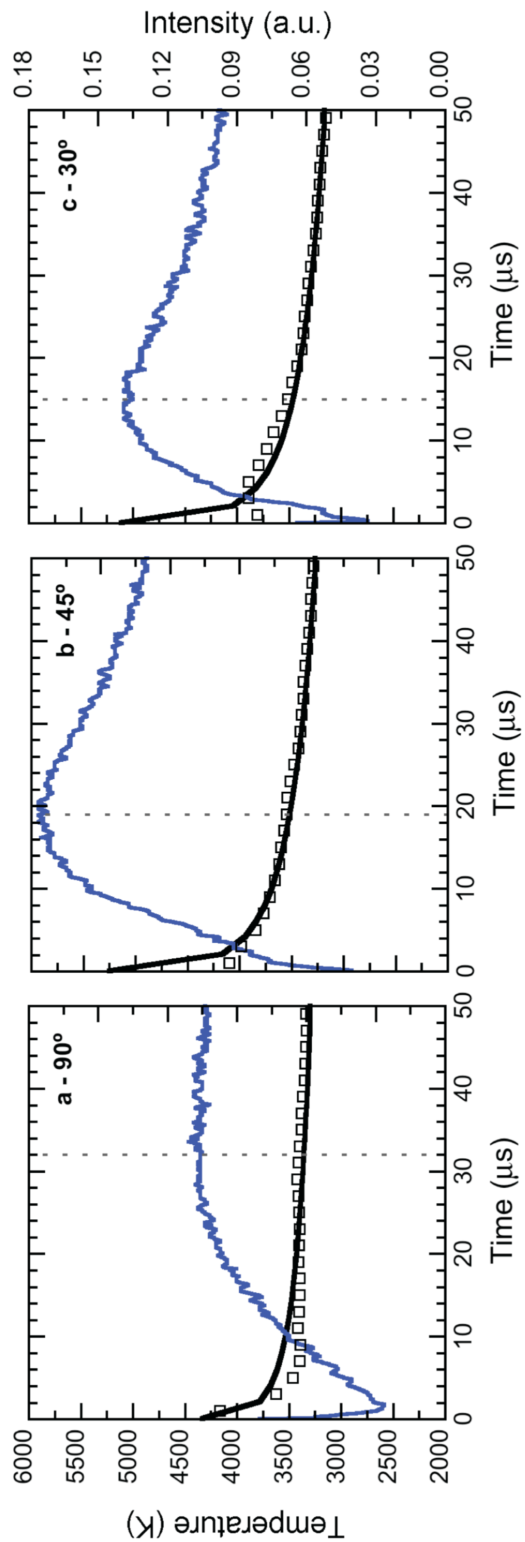

Chapter 2, Figure 7

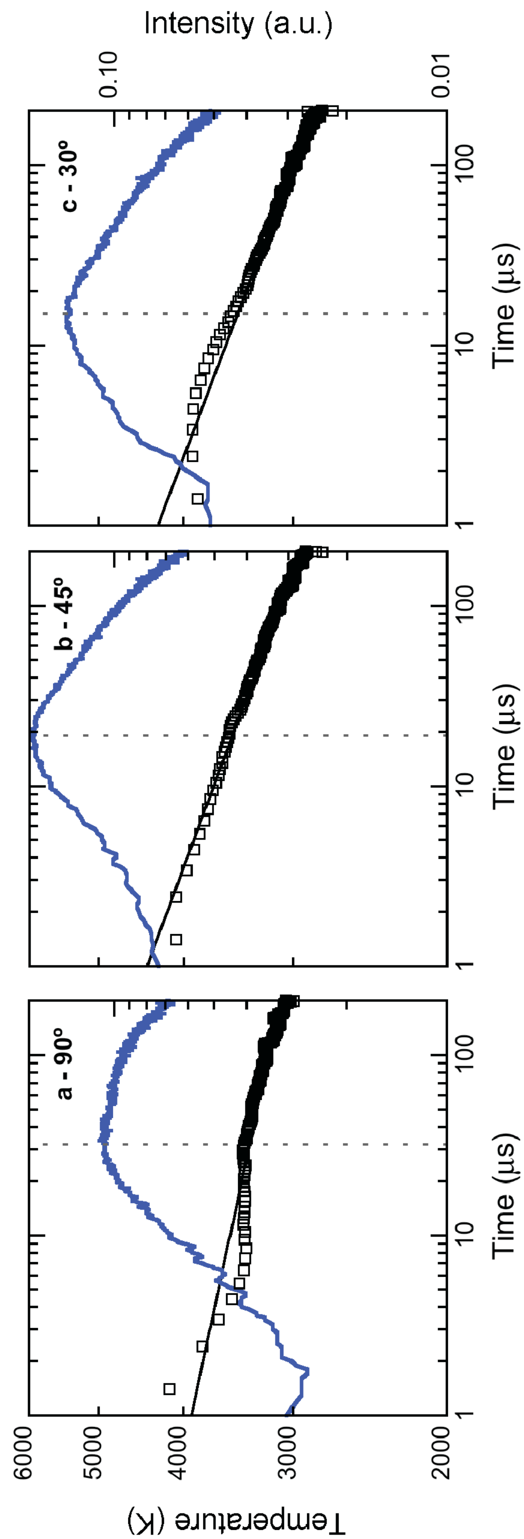

Chapter 2, Figure 8

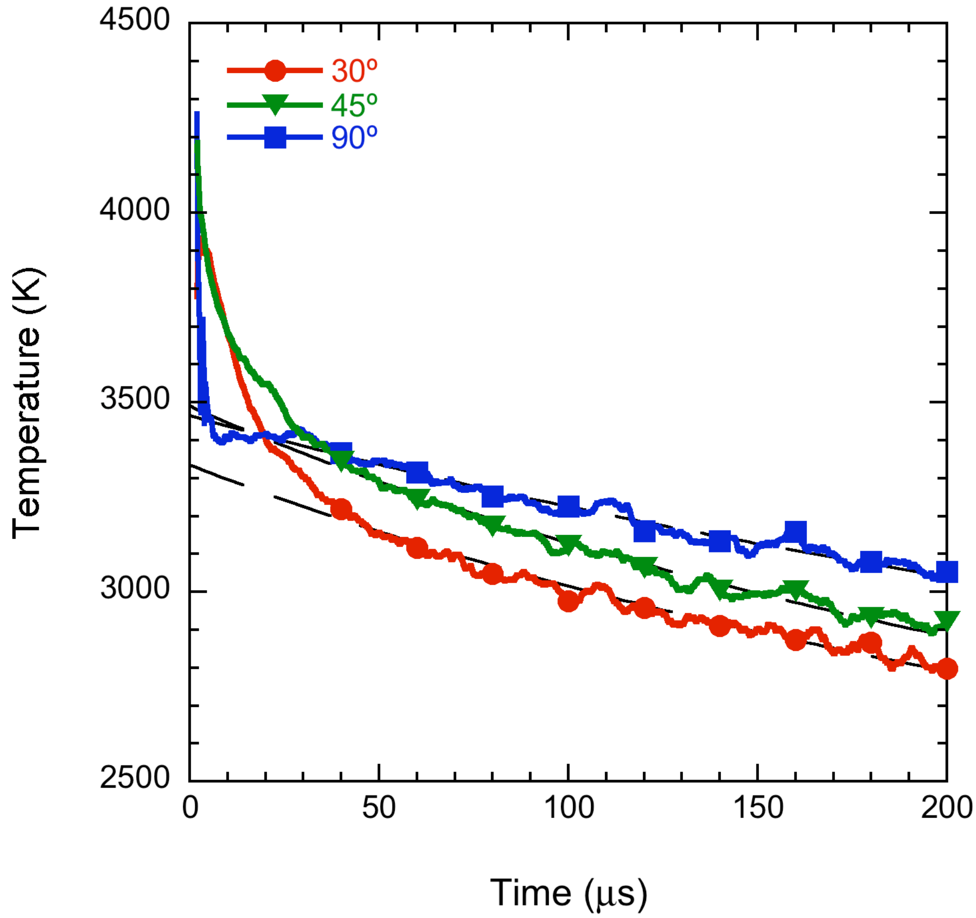

Chapter 2, Figure 9

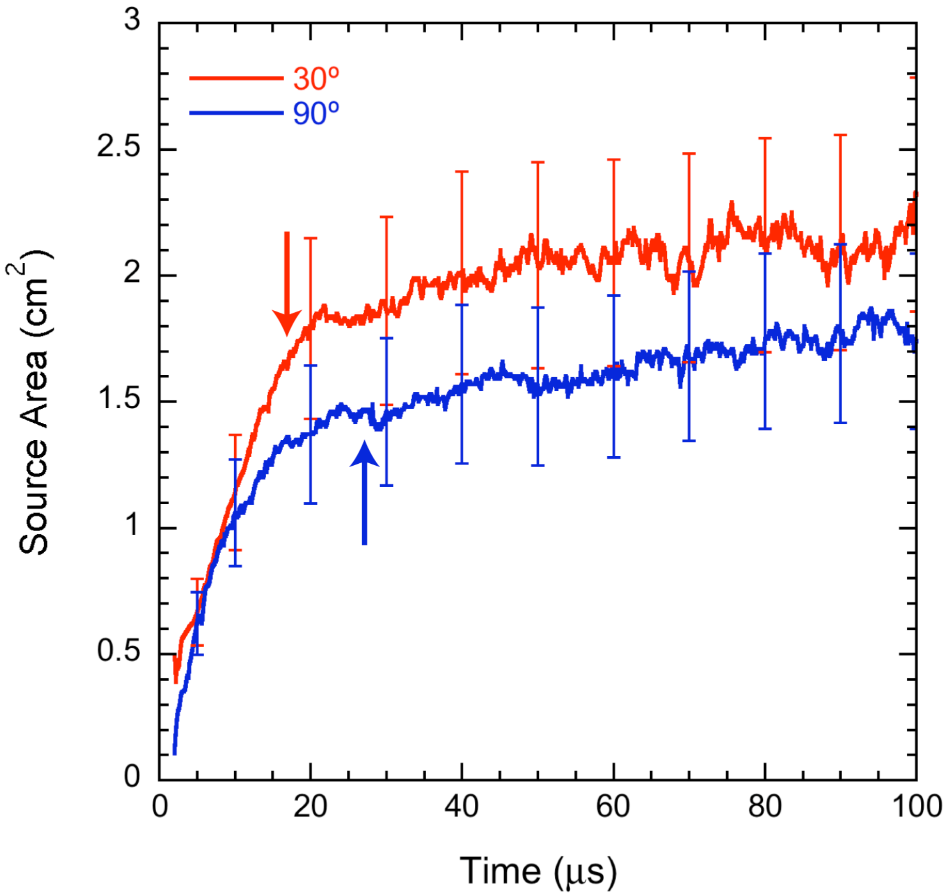

Chapter 2, Figure 10

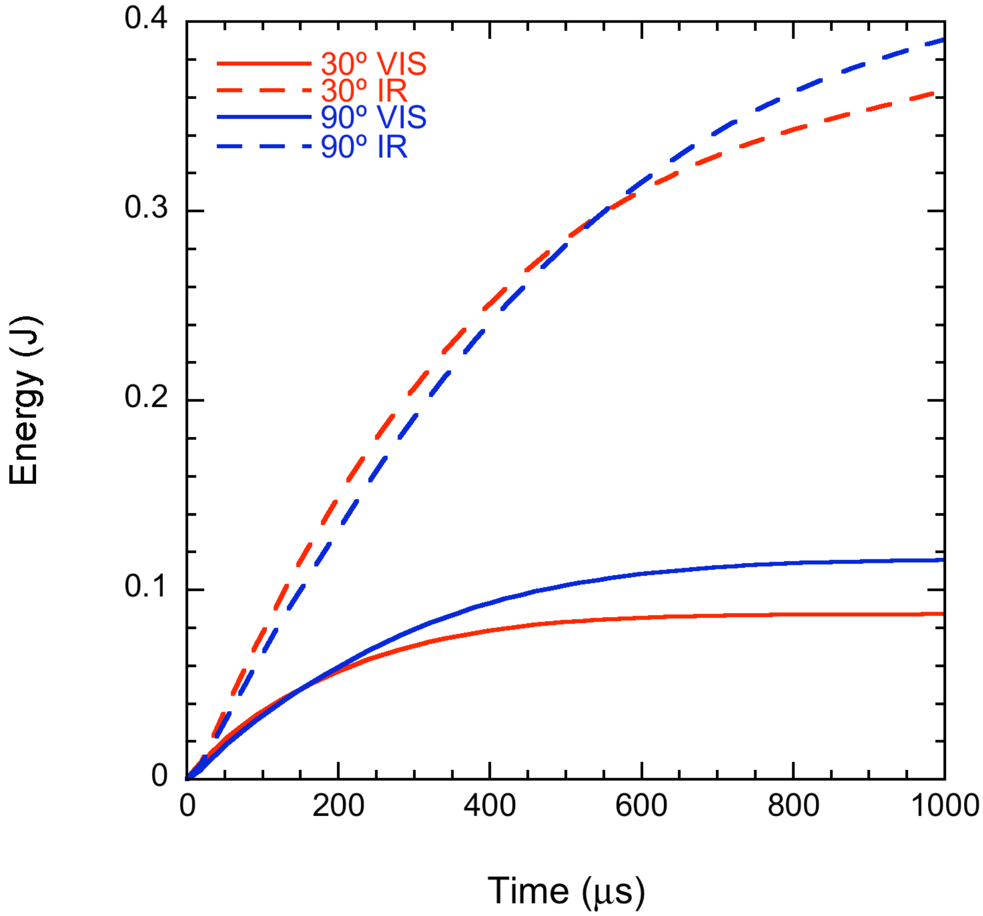

Chapter 2, Figure 11

Chapter 3

Spatial Evolution of the Impact Flash

Carolyn M. Ernst

Peter H. Schultz

Department of Geological Sciences

Box 1846

Brown University

Providence, RI 02912

Abstract

The impact flash is a short-duration phenomenon, making it difficult to observe and study in detail. Most previous studies of the flash have obtained temporally resolved intensity measurements. These data remain spatially integrated; therefore, the source location of the flash cannot be determined. Images taken by a short-exposure CCD camera are used in order to investigate the spatially resolved temperature and source distribution of the flash. The processes generating the impact flash and controlling its evolving distribution are investigated by using these images in conjunction with temporally resolved intensity data. The temperature and source area values measured from the images are consistent with those observed and calculated using the photodiode systems used extensively in Chapters 1 and 2. Impact angle has a discernable effect on the spatial distribution of the radiating material, with a larger projected area observed at lower angles. The primary source location for impacts of Pyrex projectiles into pumice powder targets is along the projectile/target interface. This source evolves through time to line the transient crater. The addition of high porosity or volatiles to the target drastically changes the distribution and location of the heated material, resulting in major differences in the observed source distribution and reductions of the flash intensity. For highly porous targets, much of the heated material is confined into a deeper transient crater. For impact-vaporized targets, the radiating source is dispersed above the target surface and entrained in a vapor plume, instead of primarily lining the transient crater cavity.

1. Introduction

The impact flash can be challenging to observe in detail, due to its short duration. This is especially true at laboratory scales. Although a "long" flash may last for several milliseconds, the most significant intensity changes occur on timescales of microseconds. If observations can be made that sufficiently resolve these changes, the flash provides a means to assess small-scale details of the impact process at early times.

The most common method for temporally resolving the impact flash has been the use of photodiodes [e.g., *Gehring and Warnica*, 1963; *Jean and Rollins*, 1970; *Eichhorn*, 1976; *Kadono and Fujiwara*, 1996]. These studies primarily examined impacts into solid (usually metallic) targets and the resulting flashes were of very short duration (on the order of microseconds). More recent studies have shown that impacts into non-volatile particulate targets produce long-duration impact flashes that can last > 2 ms at laboratory scales [*Ernst and Schultz*, 2002; 2003], with small amounts of cooling, incandescent ejecta persisting for more than 50 ms.

The flash produced by impacts into particulate targets was closely examined in Chapters 1 and 2 using photodiodes able to temporally resolve the sub-microsecond-scale flash evolution. Chapter 1 explored the intensity of the impact flash through time. The intensity evolution was found to be a good indicator of initial conditions, especially in relation to the impact velocity, angle, and target type. For pumice powder targets, the dominant radiation sources are thermal emissions from melt droplets and heated particulates that are located both lining the transient cavity as well as in a cloud above the crater. Whether the intensity evolution corresponds to changes in temperature, emitting source area, or a combination of the two could not be uniquely determined.

Chapter 2 addressed this ambiguity by using multiple photodiodes to determine the impact flash temperature. The observed thermal evolution begins with a maximum temperature at the first contact between the projectile and target. The temperature then steadily decays through time. A combination of temperature and intensity measurements reveals that a growing source area causes the observed rise to the broad intensity peak, after which the cooling of the source material controls the intensity decay.

While photodiodes can record the impact flash at very high time resolution, the resulting intensity observations are spatially integrated over the entire emitting source region. Therefore, the physical distribution of the light source cannot be determined from such data alone. The actual radiating source distribution is non-uniform and the heated material moves and expands through time.

The combination of photodiode data and camera images provides temporal and spatial resolution of the flash [*Ernst and Schultz*, 2007b]. This combination allows several issues to be addressed. (1) How representative of the true values are the integrated temperatures and areas calculated by the photodiode data (Chapter 2)? (2) What are the distribution and evolution of the radiating material? (3) What process causes the observed early-time intensity evolution? (4) What effect does the introduction of target porosity or vaporization have on the temperature and distribution of heated material?

The present study addresses these questions primarily using experimental impacts of Pyrex projectiles into pumice powder targets (hereafter, Pyrex/pumice powder impacts). The focus is on the first 20 μs after impact, when the greatest changes in intensity occur. Short exposure images of the flash are captured to spatially resolve the temperature and the projected source area distribution. These observations are compared with simultaneously recorded photodiode data to gauge the consistency of the two datasets and to determine the source of the photodiode-observed light. The shape and distribution of the radiating source are assessed with a focus on the effect of impact angle. A set of sequential camera images is then compared to a simultaneously recorded photodiode intensity curve in order to examine the physical processes controlling the observed flash signal. The distribution of the radiating source is compared for impacts into different target materials. Interpretations of these observations are then discussed.

2. Experimental Design

Several series of experiments were performed at the NASA Ames Vertical Gun Range (AVGR). The two-stage light gas gun is able to fire small projectiles $\leq$ 6.35 mm in diameter at velocities up to 6.5 km/s into a target chamber large enough to permit the free expansion of the ejecta and thermal plume without interference from the chamber walls over the observed time. The design of this facility allows the variation of impact angle from vertical (90º) to 15º. The study of oblique impacts is essential because the most common impact angle on any planetary surface is 45º and only 0.75% of impacts occur at angles greater than 85º (or less than 5º) [*Gilbert*, 1893; *Shoemaker*, 1962]. Because of the ability to vary impact angle, targets can be correctly oriented with respect to gravity, allowing the use of particulate and layered targets and permitting proper crater growth. These factors all significantly affect the observed impact flash signal.

In the present experiments, 4.76 and 6.35 mm-diameter Pyrex spheres impacted at angles of 90º, 60º, 45º, 30º, and 15º. Different targets were chosen for their specific characteristics, including pumice powder (non-volatile, silicate, particulate), sieved perlite granules (high porosity), and dolomite powder (easily vaporizable under laboratory conditions). The composition and properties of the materials used in this study are listed in Table 1. Two separate velocity ranges were used. Most experiments used velocities between 4.25 and 6.04 km/s over a range of impact angles. One series, however, was performed at lower velocities between 1.60 and 1.90 km/s at an impact angle of 60º. Such low-velocity impacts allow the isolation of processes responsible for the flash without significant melting. The chamber pressure was reduced to near-vacuum conditions (< 0.6 Torr).

An intensified CCD camera system capable of < 5ns gate widths captured the impact flash in the 600 - 900 nm wavelength range. In addition to the CCD camera, the two high-speed photodiode systems described in Chapter 2 recorded the evolution of the light intensity in the 350 - 1100 nm wavelength range with a time resolution of 100 ns. Both instruments observed the impacts from above. The camera was positioned directly downrange of the oblique impact direction. The photodiode system was positioned uprange and slightly offset from the direction of impact (Figure 1). For one series of experiments, the camera viewed the impact through a side window.

The camera system captured a single image for each impact. In order to examine the evolution of the flash, separate impact experiments were performed with nearly identical parameters, while acquiring images at various time steps. Slight variations in impact velocity between experiments are unavoidable; however, these variations did not significantly affect the observations of interest for this study.

3. Source Temperature and Distribution

The impact flash intensity and projected source area can be measured directly from the camera images. Because the images are spatially resolved, higher intensity measurements imply higher-temperature materials. Intensity levels from the images were converted to temperatures through calibration with a Thermogauge dual cavity blackbody source located at NASA Ames Research Center's Sensor Calibration Laboratory (see Appendix).

3.1 Temperature and Source Area Observations

The camera captured the first moment of contact (< 50 ns), occurring before even the rise to the early-time spike, for a 45º Pyrex/pumice powder impact at 6.04 km/s (Figure 2a). The transparent projectile is totally illuminated by the high-temperature material being generated along the projectile/target interface. The source is brightest along the leading edge of the projectile. This light represents the initiation of the jetting component. This source is made up of very little mass. Its emissions are almost completely atomic emissions with little or no thermal contribution [*Sugita and Schultz*, 1999; *Schultz et al.*, 2006] and are very short-lived; thus, they do not contribute much to the impact flash signal. The temperature distribution of the image (Figure 2b) reveals elevated temperatures observed through the projectile. The maximum observed temperature along the leading edge appears to be 4380 K; however, because the source is not thermal the temperature is not necessarily realistic.

Figure 3a shows a 250 ns exposure of the flash taken at 5 μs for a 30º Pyrex/pumice powder impact. Also shown are maps of the intensity (b) and temperature (c). Most of the observed light emitted at this time comes from a small region near the impact point with a projected area of 1.8 ± 0.2 cm^2. The hottest material is located at the central portion of this region, where the average temperature is about 3350 ± 100 K with a maximum temperature, T_{max}, of 3450 ± 100 K. In the following discussion the error for all camera-derived temperature measurements is ± 100 K.

A large region of lower intensity and temperature (23.1 ± 0.2 cm^2) surrounds the central radiating region. It emits significantly less visible luminous energy due to its lower temperature (average ~ 2850 K). A 3400 K blackbody source emits 3.3 times more energy than the same source at 2800 K over the wavelength range observed by the camera (600 – 900 nm). A small concentration of material at slightly higher intensity and temperature lies along the direction of original trajectory within this large region. This feature will be addressed in Section 5.

Figure 4 contains an image (a), an intensity map (b), and a temperature map (c) of a comparable 30º impact taken at 20 μs. Between 5 μs and 20 μs the brightest central region has grown in size to 4.6 cm^2 but decreased in total emitted light by a factor of two. The T_{max} is 3200 K and the average temperature for the area is 3150 K. This image exhibits an interesting linear feature of lower intensity and temperature that bisects the main radiating source. This feature may be related to the downrange concentration of slightly hotter material seen at 5 μs (also addressed in Section 5).

3.2 Comparison of Camera and Photodiode Observations

The spatially integrated temperatures derived from the photodiode data of a 30º impact (Chapter 2) are directly compared to the camera-based temperature measurements (made at 5 and 20 μs) in Figure 5. The plotted camera temperatures are the T_{max} values measured for each image. The two sets of temperature values agree within the measurement error and both exhibit consistent decreases between 5 and 20 μs. The camera-based temperatures (T_{CCD}), however, are consistently lower than the corresponding photodiode-based temperatures (T_{PD}).

Figure 6 compares T_{CCD} to simultaneously measured T_{PD} for several impacts to assess whether the observed offset is systematic. While the two temperature measurements continue to match within the uncertainties, there is a common offset from a 1:1 relationship, with $T_{CCD} < T_{PD}$. This offset likely results from the use of different temperature calculation methods. For both instrument calibrations, a blackbody intensity source was assumed. In reality, the materials used are greybodies. At a given temperature a blackbody emits more light than a greybody due to its perfect emissivity, i.e., the estimated temperature for a greybody will be too low. Because the photodiode temperature calculation method uses intensity ratios, the calculated temperatures are not affected by the blackbody assumption. In contrast, the camera calibration method uses absolute intensity values, leading to T_{CCD} being an underestimation of the actual temperature.

Figure 7 compares the projected source areas directly measured in the images to the source areas derived from the multi-channel photodiode data. The two independently derived areas match within the error. This comparison confirms that the photodiode-derived source areas correspond to the central, hottest emitting source area observed in the images. It also validates the area measurements presented in Chapter 2.

3.3 Impact Angle Effects

Images of the flash taken at the same time after impact (20 μs) for different impact angles (90º, 60º, 45º, 30º, 15º) reveal differences in source distribution (Figure 8). The projected areas appear slightly foreshortened due to the perspective generated by the off-vertical camera location. The source bisection is again observed for the 45º and 30º impacts (and to a lesser extent for the 15º impact). The aspect ratio (along-trajectory/cross-trajectory) of the primary emitting source area increases with decreasing angle from 60º to 15º (Figure 9). This relation to the shape of the radiating source is not observed at higher angles; between 60º and 90º, the aspect ratio remains constant and close to one (source is roughly circular). The foreshortening is accounted for in the aspect ratio measurements. The source size at 20 μs exceeds the projectile size by a factor of 4 – 15 (depending on the angle).

3.4 Later-time Source Region

After reaching maxima, the radiating source intensity and temperature both steadily decrease. Images taken 20 μs (a) and 50 μs (b) after impact reveal that the location of the radiating source does not change over this time (Figure 10). The difference in impact speed (5.49 km/s in Figure 10a versus 4.25 km/s in Figure 10b) affects absolute values of intensity and temperature but not the spatial evolution. The lingering source is fully within the transient crater. Consequently, cooling must control the observed intensity decrease, rather than significant expansion or thermal sources leaving the field of view.

3.5 Low-velocity Impacts

Observations thus far have assessed emission generated by impacts ranging in velocity from 4.25 to 6.04 km/s. At these velocities, the impact flash arises from hot material heated largely through shock effects and the radiating source temperatures are high enough to produce significant visible light. Chapter 1 showed that the magnitude of the impact flash for impacts at 5 km/s differs from the flash at 2 km/s. For faster impacts, the secondary rise dominates the observed signal and corresponds to the maximum intensity. In contrast, the maximum intensity for the lower velocity impacts corresponds to the early-time spike. Higher speeds produce both higher temperatures and greater amounts of melt and heated material that create a significantly delayed intensity peak.

Figure 11a shows the first 50 μs of the photodiode light curve for an impact at 1.9 km/s at an impact angle of 60º. The light curve out to 200 μs is shown in the upper right corner for context. The features of the light curve include an early-time spike, a subsequent rise to a broad, secondary intensity peak, and the gradual decay of the light intensity (previously described in Chapter 1). Because these impacts occurred at low speeds, the early-time spike feature becomes the brightest portion of the intensity curve when time resolved. Figure 11b is an integrated time exposure of the first 1 ms of the impact flash. Because of the long exposure time, much of the image is saturated.

The colored areas under the light curve correspond to the timing of the camera images (Figure 11 A-F), which span the first 22 μs after impact (Figure 12). The sequence in Figure 12 represents images taken during six impacts with velocities from 1.6 – 1.9 km/s. The highest intensity source region occurred between 0 - 3 μs (image A). Image A encompasses the entire early-time spike feature, resulting from the first contact between the projectile and the target (Chapter 1). This image corresponds to the time of highest absolute intensity for this series of low velocity, 60º impacts, consistent with this being the time of both peak temperature [*Kadono and Fujiwara*, 1996] and stress [*Dahl and Schultz*, 2001]. Because of the relatively long exposure times needed to record the flash source at low velocities, the maximum temperatures for most of these images cannot be determined due to saturation.

The subsequent rise and arrival at the secondary intensity peak (Figure 11) is covered by images B - E. There is a well-defined arc of maximum relative brightness, corresponding to the maximum temperature. This bright arc moves at a speed consistent with the horizontal projected motion of the penetrating projectile. The measured temperatures of this arc range from 2600 – 2800 K. By the time of the final exposure (image F, 17 μs after impact), the distinct intensity arc has dispersed. At this time, the impact flash has reached its decay stage (Figure 11a).

An (opaque) aluminum projectile was used to assess the possible effect of projectile transparency on the resulting flash intensity. Figure 13 compares 2 μs exposures of Pyrex and aluminum projectile impacts taken at similar times after impact (7 μs and 8 μs, respectively), well after the initial spike. The impacts occurred at a 60º and ~1.9 km/s. The mass of the aluminum projectile was greater than that of the Pyrex projectile (0.3758 g versus 0.2986 g), but the specific kinetic energies of the two impacts were comparable. The corresponding photodiode light curves are shown in Figure 14. The early-time intensity evolutions of Pyrex and aluminum impacts exhibit very different characteristics (Figure 14). The early-time spike feature is absent in the aluminum impact flash signal. Moreover, the broad peak is much lower, and the rise to this peak is very different. By 45 – 50 μs, the intensity level and evolution of the two impact flashes are the same. Structure can be seen in the radiating material for the opaque impactor with a maximum temperature of about 2200 K. While some saturation occurs in the Pyrex impact image, observable temperatures reach 2700 - 2800 K. The arc of heated material, however, is not observed for the aluminum impact.

4. Effect of Porosity and Vaporization

The evolution of the flash changes significantly with initial conditions. Higher velocities (5-6 km/s), oblique impact angles, and projectile failure all affect the characteristics of the observed impact flash. An additional variable is target material. Three impacts were performed to observe the effect of target properties for otherwise identical impact conditions (Figure 15). Pumice powder provides a reference (Figure 15a) for the effects of highly porous (Figure 15b) and easily vaporized materials (Figure 15c). A layer of perlite (one projectile diameter thick) is used to assess target porosity. Dolomite is used to assess the effect of vaporization.

The effect of a highly-porous surface layer on the spatial distribution of the impact flash using the combined image and photodiode datasets is discussed in Chapter 4 [*Ernst and Schultz*, 2007a]; however, the temperature and the distribution of radiating material provide further insight for controlling processes. As described in Section 3, the radiating source for a pumice powder impact is centrally located. The T_{max} is 3200 K, and the general shape of the source is elongated along-trajectory. When the thin porous layer is added, the source distribution changes significantly. The T_{max} remains the same, but it is confined to a much smaller projected area. The bright spot downrange of the impact point is likely the result of downrange projectile fragments interacting with the surface. A portion of the radiating material is directed uprange of the impact point. This uprange plume is caused by the deeper penetration of the projectile into the more porous material [*Ernst and Schultz*, 2007a; *Schultz et al.*, 2007; *Schultz et al.*, 2005]. The temperature of this uprange plume is 2700 – 2800 K.

Previous laboratory experiments described the impact-generated vaporization of dolomite targets [*Schultz*, 1996; *Sugita et al.*, 1998; *Schultz et al.*, 2006]. The shape of the impact-generated source region for dolomite contrasts with the source region for both the pumice powder and layered targets. For the dolomite impact, the source covers a much broader area than that generated for pumice. The emitting source greatly exceeds the diameter of the transient crater and must be located above the target surface. This is consistent with previous studies of impacts into dolomite that observed vapor plumes expanding above the surface while moving downrange [*Schultz*, 1996; *Schultz et al.*, 2007]. Two packets of enhanced temperatures appear within the downrange vapor plume. The splitting of this source may be related to the bisection feature noted for pumice powder (Figures 4 and 7).

Interpretations of temperature measurements of vapor sources can become complicated if strong molecular emission bands contribute significantly to the observed intensity. Vapor from dolomite exhibits prominent CaO and Ca emission bands in the wavelength range examined; however, these bands are primarily produced during the first 2 μs of the impact and a thermal source is also observed [*Sugita et al.*, 1998]; therefore, the calculated temperatures at 20 μs should be fairly representative of the actual temperature of a thermal source. Here, the radiating sources (heated particulates, condensates) are entrained in a vapor plume and thus transported above the transient crater and downrange. The observed T_{max} is 2900 K for the impact into dolomite is cooler than the T_{max} observed for both the pumice powder and the layered impacts. The lower temperature could be caused by the loss of heat at the melt/vapor phase transition.

The differences in source distribution and temperature can be compared to the temporally resolved light curves observed by the photodiode (Figure 17). The addition of the porous layer to the pumice powder target results in an overall reduction of the flash light output and a delay in the timing of the peak signal. The dolomite target produces a flash drastically reduced in overall brightness and duration.

Figure 18 provides a side view for a 60º impact of a Pyrex projectile into a dolomite target over the first 5 μs. The side view impact was performed in a quarterspace setup [*Piekutowski*, 1977; *Schultz et al.*, 2005]. The quarterspace is formed by impacting near the edge of a clear acrylic window paralleling the impact direction. The area at and below the target surface was masked so that the sub-surface signal could not be observed (including the inside of the transient crater). This setup permits a cross-sectional view of the evolving thermal plume. The acrylic glass may cause boundary effects; this is an area for future investigation. No scouring of the acrylic window was observed during post-impact examination. Also, no thermal trail is observed in the images; thus, there should not be a significant intensity enhancement caused by the presence of the window.

The images reveal the evolution at 1, 2.5, and 5 μs after impact displayed at different intensity scales to optimize visualization of the vapor plume structure (Figure 18). A packet of concentrated hotter material occurs in the center of the vapor plume that can be tracked through the three images, similar to the later-time view from above (20 μs,

Figure 16c). This observation clearly demonstrates that the concentration of highest intensity (and thus temperature) material occurs above the target surface for the dolomite impact. The intensity and temperature both decrease through time. The vapor front can be clearly seen, most prominently at 5 μs. The higher intensity of the front may be due to a concentration of entrained particles [*Kadono and Fujiwara*, 1996] or condensates [*Schultz et al.*, 2007] in the vapor front.

5. Discussion

The temperature and source area measurements made by the photodiode are comparable with those observed by the camera, with the integrated temperature corresponding best with the hottest temperature zone. The photodiode measurements, therefore, are fairly representative of the impact flash, despite being spatially integrated.

5.1 Source Distribution

At early times (20 μs), the shape of the radiating source for Pyrex/pumice powder impacts is greatly affected by the impact angle. The observed relationship between aspect ratio and angle does not follow a simple $\sin\theta$ (or $\cos\theta$) relationship related to the projected size of the projectile "footprint". The observed relationship also does not follow a $\sin^2\theta$ relationship, which would be expected for a dependence on peak pressure [*Schultz*, 1996] and has been used to describe the volume of melting during an impact for theoretical studies [*Pierazzo and Melosh*, 2000]. Instead, the observed source shape at this time may reflect a combination of the projected shape of the developing transient crater, the areal spread and depth of the emitting source, and the evolving redistribution of thermal sources along the wall and floor of the transient cavity, which is distributed farther downrange for more oblique impacts.

The bisection in the radiating source characterizes the source appearance for low-angle impacts where the projectile energy is well coupled to the target. At 15º, much of the original kinetic energy is retained by the projectile [*Schultz and Gault*, 1990a] and the bisection is not observed. The hottest portion of the 45º, 30º source is split to either side of the center. This feature appears to be related to the downrange extension of the radiating area seen in Figure 3. A possible cause is the failure style of the Pyrex projectile, which is related to the contact between the projectile and the target [*Schultz and Gault*, 1990b; *Schultz et al.*, 2006]. This process is revealed in Figure 10b where the highest temperatures 50 μs after impact correspond to regions related to projectile failure. The bisection should not be observed at 60º or higher angles due to the downward projectile trajectory and containment of material within the transient crater.

This feature was not observed for the impact into the porous layered target. The reduced peak pressure in the projectile delays projectile failure, and most of the radiating source is driven into a deeper transient crater. Therefore, the projectile failure is better-contained and hidden from view. The bisection, however, is observed for the impact into dolomite, just in a different form. There are two packets of hotter material observed. For this impact the packets are located farther downrange than the split source of the pumice powder impact, consistent with projectile failure patterns observed for other targets. This is likely due to its location above the surface and additional distance due to being vapor-driven [*Wrobel et al.*, 2004].

5.2 Source Origin

Based on the low-velocity experiments described in Section 3.4, the main source of the early-time impact flash is likely produced along the projectile/target interface where the most intense pressure and temperature conditions, highest strain rate, and shear heating occur. Hot material is left along the forming crater base along the path of the projectile as it advanced into the target. In the time-exposed image (Figure 11b), the region of highest intensity corresponds to illuminated projectile and the smeared projectile/target contact. It is observable primarily due to the transparency of the Pyrex projectile.

For Pyrex, the early-time spike represents the first contact between the projectile and target. At these low velocities, the secondary intensity peak represents the continued contact between the projectile and target, which is easily observable due to the transparency of the projectile. The spike and secondary peak are not observed for impacts by aluminum projectiles. Even at 2 km/s, Pyrex projectiles fail on impact, thereby creating numerous free surfaces with elevated temperatures. At this velocity, however, recovered aluminum projectiles reveal that they abrade only on one side. Such differences in projectile failure and transparency contribute to the differences in the light curves.

The intensity level and evolution of the two impact flashes are the same at later times (45 – 50 μs). This is to be expected since the total amount of transferred energy should be approximately the same for these two impacts. By this time, cooling of the emergent heated target material controls the signal, independent of projectile opacity.

Consequently, the use of a transparent projectile exposes conditions along the projectile/target interface that otherwise could not be observed.

6. Conclusions

Short-exposure images provide new perspectives and insight to the spatial distribution of the evolving impact flash. These observations also permit the measurement of temperatures. The combination of these images with time-resolved photodiode light curves allows the characterization of the impact flash source area and the contributing processes.

The temperature and source area values measured from the images are consistent with those observed and calculated using the photodiode systems used extensively in Chapters 1 and 2. The effect of impact angle can be directly measured from the images. The primary radiating source for the Pyrex impacts into pumice powder targets lines the walls and floor of the transient crater cavity. New phenomena have been observed for the first time, such as the bisection of the thermal source observed at lower angles. Further experimental studies will be able to characterize this feature and its relation to projectile failure.

Under the examined impact conditions, the early-time flash source, including the spike, originates along the interface between the penetrating projectile and the target. Its visibility is greatly enhanced due to the transparency of the projectile. Low-velocity impacts by opaque projectiles demonstrate that the contact surface contributes to the impact flash. When viewed from above, the flash emerges from behind the projectile. When viewed from the side, the flash is hidden below the surface.

The addition of porosity and volatiles to a target surface drastically changes the distribution of heated material at a given time. The maximum observed temperatures for highly porous targets remain similar to those for pumice, but much of the material is confined into a deeper transient crater, thereby hiding the radiating source region. A small amount of material is ejected uprange of the impact point. For impact-vaporized targets, the radiating source is dispersed above the target surface and entrained in a vapor plume, instead of primarily lining the transient crater cavity. Phase changes absorb some of the energy and uncondensed vapor emit light over limited wavelengths. The combination of all these processes significantly reduces the intensity of the impact flash.

Acknowledgements

The authors would like to thank the NASA Ames Vertical Gun Range crew (D. Holt, R. Smythe, D. Bowling, and C. Cornelison) for their assistance and technical prowess. Special thanks are afforded to M. Wilder at Ames Research Center for his cooperation and assistance. This research was supported by NASA grant No. NAGS-11538 and the NASA Graduate Student Researchers Program (04-6011H).

References

Dahl, J. M., and P. H. Schultz (2001), Measurement of stress wave asymmetries in hypervelocity projectile impact experiments, *International Journal of Impact Engineering*, *26*, 145-155.

Eichhorn, G. (1976), Analysis of the hypervelocity impact process from impact flash measurements, *Planetary and Space Sciences*, *24*, 771-781.

Ernst, C. M., and P. H. Schultz (2002), Effect of velocity and angle on light intensity generated by hypervelocity impacts, *LPSC*, *XXXIII*, #1782.

Ernst, C. M., and P. H. Schultz (2003), Effect of initial conditions on impact flash decay, *LPSC*, *XXXIV*, #2020.

Ernst, C. M., and P. H. Schultz (2007a), Evolution of the Deep Impact flash: Implications for the nucleus surface based on laboratory experiments, *Icarus*, *190*, 334-344.

Ernst, C. M., and P. H. Schultz (2007b), Temporal and spatial resolution of the early-time impact flash: Implications for light source distribution, *LPSC*, *38*, #2353.

Gehring, J. W., and R. L. Warnica (1963), An investigation of the phenomena of impact flash and its potential use as a hit detection and target discrimination technique, *6th Symposium on Hypervelocity Impact*, 627-681.

Gilbert, G. K. (1893), The Moon's face, *Bull. Philos. Soc. Wash.*, *12*, 241-292.

Jean, B., and T. L. Rollins (1970), Radiation from hypervelocity impact generated plasma, *American Institute of Aeronautics and Astronautics Journal*, *8*, 1742-1748.

Kadono, T., and A. Fujiwara (1996), Observation of expanding vapor cloud generated by hypervelocity impact, *Journal of Geophysical Research*, *101*(E11), 26,097-26,109.

Piekutowski, A. J. (1977), Cratering mechanisms observed in laboratory-scale high-explosive experiments, in *Impact and Explosion Cratering: Overviews*, edited by Roddy, D. J., R. O. Pepin and R. B. Merrill, pp. 67-102, Pergamon Press, New York.

Pierazzo, E., and H. J. Melosh (2000), Melt production in oblique impacts, *Icarus*, *145*, 252-261.

Schultz, P. H., and D. E. Gault (1990a), Prolonged global catastrophes from oblique impacts, in *Global Catastrophes in Earth History: An Interdisciplinary Conference on Impacts, Volcanism, and Mass Mortality*, edited by Sharpton, V. L. and P. D. Ward, pp. 239-261, Special Paper of the Geological Society of America.

Schultz, P. H., and D. E. Gault (1990b), Prolonged global catastrophes from oblique impacts, in *Global Catastrophes in Earth History: An Interdisiplinary Conference on Impacts, Volcanism, and Mass Mortality*, edited by Sharpton, V. L. and P. D. Ward, pp. 239-261, Special Paper of the Geological Society of America.

Schultz, P. H. (1996), Effect of impact angle on vaporization, *Journal of Geophysical Research*, *101*(E9), 21,117-21,136.

Schultz, P. H., C. M. Ernst, and J. L. B. Anderson (2005), Expectations for crater size and photometric evolution from the Deep Impact collision, *Space Science Reviews*, *117*, 207-239.

Schultz, P. H., S. Sugita, C. A. Eberhardy, and C. M. Ernst (2006), The role of ricochet in impact vaporization, *International Journal of Impact Engineering*, *33*, 771-780.

Schultz, P. H., C. A. Eberhardy, C. M. Ernst, M. F. A'Hearn, J. M. Sunshine, and C. M. Lisse (2007), The Deep Impact oblique impact cratering experiment, *Icarus*, *190*, 295-333.

Shoemaker, E. M. (1962), Interpretation of lunar craters, in *Physics and Astronomy of the Moon*, edited by Kopal, Z., pp. 283-359, Academic Press, San Diego.

Sugita, S., P. H. Schultz, and M. A. Adams (1998), Spectroscopic Measurements of Vapor Clouds Due to Oblique Impacts, *Journal of Geophysical Research*, *103*(E8), 19,427-19,441.

Sugita, S., and P. H. Schultz (1999), Spectroscopic characterization of hypervelocity jetting: Comparison with a standard theory, *Journal of Geophysical Research*, *104*(E12), 30,825-30,845.

Wrobel, K. E., P. H. Schultz, and J. T. Heineck (2004), Non-Ballistic Vapor-Driven Ejecta, *LPSC*, *XXXV*, #1800.

Table 1. Experimental target properties: composition, bulk density (ρ_b), particle density (ρ_p), and porosity

Target	Composition	ρ_b (g cm^{-3})	ρ_p (g cm^{-3})	Porosity
pumice powder	rhyolitic (> 70% SiO_2)	1.25	2.20	0.43
sieved perlite granules	rhyolitic	0.22	2.20	0.90
dolomite powder	$CaMg(CO_3)_2$	1.33	2.85	0.53

Figure Captions

Figure 1. Side and top view sketches of the instrument configuration at the AVGR. The CCD camera was located above and downrange of the impact point, in line with the projectile trajectory and elevated 75º from horizontal (CCD top). The photodiode systems were located above and uprange of the impact point, also elevated 75º from horizontal (PD). The side view camera position is located perpendicular to the projectile trajectory (CCD side). The grey ports with white circles represent window ports and the grey ports with black circles represent projectile entrance ports (each separated by 15º). The target is located at the center of the vacuum chamber on an elevated platform.

Figure 2. Image (a) and temperature (b) of the moment of first contact between a 4.76 mm-Pyrex projectile and a pumice powder target at 45º and 6.04 km/s. The image is an extremely short, 50 ns exposure started at $t = 0$. The bright leading edge likely represents the jetting component, which consists of a very small mass of material at very high temperatures. Its emissions are almost completely atomic emissions with little or no thermal contribution. The high-temperature material being generated at the projectile/target interface illuminates the entire transparent projectile. The projected direction of impact is from the top of the image.

Figure 3. Image (a), intensity map (b), and temperature map (c) of the flash taken 5 μs after an impact of a 6.35 mm-Pyrex projectile with a pumice powder target at 30º and 5.79 km/s. This is a 250 ns exposure. The impact point is indicated by a 'plus' symbol (+). The highest-temperature material is located in a small, central region near this point. The direction of impact is from the top of the image. The maximum observed temperature is 3450 K.

Figure 4. Image (a), intensity map (b), and temperature map (c) of the flash taken 20 μs after the impact of a 6.35 mm-Pyrex projectile with a pumice powder target at 30º and 5.52 km/s. This is a 250 ns exposure. Between 5 μs and 20 μs the brightest central region has grown in size decreased in total emitted light and temperature (see Figure 3). The impact point is indicated by a 'plus' symbol (+). The direction of impact is from the top of the image. The maximum temperature in the image is 3200 K. The main source is bisected by a region of lower intensity and temperature material.

Figure 5. Comparison of the temperatures measured by the photodiode system and the camera for a 30º, 6.35 mm-Pyrex/pumice powder impact at 5.52 km/s. The gray band around the photodiode-derived temperature evolution represents the ± 200 K error. The closed circles represent the maximum temperature measured by the camera at 5 μs and 20 μs (see Figures 3c and 4c). The two temperature sets match within the error; however, the photodiode-derived temperatures are higher in both cases.

Figure 6. Comparison between the temperatures simultaneously measured by the photodiode system and the camera for several impacts. The solid line through the center of the plot is a 1:1 relationship. The photodiode temperatures are consistently higher than

the maximum camera temperatures. There is a common offset, as the data fall along a line of parallel slope. This offset is likely a result of different calibration methods and the assumption of a blackbody source.

Figure 7. Comparison between the source areas calculated from the photodiode system and measured from camera images for a 30º, 6.35 mm-Pyrex/pumice powder impact at 5.52 km/s. The closed squares represent the source area measured from the images at 5 μs and 20 μs. The source areas match within the error.

Figure 8. Images of the radiating source taken 20 μs after impacts at 90º (4.62, a), 60º (4.94 km/s, b), 45º (5.54 km/s, c), 30º (5.52 km/s, d) and 15º (5.49 km/s, e) angles (and velocities). These images are displayed on different intensity scales in order to best display the source area. All projectiles were 6.35 mm-Pyrex spheres except for the 45º angle impact (4.76 mm). The 30º impact exhibits the largest projected source area. The source bisection is observed at 45º and 30º (and to a lesser extent at 15º). The images are all 50 ns exposures. The impact point is indicated by 'plus' symbols (+) and the direction of impact is from the top of the image (b – e) except for the vertical case (a). Due to the off-vertical location of the camera, the images are slightly foreshortened.

Figure 9. Aspect ratio (along-trajectory/cross-trajectory) of the projected radiating source area measured 20 μs after for impacts at 90º to 15º angles. The ratio is close to one (source is roughly circular) for 90º and 60º impacts. A change occurs between 60º and 45º as the aspect ratio begins to increase with decreasing angle. This trend holds through 15º. The foreshortening is accounted for in the measurements.

Figure 10. Comparison of the source location at 20 μs and 50 μs for 15º impacts shown on a temperature scale. A significant difference in impact speed, 5.49 km/s (a) versus 4.25 km/s (b), affects absolute values of intensity and temperature but not the location of the radiating source. The impact point is indicated by a 'plus' symbol (+). The direction of impact is from the top of the image. At the later time, the remaining heated material is primarily located inside of the crater.

Figure 11. (a) The location of the six short-exposure camera images (A-F) with respect to the photodiode light curve. The light curve out to 200 μs is shown for context, with the shaded region corresponding to the duration depicted in the main graph. (b) An intensity image of the impact flash integrated over the entire signal (0 – 1 ms). The central region of the image is completely saturated.

Figure 12. A composite time series representing the intensity of the impact flash intensity for a Pyrex projectile impact into pumice powder at 60º with a velocity between 1.6 and 1.9 km/s. The exposure times are noted in the corner of each image.

Figure 13. Comparison of the radiating source generated during Pyrex (px) and aluminum (al) projectile impacts into pumice powder at 60º and ~1.9 km/s. The 2 μs exposures were taken 7 and 8 μs after impact, respectively. A bright arc of material can

be seen for the Pyrex impact. The source distribution is very different for the aluminum impact. The flash intensity (and thus temperature) is significantly lower.

Figure 14. Comparison of the light curves for the impacts described in Figure 13. The shaded region corresponds to the timing of the camera images. The early-time spike feature is absent in the aluminum impact flash signal. Moreover, the broad peak is much lower, and the rise to this peak is very different. By 45 – 50 μs, the two signals have reached comparable levels.

Figure 15. Side views sketches of the experimental setup for the impacts displayed in Figure 16 (not drawn to scale). Pumice powder provides a reference (a) for the effects of highly porous (b) and easily vaporized materials (c). A layer of perlite (one projectile diameter thick) is used to assess target porosity. Dolomite is used to assess the effect of vaporization.

Figure 16. The effects of target porosity and vaporization on the intensity (I), temperature (T), and spatial distribution of the impact flash. The images are 250 ns exposures taken at 20 μs for 30º impacts into (a) pumice powder, (b) a projectile-thick layer of perlite over pumice powder, and (c) dolomite powder. The dashed line overlaying the upper images represents the uprange/downrange location of the impact point. All three impacts exhibit very different source distributions. For the pumice and dolomite powders, the observed radiating source is located entirely downrange of the impact point. An uprange plume is observed for the perlite impact. The maximum temperatures of the pumice and perlite targets are comparable (~3200 K), though the hot source is smaller in area for the perlite impact. For the dolomite impact, the source covers a much broader area than that generated for pumice, and the maximum temperature is lower (~2900 K). The emitting source greatly exceeds the diameter of the transient crater. The bisection of the source noted for pumice powder is also observed here.

Figure 17. The first 500 μs of the light intensity curves recorded by the photodiode for the impacts displayed in Figure 16. All three signals have distinct evolutions. There is a brief intensity delay in the rise to the intensity peak for the perlite impact. The dolomite target produces a flash drastically reduced in overall brightness and duration.

Figure 18. Side view images taken 1, 2.5, and 5 μs after 60º impacts into a dolomite quarterspace targets at velocities ranging from 5.6 to 6.0 km/s. The images are displayed on different intensity scales to highlight the source structure and distribution for all cases. The intensity and temperature both decrease through time. A packet of concentrated hotter material occurs in the center of the vapor plume that can be tracked through the three images, similar to the later-time view from above (20 μs, Figure 16c). This observation clearly demonstrates that the highest temperature packet is located above the target surface. The vapor front can be clearly seen, most prominently at 5 μs.

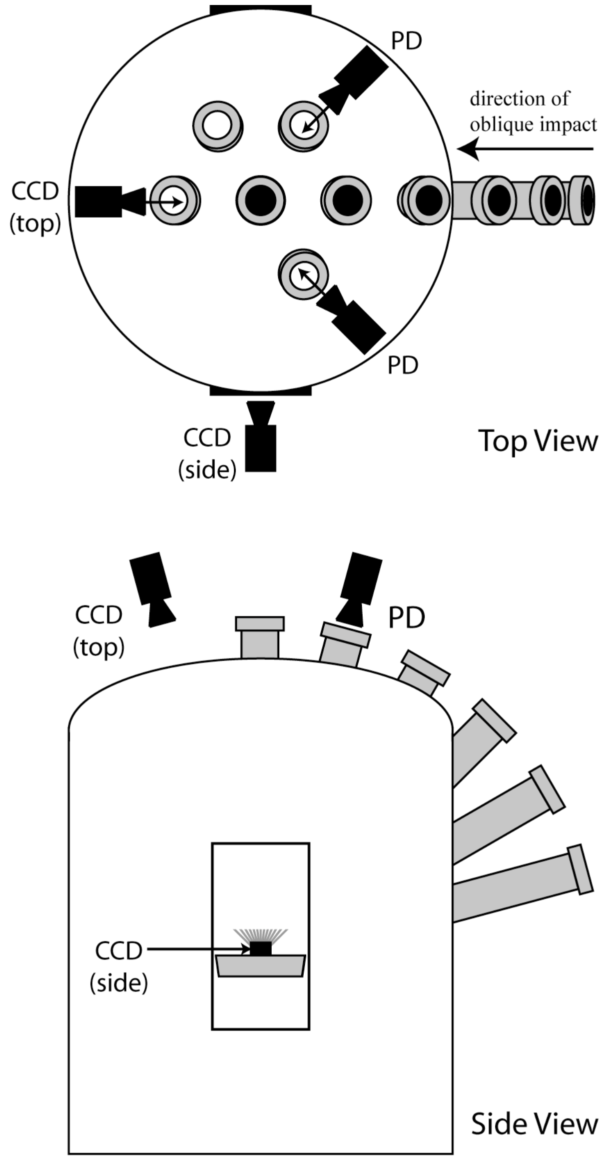

Chapter 3, Figure 1

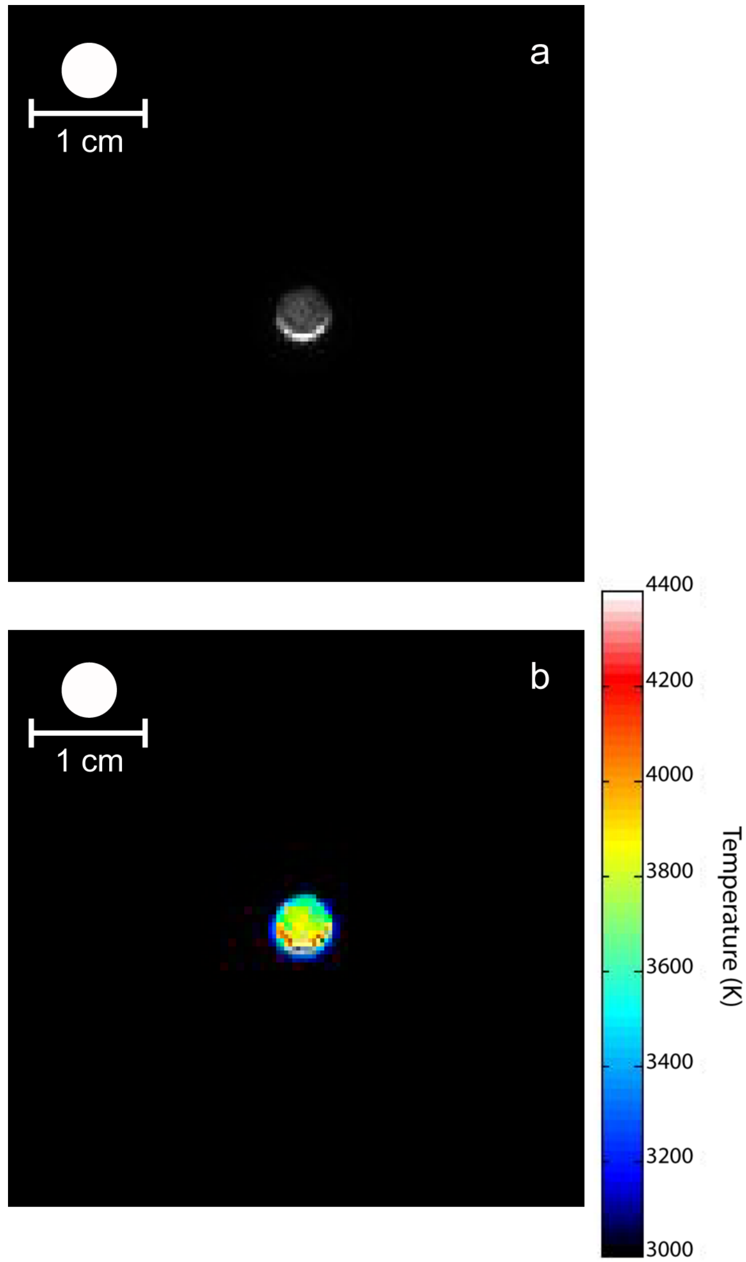

Chapter 3, Figure 2

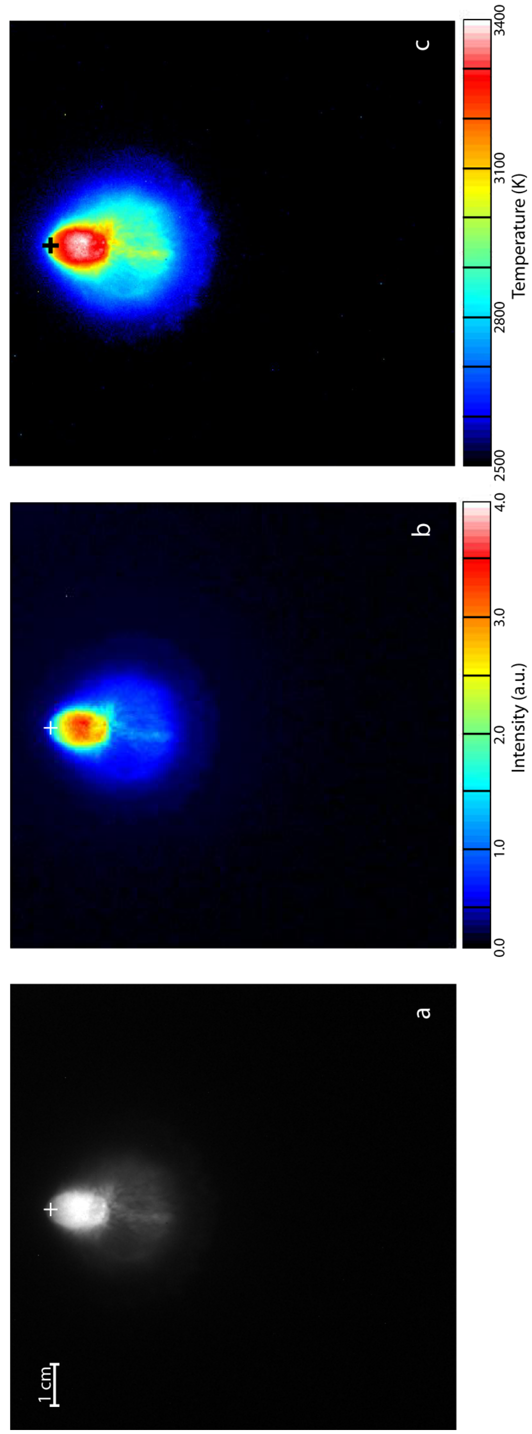

Chapter 3, Figure 3

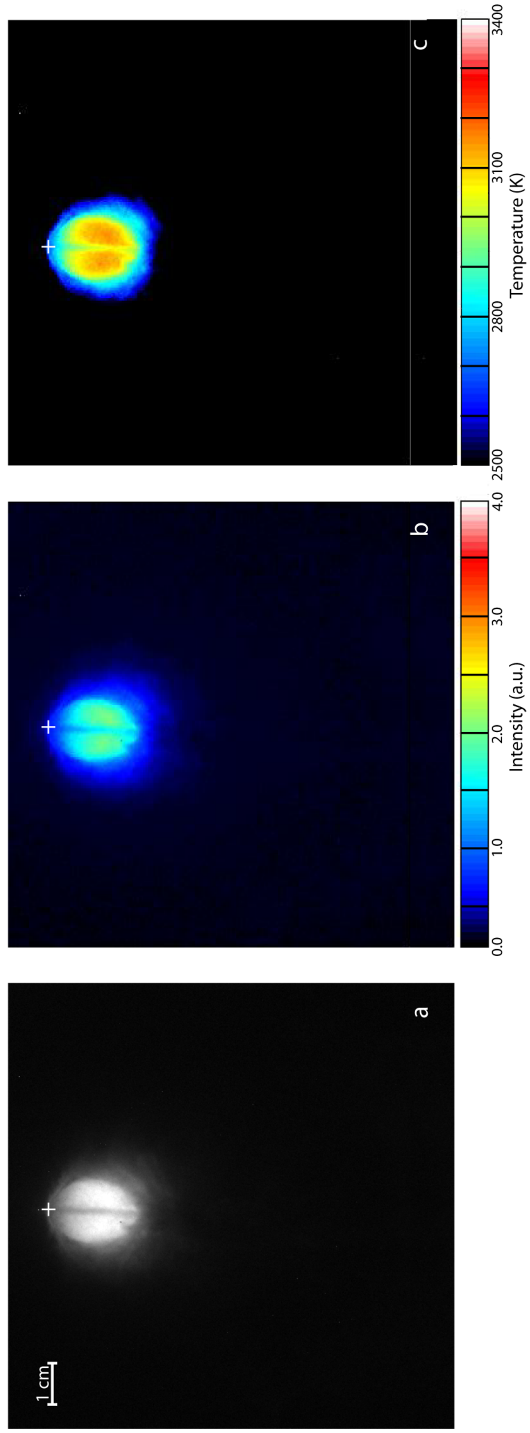

Chapter 3, Figure 4

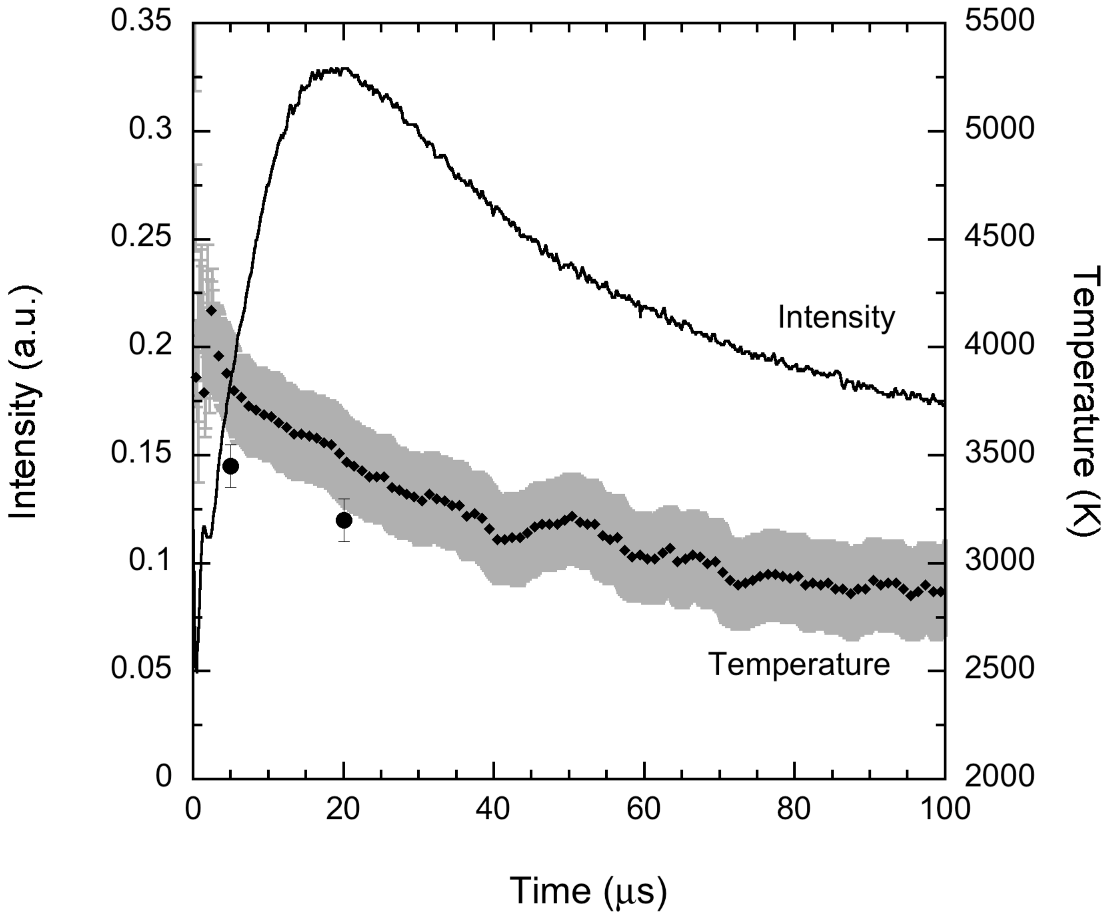

Chapter 3, Figure 5

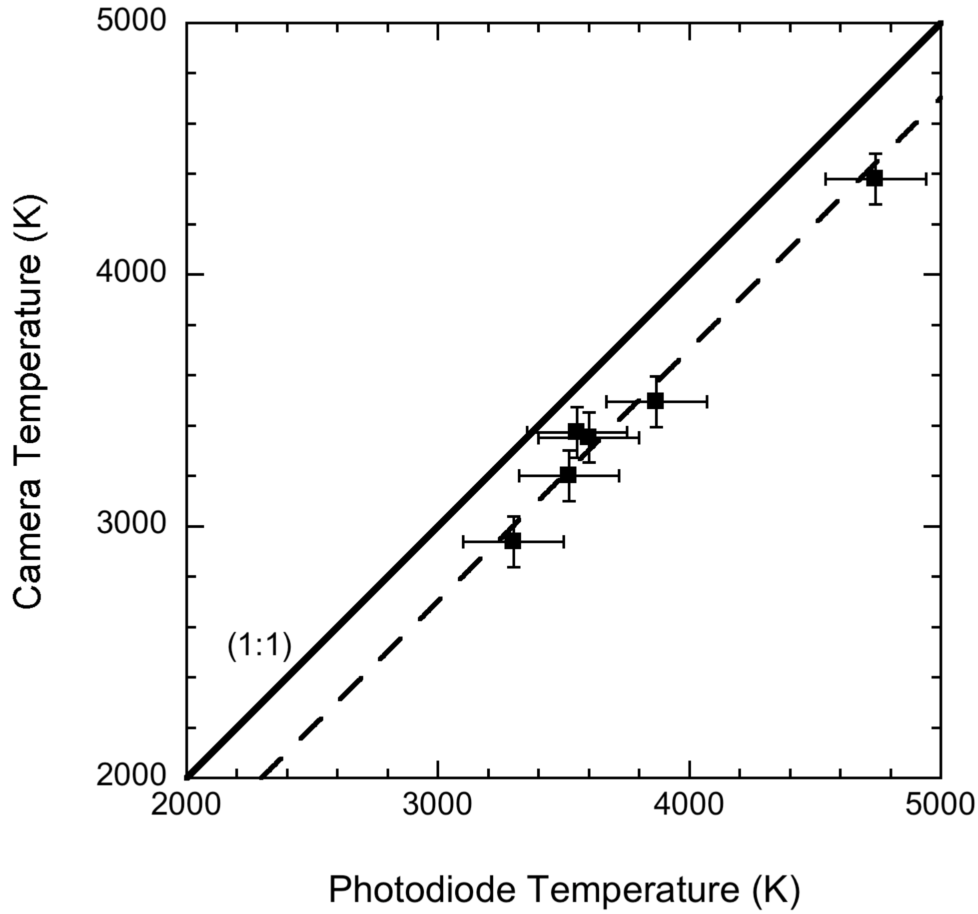

Chapter 3, Figure 6

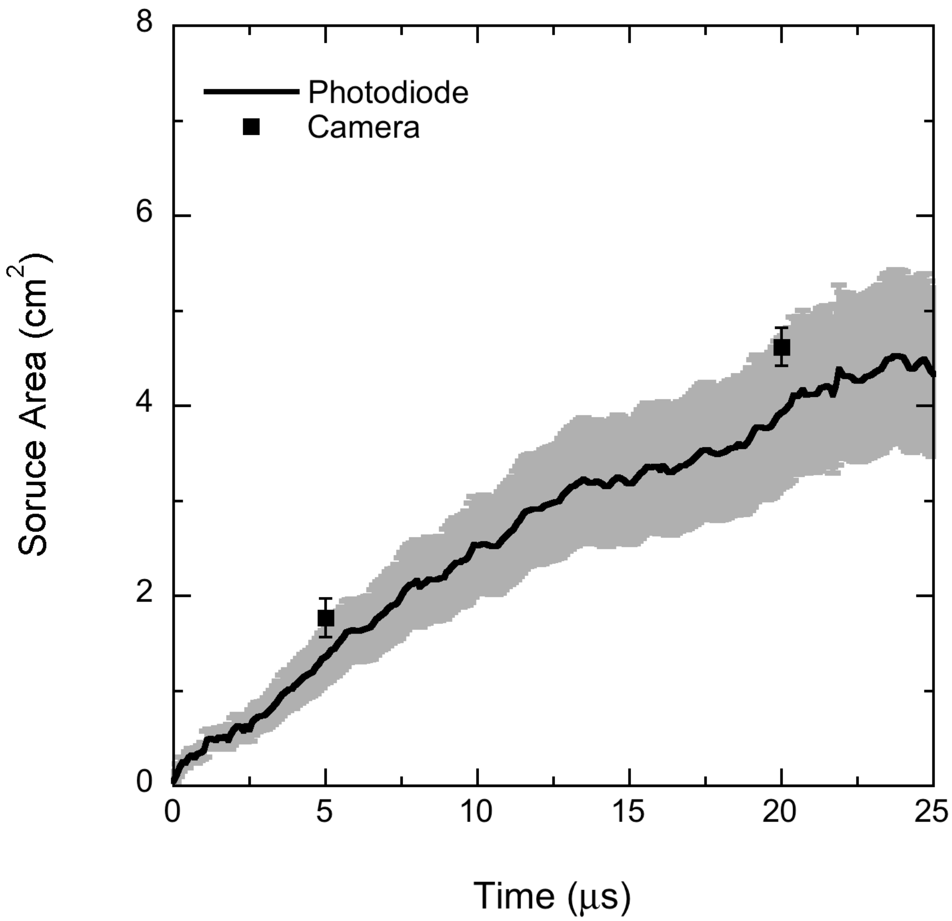

Chapter 3, Figure 7

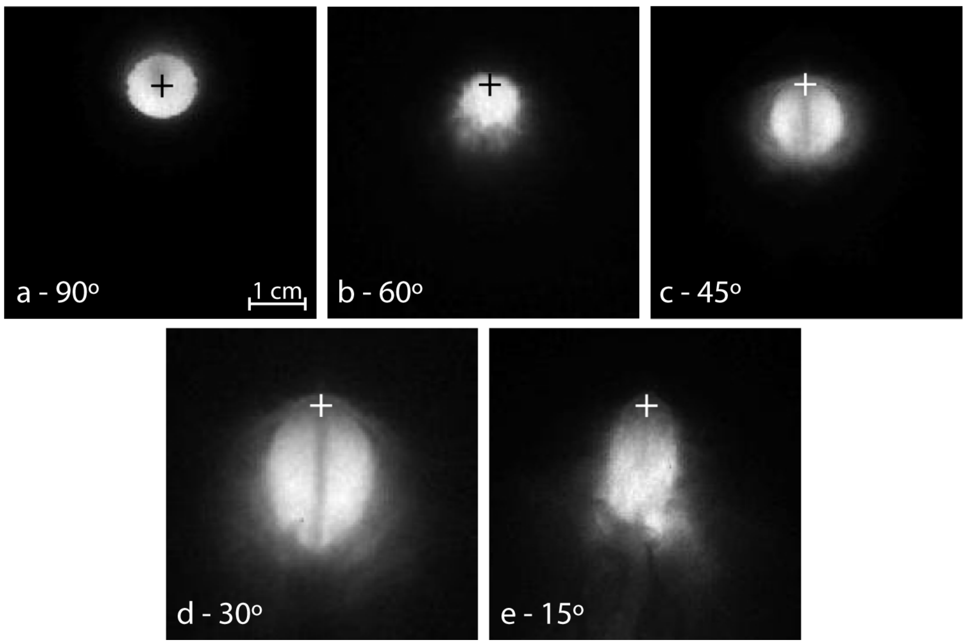

Chapter 3, Figure 8

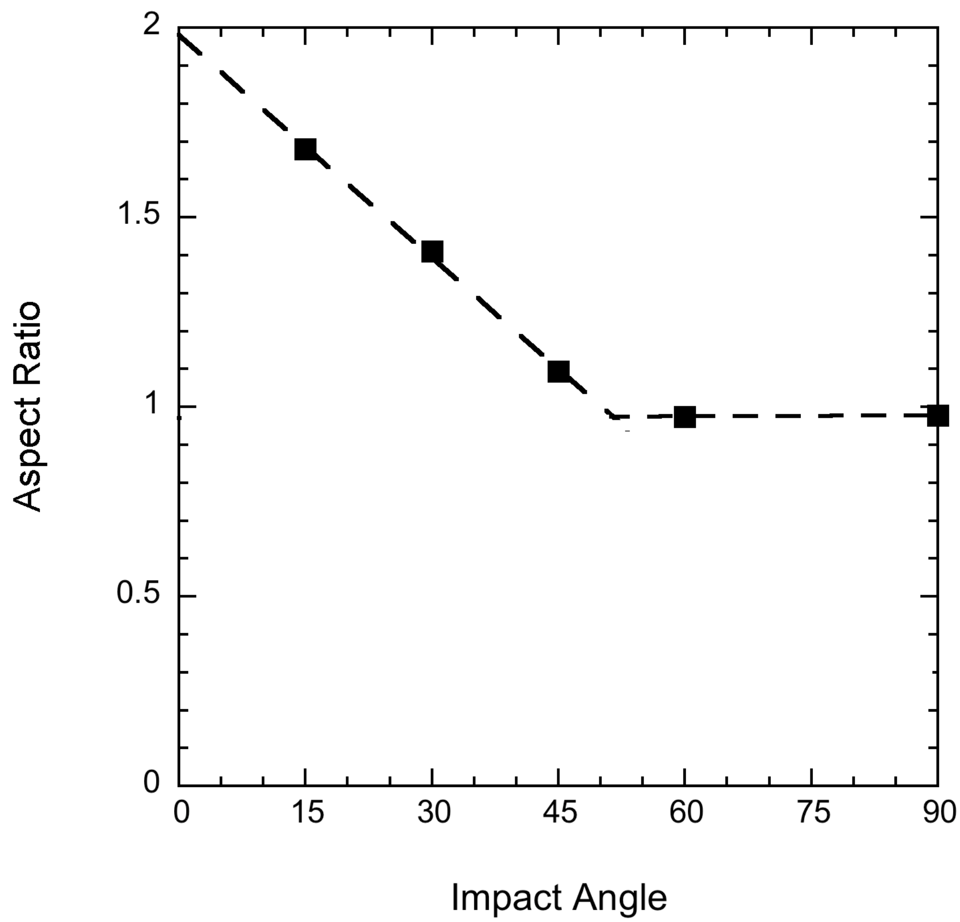

Chapter 3, Figure 9

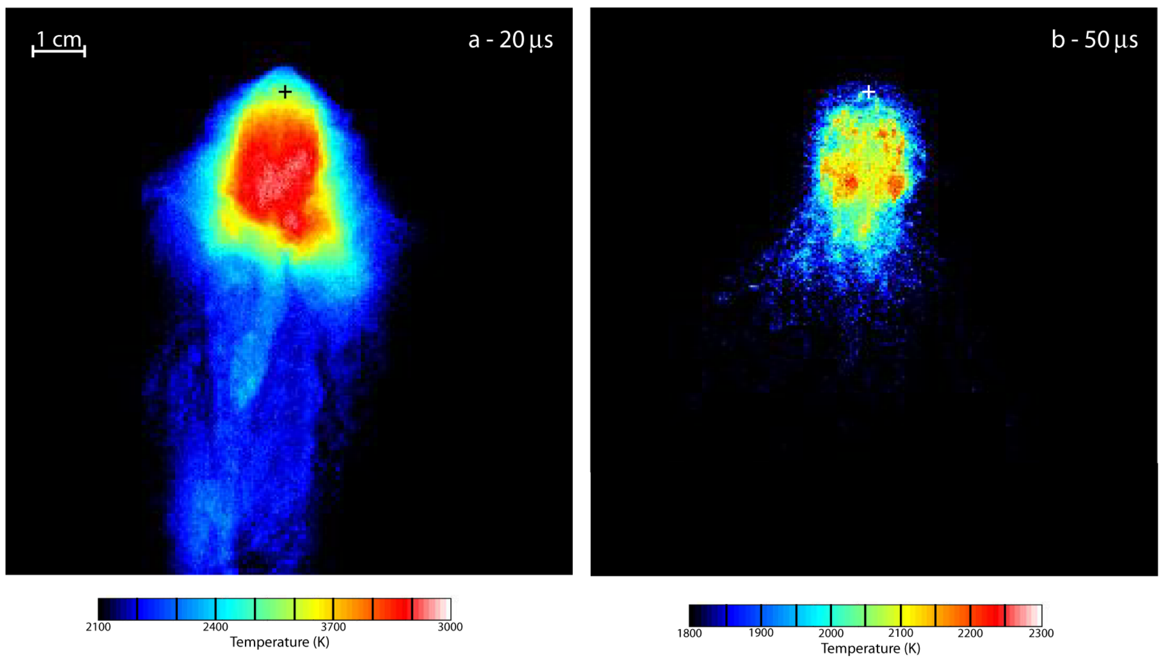

Chapter 3, Figure 10

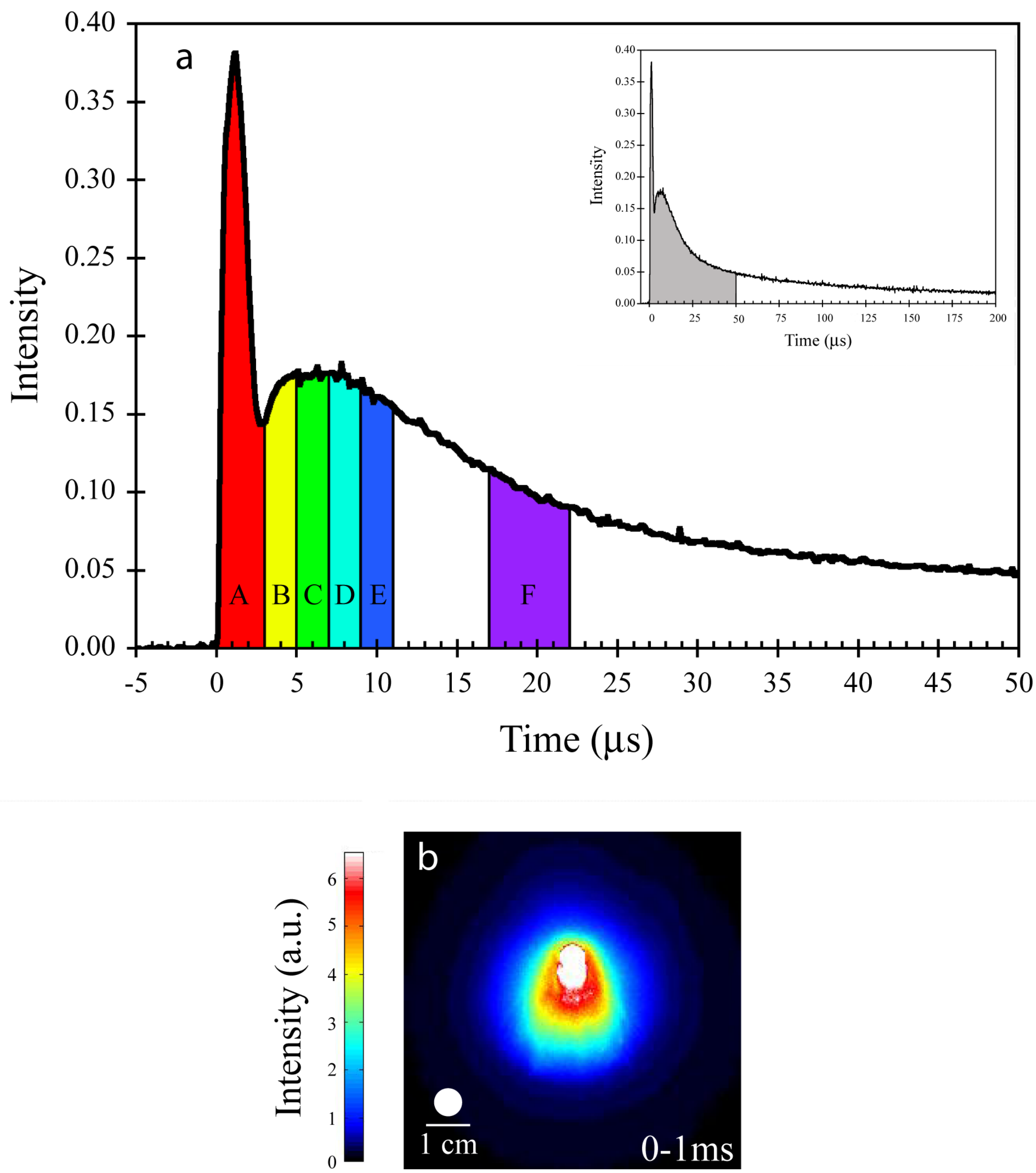

Chapter 3, Figure 11

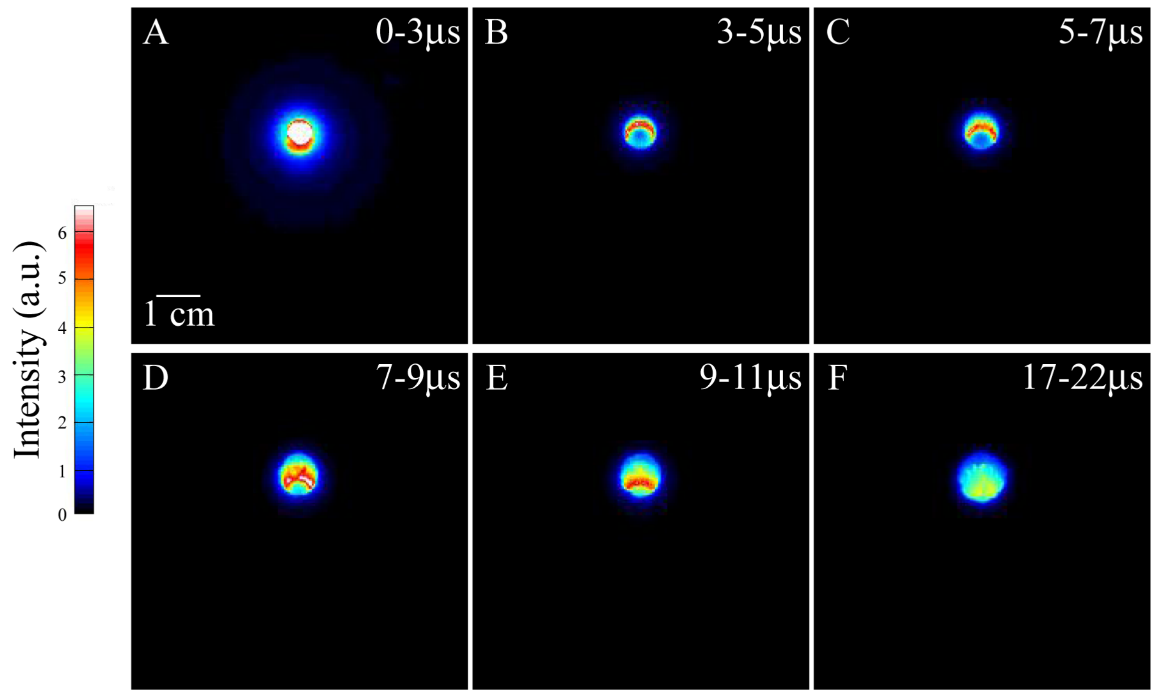

Chapter 3, Figure 12

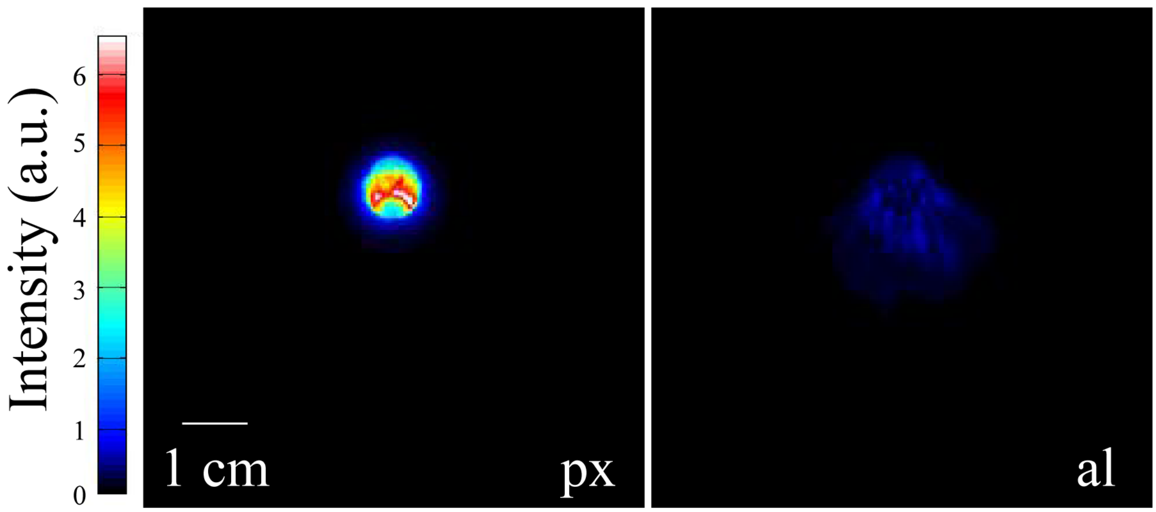

Chapter 3, Figure 13

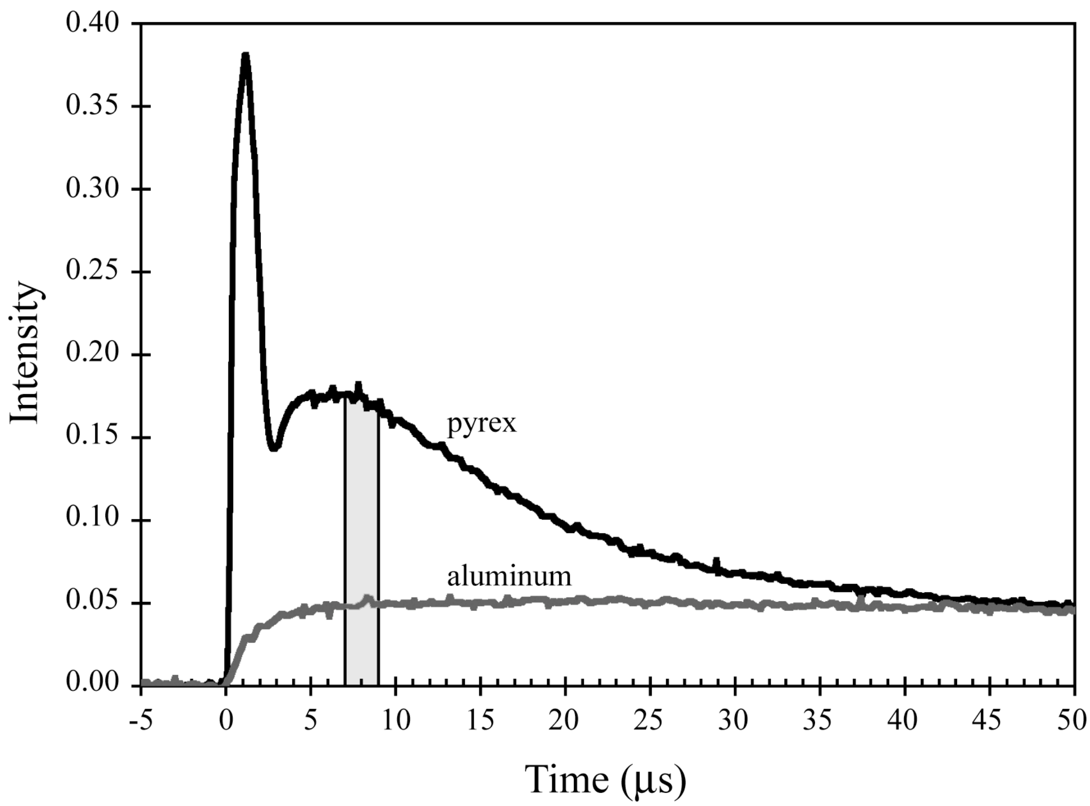

Chapter 3, Figure 14

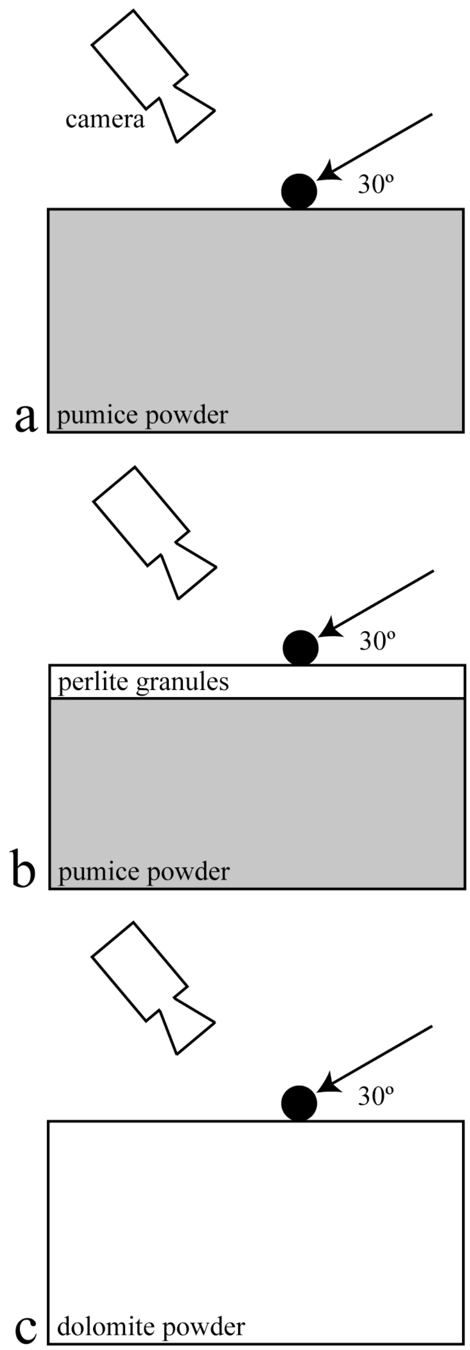

Chapter 3, Figure 15

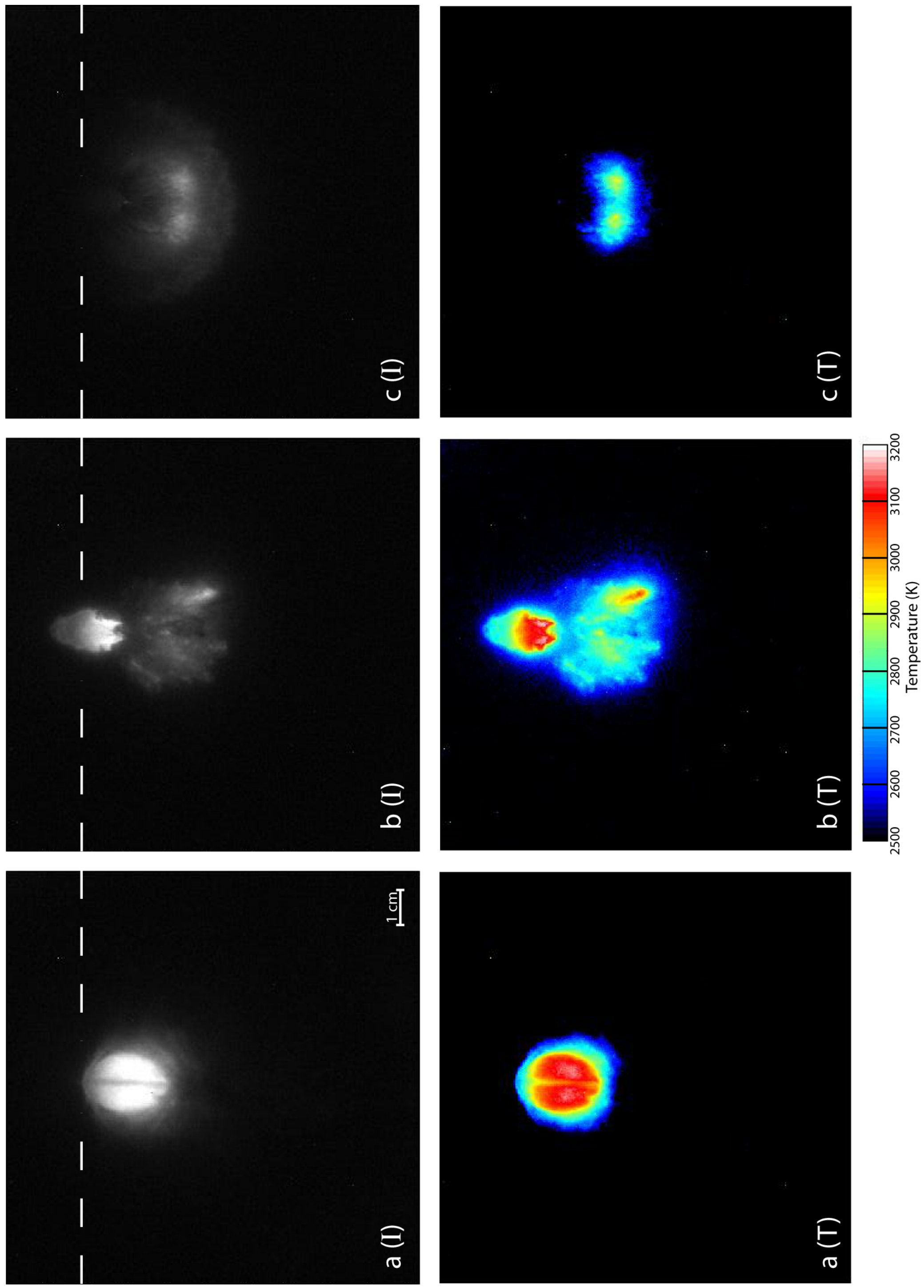

Chapter 3, Figure 16

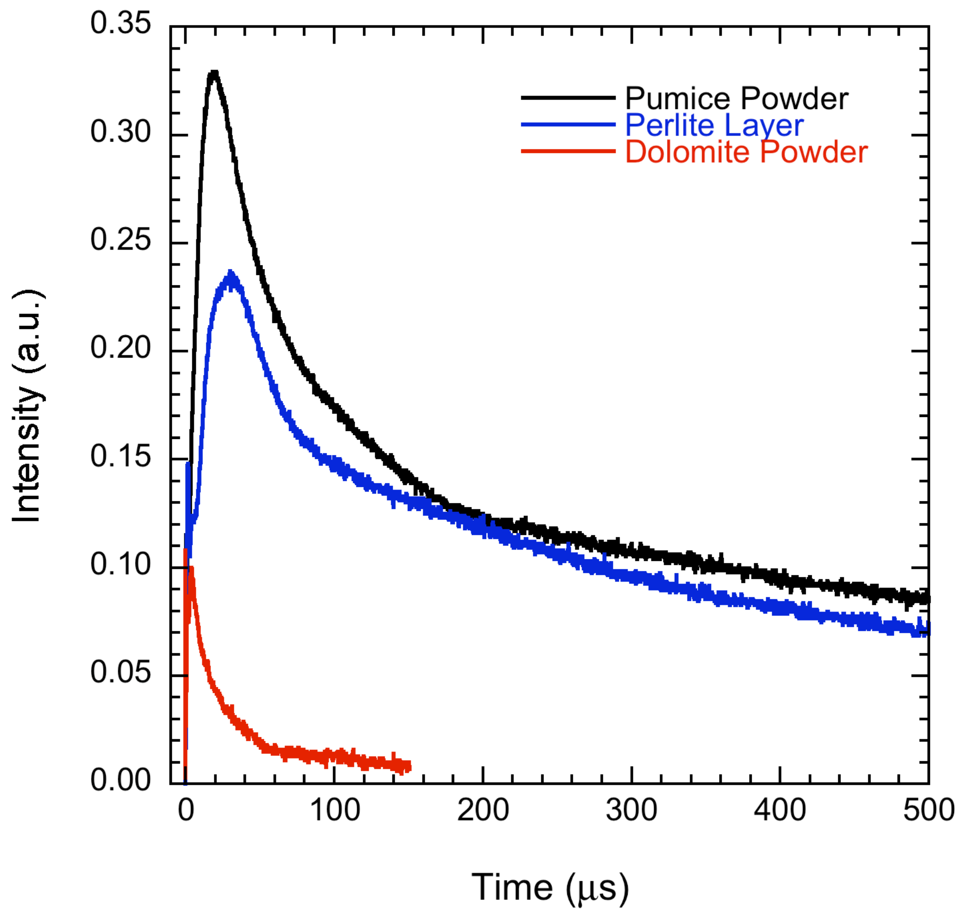

Chapter 3, Figure 17

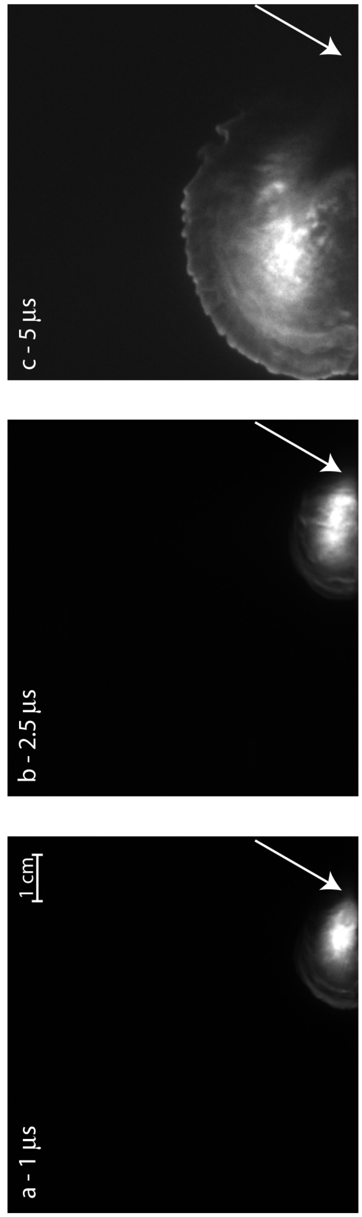

Chapter 3, Figure 18

Chapter 4

Evolution of the Deep Impact Flash: Implications for the Nucleus Surface Based on Laboratory Experiments

Carolyn M. Ernst

Peter H. Schultz

Department of Geological Sciences

Box 1846

Brown University

Providence, RI 02912

Published in its present form in:

Icarus, **190**, 334-344, doi:10.1016/j.icarus.2007.03.030, 2007.

Abstract

The Deep Impact flyby spacecraft obtained high-speed images of the evolving impact event. Multiple exposures captured a self-luminous impact flash, caused by the heating and vaporization of the cometary surface. Laboratory investigations show that target conditions affect the photometric and spatial evolutions of the impact flash; thus, the flash can be used to constrain the state of the target if the other initial impact conditions are known. Through comparisons of DI flash observations to laboratory impact experiments, the impact flash evolution can be used to determine the type of impact that occurred and to interpret the nature of the impacted Tempel 1 surface. The Deep Impact flash was of relatively long duration, though its luminous efficiency was an order of magnitude lower than expectations. Both uprange and downrange self-luminous plumes were observed. Comparisons of the DI observations with the results of laboratory experiments suggest that the surface of Tempel 1 contains silicates, volatiles, and carbon compounds, and is a highly-porous substrate.

1. Introduction

The NASA Deep Impact (DI) mission performed a planetary-scale impact into Comet 9P/Tempel 1 on July 4, 2005 at 05:44:36 UTC. The mission was designed to explore the structure and composition of a cometary nucleus by observing the impact event. The impact conditions were well known and controlled, as they are in laboratory experiments: a 370 kg impactor (49% copper by weight) impacted the comet at 10.3 km/s, delivering ~20 GJ of energy to the nucleus [*A'Hearn et al.*, 2005]. The impact was oblique, occurring at an angle between 25º and 35º (measured from the horizontal) as determined by flyby spacecraft images, a derived shape model [*Thomas et al.*, 2007], and the foreshortening of circular features [A'Hearn *et al.*, 2005]. Many phenomena can be used to analyze and assess various aspects of an impact in order to interpret the event and to constrain or determine any unknown conditions. In the case of the Deep Impact experiment, the major unknown was the state of the target: the Tempel 1 nucleus. The impact flash is one phenomenon that can be used to place constraints on the nucleus structure.

Hypervelocity impacts induce heating and vaporization in both the projectile and the target. Assuming the heated material radiates as a blackbody, the emitted energy follows a universal wavelength spectrum. The total energy partitioned to the target increases with the initial kinetic energy of the projectile, resulting in higher material temperatures.

Wien's law states that the wavelength at which the maximum specific intensity is radiated (λ_{max}) is inversely proportional to the temperature (T):

$$\lambda_{\max} = \frac{b}{T} \qquad (1)$$

where b is the Wien displacement constant. At high enough temperatures, the radiated light includes wavelengths in the visible range (as well as in the infrared and, if hot enough, the ultraviolet) that can be detected with instruments sharing the spectral response range of the human eye. This visible radiation is known as the "impact flash".

The impact flash is a well-documented phenomenon that has been observed during natural impacts as well as during laboratory impact experiments. Several studies have documented light flashes caused by meteoroid impacts into the Moon [e.g., *Bellot Rubio et al*., 2000a, 2000b; *Ortiz et al*., 2000, 2002; *Yanagisawa and Kisaichi*, 2002] and in a more extreme (and more complicated) case by the Shoemaker-Levy 9 impacts into Jupiter's atmosphere [e.g., *Zahnle and MacLow,* 1995]. These impacts were natural events, which are difficult to observe and are rare occurrences. In both the lunar meteoroid and Shoemaker-Levy 9 cases, the major unknown initial conditions were the projectile properties (e.g., size, composition). The Shoemaker-Levy 9 flash, however, was an atmospheric entry phenomenon.

The impact flash has been studied extensively in laboratory settings, where initial conditions can be controlled, repeated, and systematically varied. Previous studies quantified the effect of impact velocity, angle, projectile diameter, and projectile and target composition on the resulting flash and derived relationships between the initial conditions and the resulting impact flash peak intensity, temperature, duration, and luminous efficiency [e.g., *Gehring and Warnica,* 1963; *Eichhorn*, 1976; *Kadono and Fujiwara,* 1996; *Ernst and Schultz,* 2002-2005].

Experimental impacts into particulate silicate targets produce prolonged impact flashes that last orders of magnitude beyond the time it takes the projectile to penetrate the target [*Ernst and Schultz*, 2003]. In these experiments, the impact heats the particulates, which act as blackbody radiators that cool over time. Most of the heated particulates remain inside of the developing crater, either lining the cavity or being buried within the target. At later times, some heated material leaves the impact site as ejecta. If volatiles are introduced into the original target, heated particulates can be entrained inside of the evolving vapor plume. In the case of an oblique impact, this plume can transport the radiating particulates downrange of the impact site [*Schultz*, 1996; *Schultz et al.*, 2006].

Experimental impacts demonstrate that the observable photometric and spatial evolutions of an impact flash are highly dependent on initial conditions. The initial kinetic energy of the projectile, the impact angle, and the target properties (e.g., porosity, composition) have significant and observable influences on the magnitude and evolution of the impact flash. Because of these dependences, laboratory-derived relationships can be used to predict the evolution of an impact flash for given impact conditions. Alternatively, analysis of the impact flash evolution allows unknown conditions to be constrained when most of the initial conditions are known.

Despite the strengths of laboratory settings, laboratory impact experiments cannot achieve the full range in size, speed, and gravitational conditions of natural impacts. For this reason the DI collision was a novel experiment, occurring at large scales outside of a laboratory while most of the initial conditions were controlled. Because DI is the first experiment of its kind, there are no similar experiments for comparison. Thus, laboratory impact studies are essential for understanding the DI event in particular, and impact processes in general.

The duration of an impact flash depends on initial conditions, especially the scale of the event (velocity, size). The afterglows from laboratory impact flashes can last as long as ~ 2 ms for macroscopic impacts into particulate silicate targets [*Ernst and Schultz,* 2003], whereas lunar meteoroid impact flashes have been observed for as long as 600 ms [*Ortiz et al*., 2002]. All other conditions being the same, larger-scale events are expected to produce longer-duration flashes due to the greater mass of heated target material. The large scale of the DI event means the entire cratering processes, including the impact flash duration, will operate on a longer timescale than in the laboratory.

One method of scaling the timescale of the event is to relate the time after impact (t) to the penetration of the projectile (the time it takes the projectile to travel its diameter into the target):

$$\tau = \frac{t}{a/v} \quad (2)$$

where a is the projectile diameter and v is the impact velocity [*Schultz et al*., 2005]. Whereas the flash typically lasts ~ 2 ms, or τ ~ 2000, for the current impact experiments, the same flash would last significantly longer at DI size and velocity scales (assuming all other initial conditions are the same), where τ = 2000 is equivalent to a time of ~2000 ms.

In this paper we investigate the photometric and spatial evolutions of the DI impact flash based on images taken by the flyby spacecraft. We compare the DI flash to experimental results in order to interpret the event. Comparisons of the spacecraft observations with the Schultz *et al*. [2005] pre-mission predictions help to assess the validity of extrapolations based on laboratory experiments and to evaluate the differences between the laboratory impacts and the Deep Impact collision. Our results include the calculation of the luminous efficiency of the DI flash, as well as interpretations of the impact event and implications for the nature of the Tempel 1 surface.

2. Deep Impact Observations

Two instruments onboard the DI flyby spacecraft observed the impact event, the Medium Resolution Instrument (MRI) and the High Resolution Instrument (HRI). Though having a lower spatial resolution, the MRI images had a much shorter time resolution than the HRI images during and immediately after the moment of impact (59 ms versus ~ 840 ms) and provide the only data on the flash evolution. The MRI consists of a filtered visible-light CCD camera (0.32 – 1.05 μm) connected to a telescope with a 12 cm aperture and a 2.1 m focal length [*Hampton et al*., 2005]. The image sequence recorded from I-0.5 s to I+1.0 s (where I is the expected time of impact) was designed to capture the initial stages of the impact event at the fastest possible time resolution (59 ms) and at a spatial resolution of 86 m/pixel [*Klaasen et al*., 2005]. The sampling rate encompassed a 51.4 ms exposure plus 7.6 ms for data readout. The separation angle between the flyby spacecraft's view of the impact point and the impactor itself was 3.3º, resulting in a highly oblique view angle of the impact event (very close to the angle of impact). Figure 1 is a composite image of the Tempel 1 nucleus, composed of the best images taken by the impactor targeting sensor (ITS) on board the impactor spacecraft. The box indicates the MRI field of view at the time of impact. The entire evolving impact flash remained within the MRI field of view.

Multiple MRI exposure frames captured the impact flash produced by the DI collision. The flash evolved most dramatically over the first nine post-impact MRI images (exposure IDs 9000910_064-072), which cover the first ~ 530 ms after impact and are depicted in Figure 2. The labeled post-impact times are with respect to the "first light" (first flash appearance) in the exposure started at 05:44:36 UTC (frame A).

The MRI exposure sequence introduces small uncertainties when analyzing the evolution of the impact flash. The changes to the flash within an exposure cannot be determined. Though not a significant concern at later times, at early times the impact flash evolved rapidly with respect to the time resolution of the MRI, making it more difficult to interpret the flash evolution. Similarly, the "first light" signal could have appeared at any point during the frame A exposure. Another issue is the 7.6 ms time gap between exposures when the comet was not being imaged. The absence of these data results in further uncertainty, especially when there appear to be large discontinuities in the photometric evolution (e.g., between frames C and D, and between frames D and E). The saturation of the detector also leads to uncertainty, as any measured saturated value must be considered as a minimum. Despite the uncertainties inherent to the exposure sequence, the MRI images contain sufficient information to determine the photometric and spatial evolutions of the impact flash. The following overview of the phenomenology contains some interpretations based on analyses that will be described later in the text.

2.1. Deep Impact Flash Intensity Overview

The "first light" was relatively small and dim and was mostly confined to one pixel (frame A in Figure 2). A delayed brightening began by ~ 118 ms (frame C), after which the light intensity quickly increased to the point of detector saturation (frame D), leading to the horizontal charge bleeding seen in frames D and E. As the bright flash evolved further, a luminous plume appeared and expanded downrange, away from the point of impact. The leading edge of the plume can be easily seen in frames E – G (and is indicated by arrows in frames F – I). Both the early central portion of the light signal (consisting of the first light, the delayed brightening, and the saturated signals) and the downrange plume were self-luminous and make up what is considered to be the impact flash.

A second light source emerged from the impact point by 295 ms (frame F) and grew in both area and intensity during subsequent exposures. The source of this light was sunlight reflecting off of the expanding central ejecta cloud. Since this source was not self-luminous, it is not considered to be a part of the impact flash; if the impact had occurred on the dark side of the nucleus, the MRI would not have observed this component. The ejecta cloud casts a shadow onto the nucleus, which is first visible in frame F. The existence of the shadow indicates that at this time (295 ms after impact) the reflecting ejecta cloud was optically thick.

In contrast to the ejecta cloud, none of the impact flash components cast observable shadows onto the nucleus. This could imply that these components were optically thin, though it is possible that these components had strong enough self-luminosity to illuminate the surface, eliminating a potential shadow. Based on preliminary modeling, *Melosh et al*. [2006] state that the downrange luminous plume was optically thin in all images with the possible exception of its first appearance (frame D).

Figure 3 depicts the photometric and spatial evolution of the impact flash in a false-color representation in order to better view intensity variations. Here, the color scale corresponds to the intensity of the recorded light signal. The frames correspond to a zoomed in view of those in Figure 2, and the arrow in frame A represents the direction of impact. The final pre-impact MRI image (9000910_063) was subtracted from each post-imapct MRI image in order to remove non-impact related light sources (including sunlight reflecting off of the nucleus surface).

2.2. Photometric Evolution

Two light source components associated with the impact were observed: an early-time self-luminous source (the impact flash) and a later-time, reflected-light source (the expanding ejecta cloud). Figure 4 shows the evolution of the spatially integrated DI light intensity through time with respect to the appearance of the first light (displayed as the cumulative intensity of a given component for each MRI exposure). The MRI CCD has a linear response; so, the bleed-over light from each of the two saturated frames (D and E) was summed to determine the minimum total brightness for these exposures.

The self-luminous component on the graph represents the impact flash, consisting of the light flux spatially integrated over not only the central "first light" (A, B) and delayed brightening (C – E), but also the expanding downrange plume (E – I). The overall photometric evolution began as a faint signal that faded before quickly and dramatically undergoing a delayed brightening, bringing the signal beyond the level of detector saturation. After this point, the signal slowly decayed. The primary light source for the impact flash component is thermal radiation from heated and melted ejecta particulates. The intensity of the entire central reflected-light portion of the light signal initially underwent linear growth (beginning in frame F, 295 ms), but by ~ 650 ms after impact its growth began to slow, diverging from this linear trend.

2.3. Spatial Evolution

The center of brightness of the impact flash moved over the first ~ 175 ms after impact. In order to examine this movement, center of brightness positions from successive MRI exposures (corresponding to frames A-D of Figure 2) were resized and overlain onto a deconvolved HRI/ITS composite image of the nucleus (Figure 5). Figure 5 contains the overlay of the entire nucleus as a context image, as well as a zoomed-in view of the impact site and surrounding region.

The projected movement of the flash was along a line lying at an angle to the impactor trajectory, i.e., not along a surface tangent. The center of brightness of the "first light" signal (A) occurred one pixel uprange from the location of the delayed brightening in frame C (~ 100 - 200 m, taking into account the oblique view angle). This delayed signal was located another 100 - 200 m uprange from the center of brightness of the first saturated image (D). The movement between frames C and D was likely due to the initial downrange emergence from the impact site of the plume containing hot vapor, gas, and entrained particulates. The movement between A and C was due to a more complex process, which will be explored, with input from laboratory experiments, in Section 4.

3. Experimental Results

The Deep Impact collision was a one-of-a-kind impact event: most of the variables were controlled as in laboratory experiments, but the impact occurred at planetary scales. The possible outcomes of the collision were explored through the use of laboratory analogs to DI conditions. By comparing and contrasting photometric and spatial characteristics of laboratory impact flashes and DI observations, we can place constraints on the type of impact that occurred and the nature of the Tempel 1 nucleus surface.

The DI impact velocity was only about twice that typically achieved by experiments (10.3 km/s versus ~5.5 km/s); however, the DI projectile was ~10^6 times more massive (370 kg versus 0.30 g). Together, these scale differences translate to an initial DI kinetic energy ~4×10^6 times larger than typical laboratory kinetic energies (20 GJ versus 5 kJ). The great difference in projectile kinetic energy introduces challenges when scaling the laboratory results to DI conditions. For example, with so much more energy available, some materials will vaporize that otherwise would remain in solid or liquid form. Other challenges arise since the materials used in experiments are not the same as those found on a cometary surface.

To address these challenges, various targets were chosen for their specific characteristics: pumice dust (non-volatile, silicate, particulate), solid pumice block (strength), perlite granules (high porosity), dolomite (easily vaporizable under laboratory conditions), and sugar (carbonaceous composition). These target materials were not used to reproduce the surface of Tempel 1; rather, they are surrogates used to assess the effect of their specific properties on the resulting light signal.

3.1. Target Effects on Impact Flash Photometric Characteristics

The peak intensity, duration, and luminous efficiency of an impact flash are all easily observable photometric characteristics that are greatly affected by target properties. The luminous efficiency of an impact (η) is the fraction of the initial kinetic energy (KE_o) emitted as luminous energy (LE) over a given wavelength (λ_1 to λ_2) when an impact occurs:

$$\int_{\lambda_1}^{\lambda_2} LE = \eta \cdot KE_o . \tag{3}$$

We consider the luminous efficiency over a primarily visible wavelength range for this study, since the MRI observed the Deep Impact collision from 0.32 – 1.05 μm.

In practice, not all of the light generated by an impact will be observable by a detector above the surface, thereby affecting the observed luminous efficiency. During laboratory impact experiments, some of the emitting material can be buried in the target or obscured by other ejecta. In addition, the developing transient crater can prevent radiating material from being exposed at the surface. The degree to which the obscuration occurs relates to the nature of the target and the impact angle. For example, obscuration by the transient crater becomes more pronounced in the case of a high-porosity target, where the transient crater is extremely narrow and deep before eventually opening and exposing its contents at the surface [*Schultz*, *et al*. 2005].

Experimental impacts were performed at the NASA Ames Vertical Gun Range to explore the effects of target porosity and composition on the resulting impact flash. In order to minimize the number of variables, target type was the only initial condition changed. The impact velocity for all of the experiments described in this section was

5.67 ± 0.16 km/s, and the impact angle remained constant at 30º from the horizontal. All projectiles were 0.635 cm-diameter Pyrex spheres. At these velocities, Pyrex disrupts completely on impact, thus better simulating conditions met during larger-scale impacts [*Schultz and Gault*, 1990]. All of the experiments in this study took place under near-vacuum conditions (< 0.72 mbar). At these very low pressures, the residual atmosphere does not affect the brightness or the evolution of the flash [*Ernst and Schultz,* 2004].

Materials of similar particulate silicate composition were used to vary the target porosity from as low as 43% (pumice powder, 81 μm mean grain size) to as high as 90% (perlite granules, sieved to < 500 μm). Table 1 contains the composition and porosity for all of the target materials used in this study. The effect of target porosity on the impact flash evolution can be seen in Figure 6. As the porosity increases, the peak intensity, overall impact flash brightness, and duration decrease, resulting in a lower measured luminous efficiency. As the porosity increases from 43% to 90%, the luminous efficiency decreases by two orders of magnitude, from ~ 10^{-4} to 10^{-6}.

Two major factors contribute to the lower photometric signal. First, as the projectile penetrates a highly-porous target, it encounters less mass per unit length along its path. Although shockwaves are known to heat porous materials to higher temperatures than non-porous materials (energy is irreversibly partitioned into heat through the compaction of pore space) [*Love et al.,* 1993], there are initially few radiating sources produced near the surface, resulting in a lower initial photometric signal.

Second, a projectile impacting a highly-porous target penetrates much deeper before its energy and momentum are fully coupled to the target. The result is a long and narrow transient crater [*Schultz et al*., 2005]. This deep penetration confines the heated material at early times, and prevents much of the initial light radiation from emerging above the surface and out of the transient crater. The result is a lower photometric signal due to there being fewer observable radiating sources.

The relationship between target porosity (ϕ) and luminous efficiency (η) can be defined quantitatively (Figure 7). When examining the three targets of similar composition (pumice powder, solid pumice, perlite), the relationship follows an exponential function:

$$\eta = c_1 e^{c_2 \phi} \tag{4}$$

where c_1 and c_2 represent constants. For the current laboratory experiments, the best fit to the data results in a value of c_1 = 0.0011 and c_2 = -5.4. It should be stressed that this relationship was derived using targets of similar particulate silicate composition, at the same impact angle, velocity, and projectile diameter. With assumptions, this relationship can be applied to the DI observations to estimate a porosity value for the Tempel 1 surface. This estimate is discussed in Section 4.1.

The effect of target volatile content on the impact flash was explored by using particulate dolomite, which is easily vaporizable under laboratory impact conditions. Volatiles in the target (in the absence of an atmosphere) also decrease the brightness, duration, and luminous efficiency of the flash (Figure 6). When volatiles are present, some of the impact energy is partitioned into vaporization and vapor expansion. Much of the emitted light is in the form of atomic and molecular emission lines at specific wavelengths, as opposed to a blackbody continuum [*Eberhardy and Schultz,* 2004]; thus, the overall luminous efficiency is relatively low.

Impacts into targets containing carbon (sugar in the case of this study) yield flash evolutions distinct from those previously discussed. The resulting impact flash is of intermediate duration and brightness compared to flash signals from impacts into porous, volatile, and pumice powder targets (Figure 8). For a target made completely of sugar, the impact flash begins with a bright intensity spike that fades and undergoes a secondary, delayed brightening.

Under laboratory conditions, sugar vaporizes on impact. This process is reflected in the in the rapid intensity drop after the first contact spike. As the vapor cloud cools, particles begin to condense from the vapor and begin to radiate as blackbodies. Because these particles condense over time, the secondary peak intensity is delayed and occurs at a much later time than the secondary peak intensity observed during impacts into pumice powder targets. The flash evolution undergoes an intermediate amount of change for impacts where the carbonaceous material is mixed into the target in smaller amounts. In contrast, the vaporization of a pumice target is minimal at laboratory-scale impact velocities; thus, heated pumice particulates continually radiate, resulting in a relatively continuous impact flash signal. The high emissivity of carbon and the possibility of secondary chemical reactions during condensation and recombination may also enhance the light flash [Schultz *et al*., 2007].

3.2. Target Effects on Impact Flash Spatial Distribution

The use of a high-speed thermal imaging camera reveals the spatial distribution of self-luminous material for experimental impacts. Major differences in the distribution are observable when comparing impacts into targets of various porosities. Figure 9a illustrates a side view of the setup for two experimental impacts. The experiments impacted 0.635 cm Pyrex spheres traveling at ~ 5.50 ± 0.03 km/s and at 30º angles (from the horizontal) into pumice powder under an ambient near-vacuum (0.64 mbar). Though otherwise identical, a projectile-thick layer of highly porous perlite granules overlaid the impact II pumice powder target. The target materials are the same as those described in Table 1. The camera was positioned above and slightly downrange of the impact point, and a 250 ns exposure was taken 20 μs after each impact.

Figure 9b shows the resulting images taken by the thermal camera. The direction of impact and the approximate uprange/downrange location of the impact point are indicated in the figure. The experiments occurred in the dark, with no ambient light reaching the camera; therefore, the impacts generated all of the imaged light. Despite the thinness of the high-porosity layer, its presence had a significant effect on the resulting light distribution and intensity. The light generated by impact I is located entirely downrange of the impact point at the time of the exposure, and is confined to a well-defined area. The light generated by impact II extends not only downrange but also uprange of the impact point. The downrange component is fainter and much more diffuse than in impact I. Consequently, some of the emitting material may lie underneath the target surface at the interface between the perlite and the pumice powder layers. *Schultz et al.* [2005; 2007] also observed this phenomenon from a side view in quarterspace impact experiments.

The uprange portion of the impact II light signal is an uprange plume. *Schultz* [1996] and *Schultz et al*. [2007] address the general evolution and source of such plumes during impacts into highly porous targets. Because a projectile penetrates deeply into a high-porosity target, the early-generated vapor component is contained by the transient cavity, a phenomenon known as cavitation. A highly-collimated plume is directed back up the impactor-generated penetration funnel and travels uprange at a relatively high angle. Parts of the uprange plume are initially self-luminous, but because it is composed mostly of vapor phases, the plume remains relatively dim.

Figure 10 shows the light curves of impacts I and II out to 500 μs after impact, as recorded by a photodiode (sensitive to the 0.35 – 1.10 μm wavelength range). The photodiode was positioned above and slightly uprange of the impact point. Though the overall shapes of the curves are similar, there are observable details that differentiate the two. The impact II rise time (time to the peak) was ~ 40% longer than that of impact I, and the impact II curve displays a visible change in decay rate at ~ 70 μs. At later times (> 250 μs), both light sources decayed at similar rates and had similar durations.

The cumulative light output for impact I was only ~ 15% more than that for impact II. Since the porous layer was only as thick as the projectile, it initially affected the distribution and evolution of the light output at early times, but at later times the photometric decays were similar. If the porous layer were thicker, the light curve differences would be more pronounced and would persist longer into the recorded light signal.

4. Analysis and Interpretations

The expanding downrange plume is known to be self-luminous because it passed by the spectrometer slit during the first HRI-IR exposure (~ 200 – 250 ms after impact) as described by *A'Hearn et al.* [2005]. The continuum temperature of the downrange plume at this time was modeled to be ~ 850 K. The spectrometer also observed emission lines from vapor species with peak temperatures between 1000 and 2000 K. These observations indicate that the plume was composed of hot dust particles that were entrained in the downrange-moving and expanding vapor. The dust particles acted as blackbody radiators that cooled over time as the plume expanded. At earlier times (< 200 ms after impact, before the plume passed by the slit) this dust component would have been even hotter. *Melosh et al*. [2006] modeled the dust component as a cloud of 150 μm diameter liquid silicate droplets that cooled from an initial temperature of ~ 3500 K.

Experimental oblique impacts produce a downrange-moving vapor plume that travels along the surface at a velocity comparable to the initial impact velocity while expanding hemispherically [*Schultz et al*., 2005; *Schultz*, 1996]. On a three-dimensional body, this plume evolves into a spherically expanding cloud. The oblique view angle of the DI collision requires that the downrange plume velocity be corrected, taking into account the projection. Consequently, the observed downrange speed of ~ 6 km/s for the leading edge becomes ~ 12 km/s, assuming a 30º impact angle.

4.1. Luminous Efficiency and Duration

First-order predictions for the brightness and duration of the DI flash were based on extrapolations from laboratory impacts [*Schultz et al*., 2005; *Ernst and Schultz*, 2005]. For reference, the predictions incorporated a simplified assumption of a pumice powder-like target (no volatiles, 43% porosity), although target porosity and volatile content were observed to also affect the duration and intensity of the impact flash. The flash was predicted to last at least 0.06 s (one MRI exposure frame), with the prospect of lasting 10

– 50 times longer if the Tempel 1 surface is particulate and silicate-rich. The predicted cumulative luminous energy output under these assumed conditions was ~ 15 MJ, thereby resulting in a predicted luminous efficiency (in the MRI wavelength range) of the DI flash of ~ $8x10^{-4}$.

The actual luminous efficiency of the DI flash was calculated by integrating the total light output over time of the self-luminous components of the impact-induced light signal. Simple linear interpolation between frames accounted for the brief time gaps. Due to the saturated images, the calculated luminous efficiency value must be considered a lower limit. However, the inclusion of the spill over pixel values into the total luminous energy output reasonably compensates for the saturation and provides a closer estimate of the actual brightness. The calculated luminous efficiency based on the MRI images was ~ $7x10^{-5}$, an order of magnitude less than predictions. This difference most likely results from the use of silicate powder as the reference target, which was not meant to represent the Tempel 1 surface. The actual light output of an impact is affected by factors that were purposely not taken into account for the prediction, such as target porosity, particle emissivity, volatile content, strength, and optical depth. Consequently, the difference between predictions and observations provides useful information about the nature of the surface materials of Tempel 1 at the impact site. The dimmer than expected luminous efficiency implies that the surface is highly porous, contains volatiles, or a combination of the two.

Although the predicted and measured values of the total luminous output differed, the flash duration was actually consistent with the lower bound of expectations for a long-lasting flash [Schultz *et al.*, 2005]. Laboratory impacts into highly porous (perlite) and highly volatile (particulate dolomite) targets demonstrate that the impact flash is much shorter than the flash from impacts into pumice powder. Any porosity or volatiles on the surface of Tempel 1 would drastically shorten the duration of the self-luminous component, perhaps even confining it to one MRI exposure. Since the signal was significantly longer than one exposure, another factor must be acting to lengthen the signal duration. Carbon-based compounds (CH-X) are known to exist on or near the surface of Tempel 1 based on spectral measurements during the impact event [*A'Hearn et al*., 2005; *Sunshine et al*., 2007]. These compounds may contribute to the reduced luminous efficiency yet prolonged duration of the flash due to their high emissivity and the possible evolution of back reactions within the vapor plume.

The relationship between target porosity and luminous efficiency (Equation 4) can be scaled to DI conditions by making a few assumptions. First, it is assumed that the exponential constant (c_2) is the same at all scales. Second, c_1 is calculated to be 0.0082 based on the predicted DI luminous efficiency value of 8 x 10^{-4}, assuming a 43% surface porosity and a silicate target [*Schultz et al*., 2005]. Plugging both this new c_1 and the DI luminous efficiency calculated here (a lower limit of 7 x 10^{-5}) into Equation 4 yield an 88% porosity value for the upper surface of the comet. For a silicate surface composition (2.2 g/cm^3), this corresponds to a surface density of 0.26 g/cm^3. If the actual luminous efficiency were twice as high as the calculated lower limit (to try to compensate for saturation effects), the values would be 75% porosity and 0.55 g/cm^3.

Because of the assumptions made and the factors not taken into account, especially target composition, these calculations must be considered an exercise. Various phenomena observed in the DI event, however, are similar to those seen in laboratory impacts into targets with porosities in this range [*Schultz et al.,* 2007]. *A'Hearn et al.* [2005] place a rough estimate of 0.6 g/cm^3 on the bulk density of the Tempel 1 nucleus. This value is close to those calculated here, and it is reasonable to believe the surface density of the nucleus would be lower than the bulk density; therefore, the results of this exercise have some merit.

4.2. Source Movement

The faint "first light" appears uprange of the projected impact point (Figure 5). In subsequent images, the center of brightness of the impact flash moves in a downrange direction, traveling closer to the impact point. This motion indicates that the first light represents a self-luminous component uprange from the developing crater.

The view angle of the impact was 3.3º off of the impactor trajectory, thus any early light source inside of the transient crater would appear along the projected trajectory. The first light appears slightly off-axis from the trajectory, indicating that the light source rose above the surface at an angle higher than the impact angle. Consequently, the first light does not represent the path of the projectile through an upper surface.

The apparent motion and the off-trajectory position of the first light are consistent with the existence of an uprange plume created by the containment and redirection of vapor by a deep and narrow transient crater. The self-luminous nature of the uprange plume is mainly due to atomic and molecular emission lines. This light component fades quickly due to a low affected mass and the lack of significant thermal emissions. Predictions made by *Schultz et al*., [2005], observations of the DI event made by the

Hubble Space Telescope [*Feldman et al.,* 2007], and data from the DI flyby spacecraft [*Schultz et al*., 2007] support the existence of a long-lasting, uprange plume. Based on results from laboratory impact experiments, the existence of an uprange plume implies that the surface of Tempel 1 is highly porous. This conclusion is consistent with those derived from the photometric characteristics.

4.3 Summary

The initial faint flash followed by the delayed saturated flash farther downrange can be explained by an oblique impact into a low-density (0.2 to 0.5 g/cm^3) particulate target as documented in laboratory experiments. In this scenario, the first light is a plume of radiating dust and gas directed uprange of the initial penetration funnel due to cavitation. In laboratory experiments, this initial plume is highly collimated and is relatively faint due to the low affected mass (caused by high target porosity) and/or the dominance of vapor phases (absence of significant thermal radiation) [*Ernst and Schultz*, 2005]. The apparent movement of the early flash is due to the evolution of this uprange plume and the subsequent opening of the transient crater.

As the transient crater develops, the initial penetration funnel opens, exposing the once-hidden, shock-heated material at the surface as it emerges and moves downrange of the impact point (corresponding to frames D and E from Figure 2) while retaining a substantial fraction of the initial impact velocity [*Schultz*, 1996; *Ernst and Schultz*, 2003]. Hot, radiating particulates entrained in this vapor plume move and expand downrange of the impact point. Vapor expansion adds an additional velocity component to the plume's leading edge. Tracing the downrange plume back to the moment of emergence from the surface indicates that this velocity component should appear ~ 100 ms after the first light. The subsequent delay in the bright flash can be interpreted as the combination of the initial rapid expansion, the time before the opening of the penetration funnel, obscuration during projectile entry, and the initial absence of thermal radiation due to the early dominance of emission lines (see *Schultz et al*. [2007]). Such a scenario was outlined as a predicted result of a highly porous Tempel 1 nucleus in *Schultz et al*. [2005]. A highly porous surface layer is also supported by the analyses performed by *Schultz et al*. [2007] and *Richardson and Melosh* [2006].

Spectral data and observations of the post-impact downrange vapor plume are evidence that volatiles exist on or near the Tempel 1 surface [*A'Hearn et al*., 2005; *Sunshine et al*., 2006]. Though their presence may contribute to lowering the luminous efficiency of the DI collision, it cannot explain all of the observed phenomena; volatiles alone will not produce an uprange plume. The surface also must contain significant quantities of "dust" (or condensates) to create the thermal signal entrained in the downrange vapor plume, some of which could be silicate in nature, and some of which could be condensed, high-emissivity carbon. Both silicate dust and carbonaceous material were detected in the initial self-luminous plume by the IR spectrometer [*Sunshine et al*., 2007; *A'Hearn et al*., 2005].

5. Conclusions

The Deep Impact flyby spacecraft successfully recorded the light flash produced by the impactor's collision with comet Tempel 1. The "flash" persisted through multiple MRI exposures, which enabled the analysis of the flash evolution through time. The photometric and spatial evolutions of the DI flash provide independent constraints on the nature of the Tempel 1 surface through comparisons with laboratory impact flash data.

The DI impact flash consisted of three self-luminous components: the “first light”, the saturated central flash, and the downrange plume. The “first light” appeared uprange of the projected point of impact. The light intensity then faded briefly before undergoing a second brightening at a position closer to the impact point. This central self-luminous component quickly and dramatically brightened, which resulted in detector saturation. A downrange-moving plume then emerged from the impact site, consisting of vapor and entrained, radiating dust particles. The combined luminous efficiency of these three components was lower than predictions based on simplified laboratory experiments using silicate powder; however, the duration was comparable to predictions. The difference between the predictions and observations indicates the effect of high porosity and the presence of volatiles that suppress the luminous efficiency.

The photometric and spatial evolutions of the DI first light are consistent with the existence of an uprange plume directed up and out of the penetration funnel due to cavitation. The delayed brightening results from the emergence of heated material with the opening of the transient crater. Based on comparisons with laboratory impact flash studies, these observations and the low luminous efficiency are consistent with an under-dense (porous) target surface.

Volatiles exist on the Tempel 1 surface, as evidenced by the existence of the downrange plume. This plume entrained blackbody-radiating particles and translated them downrange away from the impact site. These entrained particles allowed the vapor plume to be easily detected by the MRI camera. The existence of a vapor plume is consistent with results from the MRI-IR spectrometer.

Though the DI flash was dimmer than predicted, its duration was on the long side of expectations, thereby suggesting an additional target component. The presence of carbon compounds could account for the long duration, since carbon compounds vaporize and condense at lower temperatures than silicates. The condensation of carbon compounds in the downrange plume would create new particulate radiators at later times, thus resulting in a long decay time. Future experimental studies will be able to quantify such effects.

The impact flash is an effective remote sensing tool. Details of the Tempel 1 surface were independently constrained by photometry alone, and these constraints agree with conclusions drawn through other means (e.g., spectrometry, ejecta behavior). Laboratory experiments are critical to understand the underlying processes that caused the observed photometric and spatial evolutions of the light flash.

Acknowledgements

We are grateful to D. Holt, D. Bowling, and R. Smythe at the NASA Ames Vertical Gun Range for their assistance and technical expertise. We thank M. F. A'Hearn for his valuable comments. We also thank N. Artemieva and an anonymous referee for their constructive reviews, which have improved the quality of this manuscript. This research was supported by the NASA Discovery Program Deep Impact mission (NASW-00004) and by the NASA Graduate Student Researchers Program (04-6011H).

References

A'Hearn, M. F., and 32 coauthors (2005), Deep Impact: Excavating comet Tempel 1, *Science, 310*(5746), 258-264.

Bellot Rubio, L. R., J. L. Ortiz, and P. V. Sada (2000a), Luminous efficiency in hypervelocity impacts from the 1999 lunar Leonids. *Astrophys. J. 542*, L65-L68.

Bellot Rubio, L. R., J. L. Ortiz, and P. V. Sada (2000b), Observation and interpretation of meteoroid impact flashes on the Moon, *Earth, Moon, and Planets 82-83*, 575-598.

Eberhardy, C. A., and P. H. Schultz (2004), Probing impact-generated vapor plumes, *LPSC, XXXV*, #1855.

Eichhorn, G., (1976), Analysis of the hypervelocity impact process from impact flash measurements. *Planetary and Space Sciences, 24*, 771-781.

Ernst, C. M., and P. H. Schultz (2002), Effect of velocity and angle on light intensity generated by hypervelocity impacts, *LPSC, XXXIII*, #1782.

Ernst, C. M., and P. H. Schultz (2003), Effect of initial conditions on impact flash decay, *LPSC, XXXIV*, #2020.

Ernst, C. M., and P. H. Schultz (2004), Early-time temperature evolution of the impact flash and beyond, *LPSC, XXXV*, #1721.

Ernst, C. M., and P. H. Schultz (2005), Investigations of the luminous energy and luminous efficiency of experimental impacts into particulate targets, *LPSC, XXXVI*, #1475.

Feldman, P. D., S. R. McCandliss, M. Route, H. A. Weaver, M. F. A'Hearn, M. J. S. Belton, and K. J. Meech (2007), Hubble Space Telescope observations of Comet 9P/Tempel 1 during the Deep Impact encounter, *Icarus, 187*, 113-122.

Gehring, J. W., and R. L. Warnica (1963), An investigation of the phenomena of impact flash and its potential use as a hit detection and target discrimination technique, *6th Symposium on Hypervelocity Impact*, 627-681.

Hampton, D. L., J. W. Baer, M. A, Huisjen, C. C. Varner, A. Delamere, D. D. Wellnitz, M. F. A'Hearn, and K. P. Klaasen (2005), An overview of the instrument suite for the Deep Impact mission, *Space Science Reviews, 117*, 43-93.

Kadono, T., and A. Fujiwara (1996), Observation of expanding vapor cloud generated by hypervelocity impact, *Journal of Geophysical Research, 101*(E11), 26,097-26,109.

Klaasen, K. P., B. Carcich, G. Carcich, E. J. Grayzeck, and S. McLaughlin (2005), Deep Impact: The anticipated flight data, *Space Science Reviews, 117*, 335-372.

Love, S. G., F. Horz, and D. E. Brownlee (1993), Target porosity effects in impact cratering and collisional disruption, *Icarus, 105*, 216-224.

Melosh, H. J., and the Deep Impact Team (2006), Deep Impact: The first second, *LPSC, XXXVII*, #1165.

Ortiz, J. L., P. V. Sada, L. R. Bellot Rubio, F. J. Aceituno, J. Aceituno, P. J. Gutierrez, and U. Thiele (2000), Optical detection of meteoroidal impacts on the Moon, *Nature, 405*, 921-923.

Ortiz, J. L., J. A. Quesada, J. Aceituno, F. J. Aceituno, and L. R. Bellot Rubio (2002), Observation and interpretation of Leonid impact flashes on the Moon in 2001, *Astrophysical Journal*, *576*, 567-573.

Richardson, J. E., and H. J. Melosh (2006), Modeling the ballistic behavior of solid ejecta from the Deep Impact cratering event, *LPSC, XXXVII*, #1836.

Schultz, P. H. (1996), Effect of impact angle on vaporization, *Journal of Geophysical Research, 101*(E9), 21,117-21,136.

Schultz, P. H., and D. E. Gault (1990), Prolonged global catastrophes from oblique impacts, in *Global Catastrophes in Earth History: An Interdisciplinary Conference on Impacts, Volcanism, and Mass Mortality*, edited by Sharpton, V. L. and P. D. Ward, pp. 239-261, Special Paper of the Geological Society of America.

Schultz, P. H., C. M. Ernst, and J. L. B. Anderson (2005), Expectations for crater size and photometric evolution from the Deep Impact collision, *Space Science Reviews 117*, 207-239.

Schultz, P. H., S. Sugita, C. A. Eberhardy, and C. M. Ernst (2006), The role of ricochet in impact vaporization, *International Journal of Impact Engineering, 33*, 771-780.

Schultz, P. H., C. A. Eberhardy, C. M. Ernst, M. F. A'Hearn, J. M. Sunshine, and C. M. Lisse (2007), The Deep Impact oblique cratering experiment, *Icarus, 190*, 295-333.

Sunshine, J. M., and 22 coauthors (2006), Exposed water ice deposits on the surface of comet 9P/Tempel 1, *Science, 311*, 1453-1455.

Sunshine, J. M., O. Groussin, P. H. Schultz, M. F. A'Hearn, L. M. Feaga, T. L. Farnham, and K. P. Klaasen (2007), The distribution and structure of water ice in the interior of comet Tempel 1, *Icarus*, *190*, 284-294.

Thomas, P. C., and 14 coauthors (2007), The shape, topography, and geology of Tempel 1 from Deep Impact observations, *Icarus, 187*, 4-15.

Yanagisawa, M., and N. Kisaichi (2002), Lightcurves of 1999 Leonid impact flashes on the Moon, *Icarus, 159*, 31-38.

Zahnle, K., and M. M. MacLow (1995), A simple model for the light curve generated by a Shoemaker-Levy 9 impact, *Journal of Geophysical Research, 100*(E8), 16,885-16,894.

Table 1. Experimental target properties

Target	Composition	ρ_b (g cm^{-3})	ρ_p (g cm^{-3})	ϕ
pumice powder	rhyolitic (> 70% SiO_2)	1.25	2.20	0.43
sieved perlite granules	rhyolitic	0.22	2.20	0.90
solid pumice block	rhyolitic	0.62	2.20	0.72
sugar	$C_{12}H_{22}O_{11}$	0.97	1.58	0.39
dolomite powder	$CaMg(CO_3)_2$	1.33	2.85	0.53

Figure Captions

Figure 1. The Tempel 1 nucleus. This is a composite of the best impactor targeting sensor (ITS) images. The sun is to the right. The box indicates the MRI field of view at the time of impact. The impact point is indicated by the white "x".

Figure 2. The first nine post-impact MRI images (out to ~ I + 500 ms). The listed times are the exposure start times with respect to the "first light" signal (frame A). The initial first light signal was overtaken by a delayed bright (saturated) signal after 117 ms (frame D). A vapor plume emerged and expanded downrange, away from the impact site, beginning in frame E. The arrow in frame A indicates the projected impact trajectory, and those in frames E-I indicate the expanding vapor plume.

Figure 3. An alternate display of the first nine post-impact MRI images. The multicolor scale better highlights details in the light intensity. The frames correspond to zoomed-in views of those in Fig. 2. A pre-impact image was subtracted from each post-impact MRI image in order to remove non-impact related light sources (including sunlight reflecting off of the nucleus surface).

Figure 4. Plot of the light intensity evolution of the first 1500 ms of the Deep Impact collision. The black curve represents the self-luminous (impact flash) portion of the light output. The intensity values for the saturated images represent minimum values. The grey curve represents the light reflected off of the expanding ejecta cloud. The dashed line is the initial linear growth trend of the reflecting portion extrapolated through time. The letters correspond to those from Fig. 2.

Figure 5. Movement of the impact flash at early times, illustrated by the location of the center of brightness for a given MRI exposure. The letters correspond to the exposure frames from Fig. 2: (A) represents the center of brightness of the first light, (C) represents the beginning of the delayed brightening (100 - 200 m downrange of the first light), and (D) represents the center of brightness of the first saturated exposure (located another 100 - 200 m downrange). The projected impact point is indicated by an "x". The arrow represents the projected impact trajectory, and lies at an angle to the apparent movement of the flash. The background image is a subset of the comet surface as observed by the impactor spacecraft (ITS) before the impact. The nucleus context image is a composite of the best ITS images.

Figure 6. Plot of the light intensity evolution of experimental impacts into targets of different porosity and volatile content. Both increasing porosity (seen in the difference between the pumice powder (i), solid pumice (ii), and perlite granule (iii) targets) and increasing volatile content (seen in the difference between the pumice powder (i) and dolomite powder (iv) targets) lead to a suppression of the luminous output of an impact.

Figure 7. Plot of the relationship between target porosity and luminous efficiency based on laboratory impacts into silicate targets (pumice powder, solid pumice, and perlite granules). The trendline represents the exponential relationship detailed in Eq. 4.

Figure 8. Light intensity evolution of experimental impacts into silicate and carbonaceous targets: (i) pumice powder, (ii) sugar, and (iii) perlite granules. (a) The evolution from 0 - 500 μs. The pumice powder signal is the brightest and the longest. On impact, pumice particulates are heated and radiate as blackbodies while cooling. The sugar is vaporized on impact, later condensing into radiating particulates. The perlite target is porous, so much of the impact flash is hidden inside of the developing transient crater, resulting in a dim, short signal. (b) The evolution from 0 - 50 μs. The sugar target exhibits an evolution that is distinct from that of the pumice powder and the perlite.

Figure 9. The effect of a highly-porous surface layer on the spatial distribution of the impact flash. (a) Side views of the experimental setup of impacts I and II. In both cases, 0.635 cm Pyrex spheres impacted at ~ 5.5 km s^{-1} at angles of 30º. The thermal imaging camera was located above and downrange of the impact point. Both targets were pumice powder, but a projectile-thick layer of highly-porous perlite granules overlaid the pumice for impact II. (b) The thermal imaging camera exposures: 250 ns exposures taken 20 μs after impact. The entire image is self-luminous material. The dashed line represents the uprange/downrange location of the point of impact, and the arrow represents the projected impactor trajectory. The addition of the high-porosity perlite layer caused major changes in the spatial distribution and exposure of the self-luminous components. The overall intensity was lower and much of the downrange component was more diffuse. All of the impact I self-luminous material was directed downrange of the impact point. In contrast, a portion of the impact II self-luminous material was directed uprange of the impact point in the form of a high-angle, uprange plume.

Figure 10. The first 500 μs light intensity curves of impacts I (grey) and II (black) from Fig. 9. The signals look different at early times, and begin to converge at later times. There is an early-time spike in the impact II signal, followed by a brief intensity decrease before the eventual intensity peak. The arrow represents the time at which the Fig. 9b images were taken.

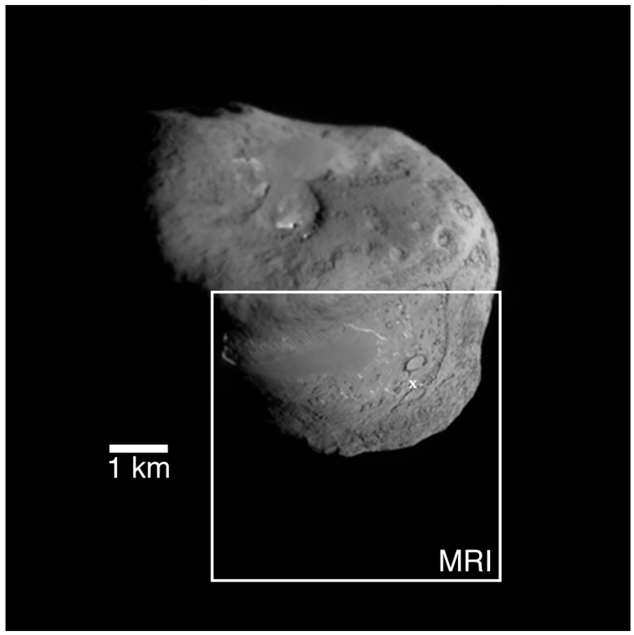

Chapter 4, Figure 1

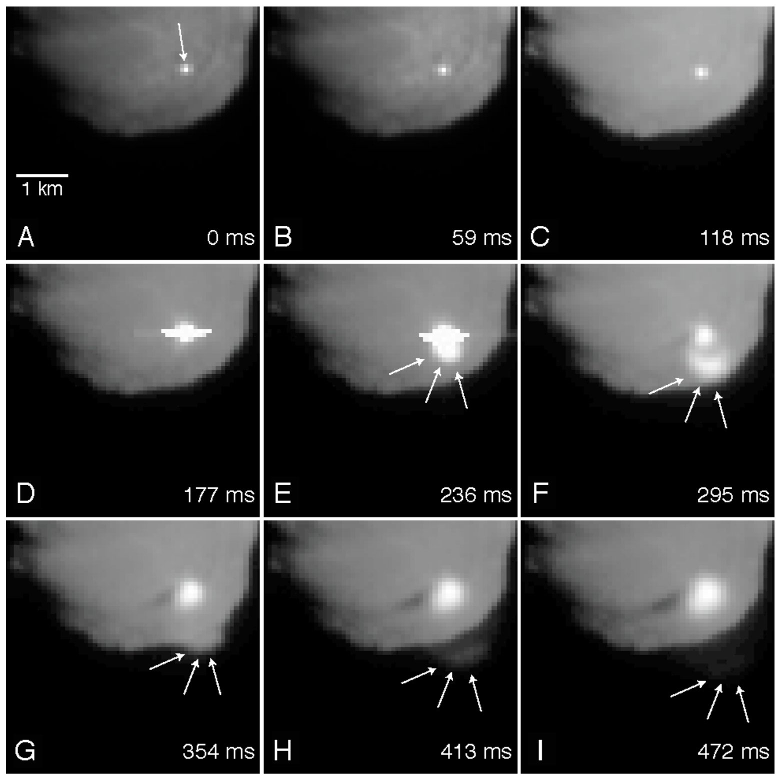

Chapter 4, Figure 2

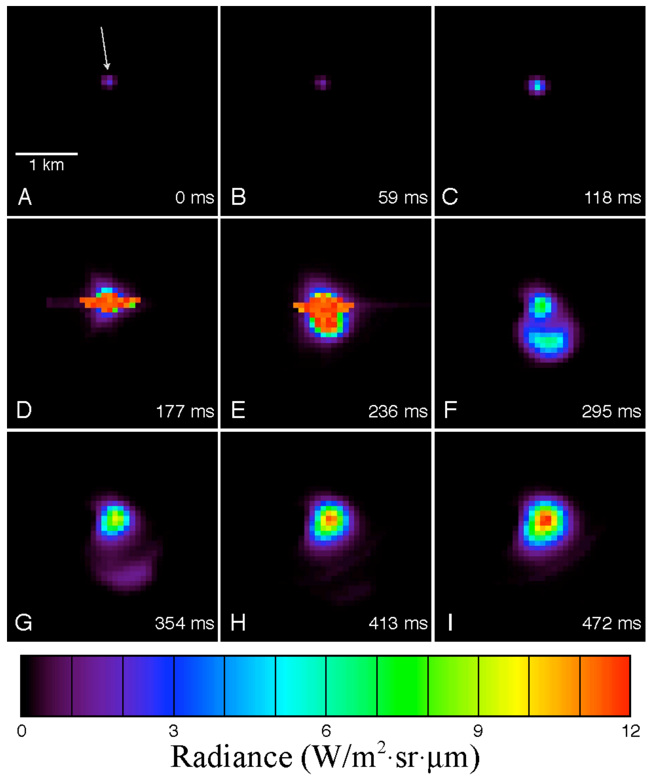

Chapter 4, Figure 3

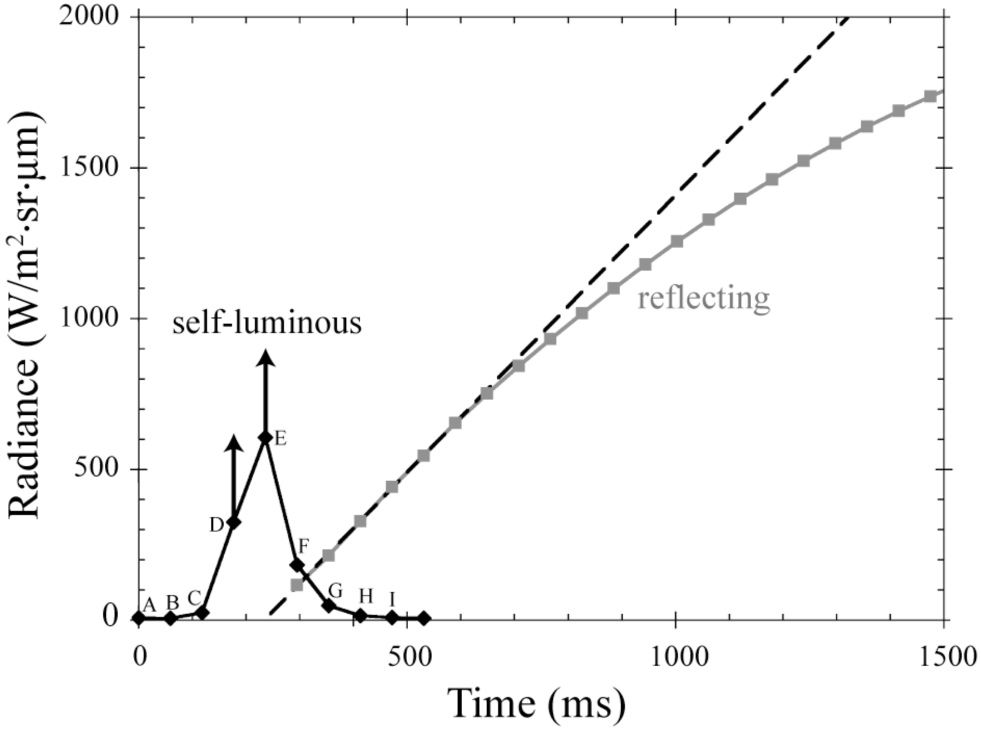

Chapter 4, Figure 4

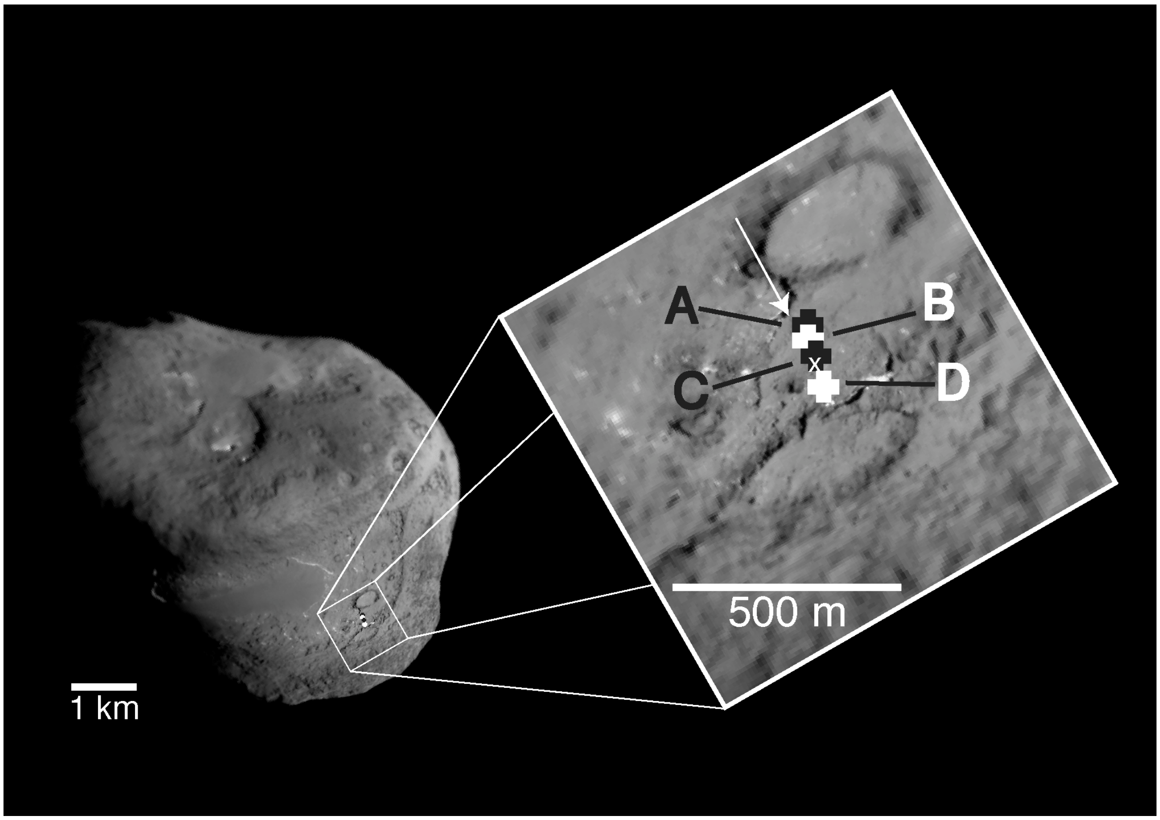

Chapter 4, Figure 5

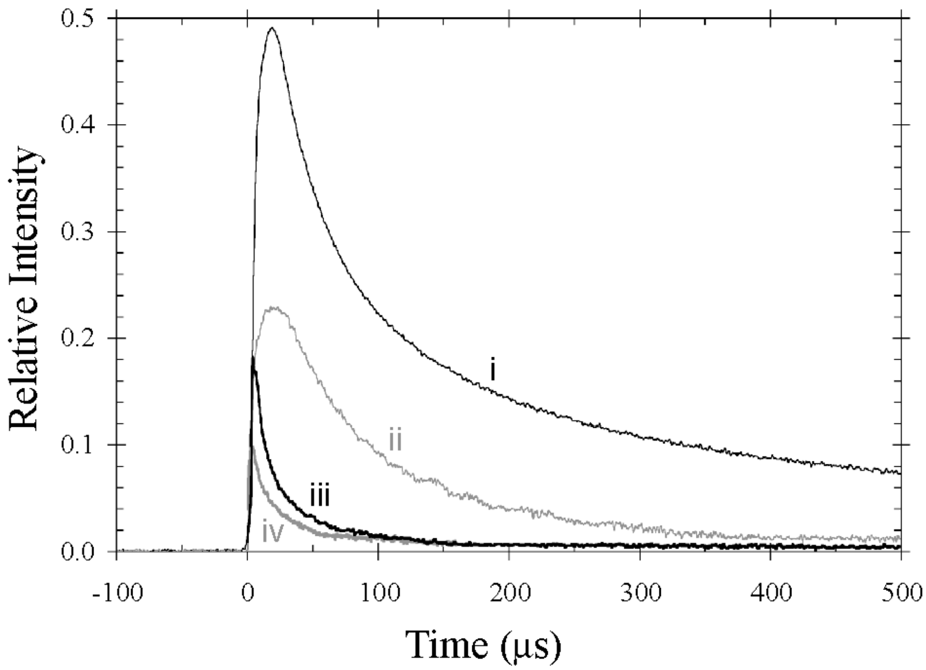

Chapter 4, Figure 6

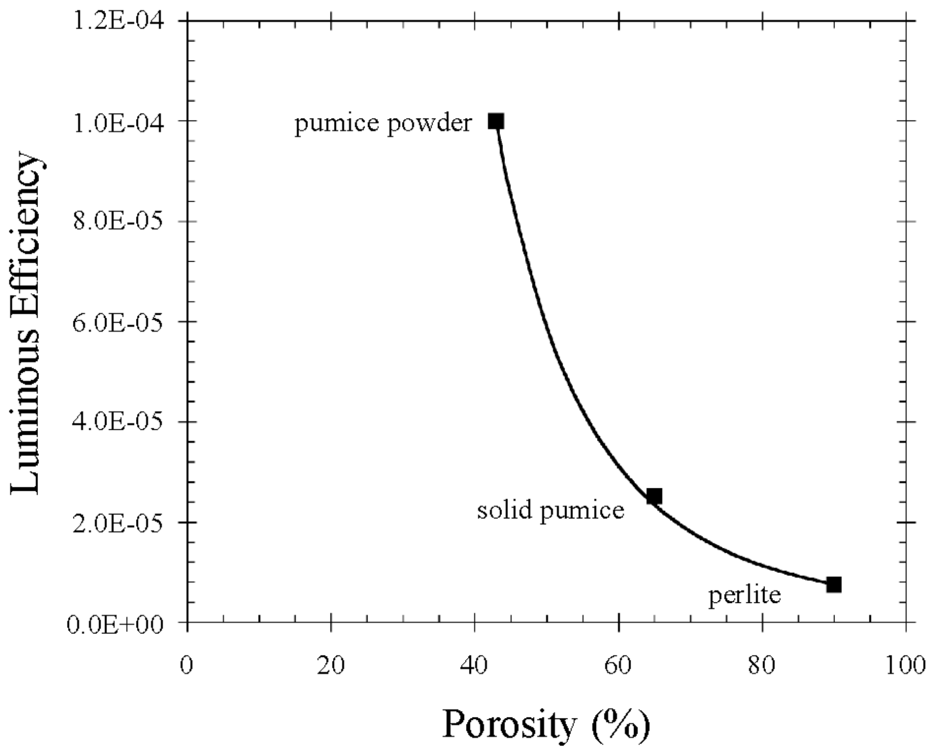

Chapter 4, Figure 7

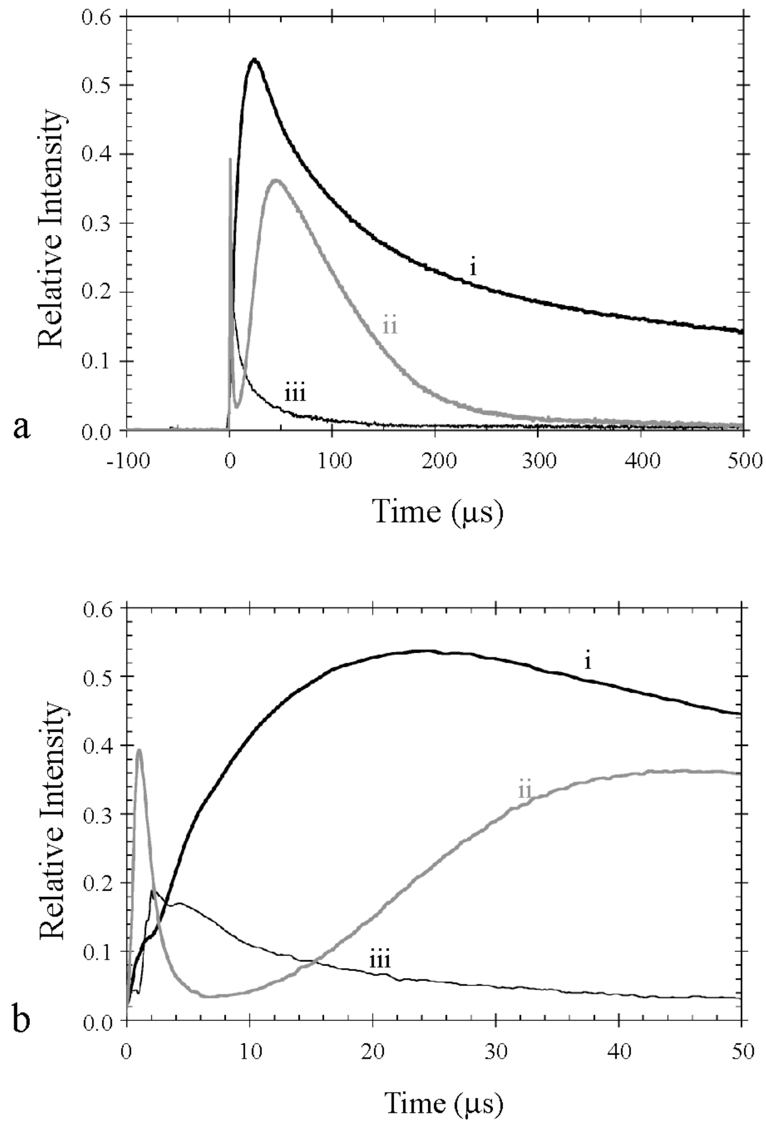

Chapter 4, Figure 8

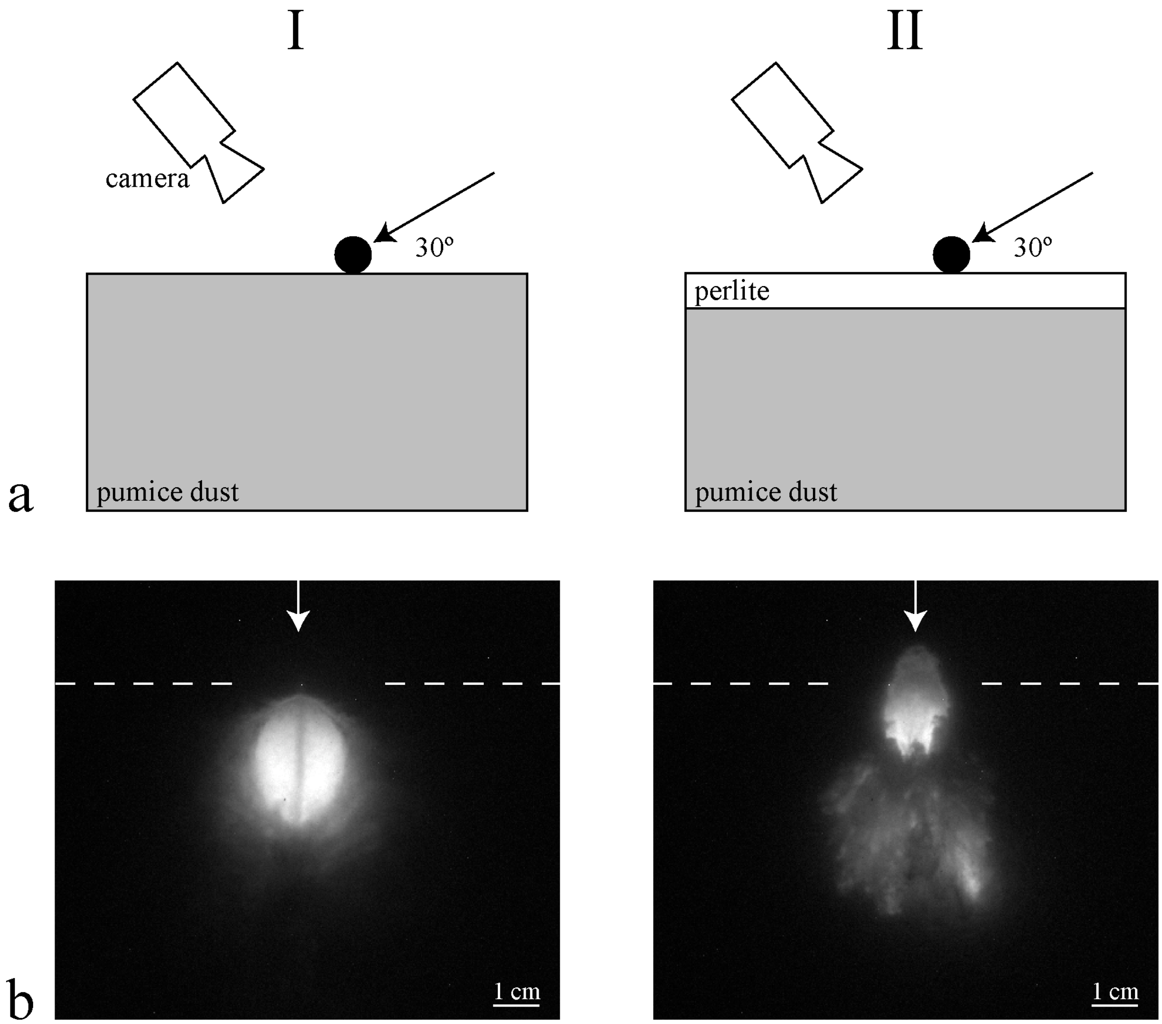

Chapter 4, Figure 9

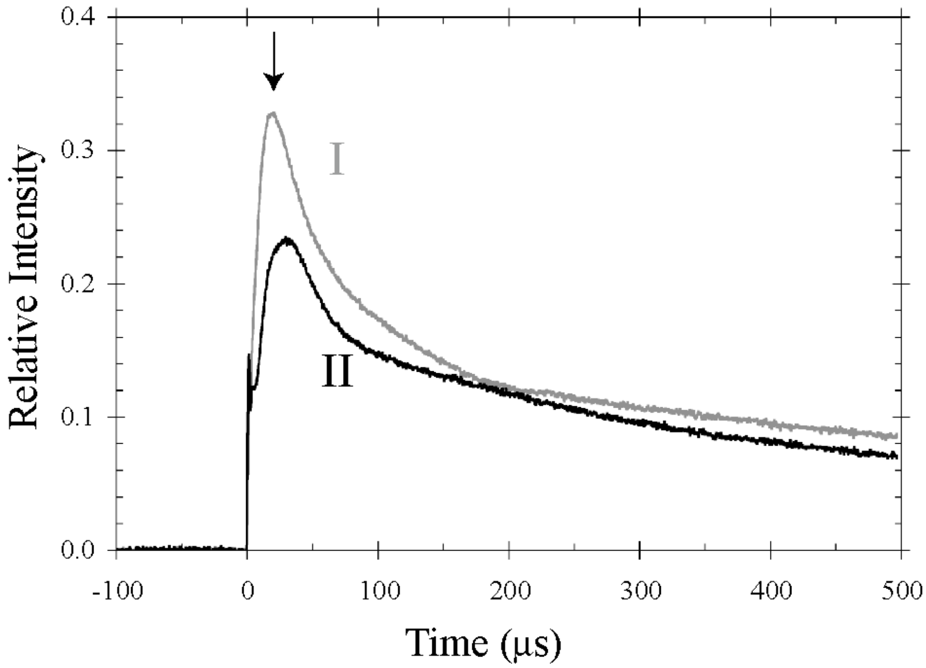

Chapter 4, Figure 10

Chapter 5

Synthesis: Evolution of the Impact Flash

Carolyn M. Ernst

Peter H. Schultz

Department of Geological Sciences

Box 1846

Brown University

Providence, RI 02912

The impact flash is a fundamental component of a hypervelocity impact event. The flash is a quickly evolving phenomenon that provides a method of observing the cratering process at early times. Previous quantitative studies of the impact flash investigated its intensity and duration for metal targets (where atomic and molecular emissions from vapor are the principal light sources), which resulted in very short duration flashes (< 10 μs) [*MacCormack*, 1963; *Jean and Rollins*, 1970; *Eichhorn*, 1976]. Sand target impacts at low velocities (~2.5 km/s) also resulted in brief flashes [*Gehring and Warnica*, 1963].

The maximum intensity for these early experimental impacts occurred during the initial projectile penetration, and the signal quickly decayed thereafter. Theoretical and computational investigations dealing only with the radiation produced by an impact-generated vapor cloud also predicted short-duration impact flashes [*Melosh et al.*, 1993; *Artem'eva et al.*, 2001]. These observations and predictions led to a general expectation that observed impact flashes should be extremely short lived. As a result, many of the initial flashes observed during meteor showers on the Moon [e.g., *Bellot Rubio et al.*, 2000; *Ortiz et al.*, 2002; *Yanagisawa and Kisaichi*, 2002] were initially doubted to be the result of impact events.

The studies performed as a part of this dissertation focus on the evolution of the flash produced by hypervelocity impacts into non-volatile, particulate targets using an experimental approach. Blackbody emissions generated by heated ejecta particles and impact melt dominate the signal. The importance of this component has been largely overlooked until this point.

The observed impact flashes in laboratory experiments using particulate targets are relatively long (lasting milliseconds), with luminous efficiency values between 10^{-4} and 10^{-5}. The primary radiating source for these experiments is melt that lines the walls and floor of the transient crater cavity. Time-resolved light intensity observations reveal three main components: an early-time spike, a delayed, broad intensity peak, and a long decay signal. The characteristics of these components are directly related to, and are highly dependent on, initial conditions (e.g., velocity, impact angle, target composition, view orientation). Because of these dependencies, laboratory-derived relationships can be used to predict the evolution of an impact flash under known initial conditions. Conversely, analysis of the impact flash evolution allows unknown conditions to be constrained remotely when most of the initial conditions are known.

The initial spike is created by high-temperature thermal emissions generated at the first contact between the projectile and the target. These emissions transition to a much longer lasting signal affected by the growth, distribution, and cooling of the evolving thermal sources (retained melt, heated particulate ejecta, and the evolution of exposed material).

Impact angle and target properties significantly affect the distribution of the heated materials. The penetration depth of a projectile is greater for higher impact angles; therefore, the early-stage transient crater will be narrowest and deepest for a vertical impact [*Schultz et al.*, 2005]. At lower impact angles, the transient crater opening is shallower and elongated parallel to the direction of impact. At low impact angles, the radiating material will be spread over a broad area, with most ejected downrange.

The maximum observed temperatures for highly porous targets (porosity > 0.7) remain high, but much of the material is confined into a deeper transient crater, thereby hiding much of the radiating source region from the detector. For impact-vaporized targets, the radiating source is dispersed above the target surface and entrained in a vapor plume, instead of primarily lining the transient crater cavity. Phase changes absorb some of the energy and uncondensed vapor emit light over limited wavelengths. The combination of all these processes significantly reduces the intensity of the impact flash.

Detectors viewing from above an impact observe not only radiating ejecta but also material contained within the transient crater (which lies below the pre-impact surface plane). In side views, however, most of the radiating material (especially in the 90º case) remains hidden by the crater walls and the emerging optically thick ejecta curtain. Consequently, view orientation affects both the observed flash magnitude and duration. This result affects estimates of luminous efficiency and impactor size.

Thermal radiation from melt controls the total luminous output of the flash for impacts into particulate silicate targets. The long-lasting decay portion of the impact flash intensity curve contributes a significant portion of the total luminous energy, with as much as 60% of the visible-wavelength energy being emitted after the intensity peak. Consequently, the intensity peak alone cannot be used to determine the luminous efficiency.

The thermal radiation from heated and melted particulates is a dominant contribution to the total luminous output of a hypervelocity impact into non-volatile particulate silicate targets. As impact velocities increase, temperatures become hotter and more material is vaporized; however, there will always be proportionally more material melted than vaporized [*O'Keefe and Ahrens*, 1977]. The thermal source results in a long-lasting impact flash. Based on the results of this dissertation, long-duration flashes, including those produced by impacts into the Moon, are not only possible but should be expected.

References

Artem'eva, N. A., I. B. Kosarev, I. V. Nemtchinov, I. A. Trubetskaya, and V. V. Shuvalov (2001), Light flashes caused by Leonid meteoroid impacts on the lunar surface, *Solar System Research*, *35*(3), 177-180.

Bellot Rubio, L. R., J. L. Ortiz, and P. V. Sada (2000), Observation and Interpretation of Meteoroid Impact Flashes on the Moon, *Earth, Moon, and Planets*, *82-83*, 575-598.

Eichhorn, G. (1976), Analysis of the hypervelocity impact process from impact flash measurements, *Planetary and Space Sciences*, *24*, 771-781.

Gehring, J. W., and R. L. Warnica (1963), An investigation of the phenomena of impact flash and its potential use as a hit detection and target discrimination technique, *6th Symposium on Hypervelocity Impact*, 627-681.

Jean, B., and T. L. Rollins (1970), Radiation from hypervelocity impact generated plasma, *American Institute of Aeronautics and Astronautics Journal*, *8*, 1742-1748.

MacCormack, R. W. (1963), Investigation of impact flash at low ambient pressures, *6th Symposium on Hypervelocity Impact*, 613-625.

Melosh, H. J., N. A. Artemieva, A. P. Golub, I. V. Nemtchinov, V. V. Shuvalov, and I. A. Trubetskaya (1993), Remote visual detection of impacts on the lunar surface, *LPSC*, *24*, 975-976.

O'Keefe, J. D., and T. J. Ahrens (1977), Impact-induced energy partitioning, melting, and vaporization on terrestrial planets, 8^{th} *Lunar Science Conference Proceedings*, 3357-3374.

Ortiz, J. L., J. A. Quesada, J. Aceituno, F. J. Aceituno, and L. R. Bellot Rubio (2002), Observation and interpretation of Leonid impact flashes on the Moon in 2001, *The Astrophysical Journal*, *576*, 567-573.

Schultz, P. H., C. M. Ernst, and J. L. B. Anderson (2005), Expectations for crater size and photometric evolution from the Deep Impact collision, *Space Science Reviews*, *117*, 207-239.

Appendix

Temperature Calibration of the Multi-Channel Photodiode System

The multi-channel photodiode system (used mainly in Chapter 2) consists of six identical photodiodes used in conjunction with narrow bandpass filters (50 - 80 nm FWHM). The filters used in this study have wavelength centers at 500, 550, 600, 650, 700, and 880 nm. The system was calibrated using a Thermogauge carbon arc blackbody source at NASA Ames Research Center's Sensor Calibration Laboratory.

The output of each photodiode is proportional to the light energy received. The non-uniform wavelength response of the detector and the spectral transmission of the filters and the target chamber windows affect the observed signals. The instrument was placed 1.0 m from the calibration source with filters and windows in place in order to eliminate their possible effects on the calculated temperatures. Calibration temperatures ranged from 1800 - 3100 K and the signal voltages for each temperature were obtained for each channel. Polynomial fits were made to the data to produce numerical relationships between signal voltage and temperature.

The radiated power per unit area per unit wavelength from a blackbody depends only on its temperature (*T*), as given by Planck's Law:

$$\frac{dR}{d\lambda} = \frac{2hc^2}{\lambda^5}\frac{1}{e^{hc/\lambda kT} - 1}, \tag{1}$$

where λ is wavelength, h Planck's constant, c the speed of light, and k Boltzmann's constant. The color temperature of a thermal radiation source can be determined using intensity ratios at different wavelengths. The data recorded for each filtered channel was ratioed to that of the 880 nm channel, and the calculated temperatures for each ratio were then averaged to produce the final temperature value. Applying this method to an entire intensity light curve generates the temperature as a function of time. Using this ratio method, the actual distance between the detector and the source does not affect the temperature calculations. Because the photodiodes record the spatially integrated light output, the calculated temperature values are spatially integrated over the entire flash at a given time. The actual temperature of the source, however, is non-uniform.

The color temperature of a source is the temperature at which a blackbody, emissivity (ε) = 1, would emit radiation corresponding to the observed intensity ratios. If $\varepsilon < 1$ but wavelength-independent (definition of a "greybody"), the color temperature of the source as determined by ratios is equivalent to its true temperature. For this study, all materials are assumed to be blackbodies, but because ratios are used, the calculated are not affected by a blackbody versus a greybody assumption.

Temperature Calibration of the CCD Camera

Intensity levels recorded in the CCD camera images (Chapter 3) were converted to temperatures through calibration with a Thermogauge dual cavity blackbody source located at NASA Ames Research Center's Sensor Calibration Laboratory. This facility was run at temperatures ranging from 600 - 2700 K. The camera was positioned 2.4 m from the blackbody source with windows inserted between the camera and the calibration source. Images were obtained at known exposure times, and intensity count versus temperature calibration data curves were created. The intensity axis of the calibration curve can be adjusted easily to account for different exposure times and source distances by multiplying by the appropriate factor. The calibration data were fit with polynomial functions to produce a numerical relationship between intensity counts and temperature.

Because the maximum temperature of the calibration source (2700 K) was lower than some of the temperatures being measured during the experiments (> 4000 K), higher uncertainties are introduced at the higher temperatures. A quartz-tungsten calibration lamp was used to confirm the calibration at 3200 K.

As discussed in Chapter 3, the maximum temperatures measured by the CCD camera (T_{CCD}) generally match within the uncertainties with the temperatures calculated from data obtained with the spatially-integrating multi-channel photodiode system (T_{PD}); however, there is a common offset from a 1:1 relationship, with $T_{CCD} < T_{PD}$. This offset likely results from the use of different temperature calculation methods. For both instrument calibrations, a blackbody intensity source was assumed. In reality, the materials used are greybodies. At a given temperature a blackbody emits more light than a greybody due to its perfect emissivity, i.e., the estimated temperature for a greybody will be too low. Because the photodiode temperature calculation method uses intensity ratios, the calculated temperatures are not affected by the blackbody assumption. In contrast, the camera calibration method uses absolute intensity values, leading to T_{CCD} being an underestimation of the actual temperature.